University of Alberta

Inverse Design of Two-Dimensional Turbomachinery Cascades: The Thickness

by

Christopher Nicholas Sideroff

A thesis submitted to the Faculty of Graduate Studies and Research in partial fulfillment of the requirements for the degree of Master of Science.

Department of Mechanical Engineering

Edmonton, Alberta
Spring 2003

National Library of Canada
Acquisitions and Bibliographic Services
395 Wellington Street
Ottawa ON K1A 0N4
Canada

Bibliothèque nationale du Canada
Acquisitions et services bibliographiques
395, rue Wellington
Ottawa ON K1A 0N4
Canada

Your file Votre référence

Our file Notre référence

The author has granted a non-exclusive licence allowing the National Library of Canada to reproduce, loan, distribute or sell copies of this thesis in microform, paper or electronic formats.

L'auteur a accordé une licence non exclusive permettant à la Bibliothèque nationale du Canada de reproduire, prêter, distribuer ou vendre des copies de cette thèse sous la forme de microfiche/film, de reproduction sur papier ou sur format électronique.

The author retains ownership of the copyright in this thesis. Neither the thesis nor substantial extracts from it may be printed or otherwise reproduced without the author's permission.

L'auteur conserve la propriété du droit d'auteur qui protège cette thèse. Ni la thèse ni des extraits substantiels de celle-ci ne doivent être imprimés ou autrement reproduits sans son autorisation.

0-612-82345-8

Canada

University of Alberta

Library Release Form

Name of Author: Christopher Nicholas Sideroff

Title of Thesis: Inverse Design of Two-Dimensional Turbomachinery Cascades: The Thickness

Degree: Master of Science

Year this Degree Granted: 2003

Permission is hereby granted to the University of Alberta to reproduce single copies of this thesis and to lend or sell such copies for private, scholarly, or scientific research purposes only.

The author reserves all other publication and other rights in association with the copyright in the thesis, and except as hereinbefore provided, neither the thesis nor any substantial portion thereof may be printed or otherwise reproduced in any material form whatever without the author's prior written permission.

Jan 10, 2003

Christopher Nicholas Sideroff
10810 85 Ave
Edmonton, Alberta
CANADA, T6E 2L1

Where a calculator on the ENIAC is equipped with 18,000 vacuum tubes and weighs 30 tons, computers in the future by the year 2000, may have only 1,000 vacuum tubes and weigh only 1.5 tons

—Popular Mechanics, March 1949

University of Alberta

Faculty of Graduate Studies and Research

The undersigned certify that they have read, and recommend to the Faculty of Graduate Studies and Research for acceptance, a thesis entitled Inverse Design of Two-Dimensional Turbomachinery Cascades: The Thickness submitted by Christopher Nicholas Sideroff in partial fulfillment of the requirements for the degree of Master of Science.

Dr. J. Yokota (Supervisor)

Dr. S. M. Kresta

Dr. B. Fleck

Date 1/10/2003

This work as well as all my previous and future endeavors in the world of engineering and science are dedicated to my late grandfather, Howard Beebe.

Abstract

A new technique to inverse design the thickness of turbomachinery blades has been developed. Coupled with the design of the camberline, this design procedure allows the designer to specify a prescribed turning distribution along with the total amount of turning to generate a two dimensional turbomachinery cascade. The procedure consists of a two dimensional flow field integrator, thickness generator, camberline generator and a passage averaged momentum/pressure boundary condition where the blade is updated in response to the prescribed turning distribution.

The blade surfaces are described as a mean camberline and thickness distribution. This technique was shown to improve the performance characteristics of turbine cascades in both subsonic and transonic flow.

With this new inverse design technique, an entire blade geometry can be designed, leading to more effective use of these techniques in the final design.

Acknowledgements

I take pride in acknowledging my supervisor, Dr. Jeff W. Yokota, for the many valuable lessons learned in the course of the past two years. Through his ability to draw a map for the road not taken, I have had the pleasure of discovering and learning many new ideas in the world of science and engineering. I know I will use the box full of tools he has offered throughout my engineering career.

I would like to express gratitude to my lab mates, colleagues and friends, Mike Wojcichowksy and Marty Lastiwka for the many endless conversations about our research. I will miss the times we had together and hope we may be able to share some of these again in the future.

I would like to thank Dr. Suzanne Kresta and Dr. Brian Fleck for participating on my oral exam as committee members.

Last but not least, thanks to my family for all their encouragement over the years. A very special thanks goes out to my girlfriend Tina. She provided me with the support, when none was there, to help me through the difficult times and showed me how rewarding this journey in life was.

Contents

1 Introduction **1**

1.1 Aerodynamic Geometry 1
1.2 Background 4
1.3 State of the Art 7
1.4 Contributions 13

2 Inverse Design **16**

2.1 Prescribed Quantity 16
2.2 Blade Boundary Interpretation 19
2.2.1 Analysis Methods 19
2.2.2 Inverse Design Methods 21
2.3 Relationship between Geometry and No-Flux Condition for Inverse Design 21
2.3.1 Camberline Generation 26
2.3.2 Thickness Generation 31
2.3.3 Thickness Correction and Update 37
2.4 Conservation Equations 41
2.4.1 Equation Classification 43
2.4.2 Non-dimensionalization 45

3 Numerical Methods **46**

3.1 Solution Sequence 46
3.2 Thickness Generator 48
3.2.1 Time Advancement 49
3.2.2 Spatial Discretization 50
3.2.3 Boundary Conditions 52
3.2.4 Numerical Stability and Time Step 52
3.3 Camberline Generator 56

3.4 Flow Field Integrator 57
3.4.1 Time Advancement 57
3.4.2 Spacial Discretization 58
3.4.3 Artificial Dissipation 62
3.4.4 Numerical Stability and Time Step 64
3.5 Boundary Conditions for Flow Equations 65
3.5.1 Inflow and Outflow Boundaries 65
3.5.2 Periodic Boundary 67
3.5.3 Blade Surfaces 68

4 Design Procedure and Results **75**
4.1 Subsonic Test Cases 79
4.1.1 Subsonic Case 1: Camberline Generation - Smooth Prescribed Thickness 81
4.1.2 Subsonic Case 2: Camberline Generation - Oscillations in Prescribed Thickness 92
4.1.3 Subsonic Case 3: New Design - Oscillations in Prescribed Thickness 101
4.2 Transonic Test Cases 132
4.2.1 Transonic Case 1: Camberline Generation - Discontinuous Geometry 134
4.2.2 Transonic Case 2: New Design - Discontinuous Geometry 143

5 Conclusions **162**

A Derivation of Euler Equations from First Principles **171**
A.1 Conservation of Mass 172
A.2 Conservation of Linear Momentum 173
A.3 Conservation of Energy 175

List of Figures

1.1 Airfoil Shape 2
1.2 Turbomachinery Blade Shape 2
1.3 Aerodynamic Shape Components 3
1.4 2-D Turbomachinery Cascade 4
1.5 Inverse Design Flow Chart 8

2.1 No-Flux Blade Boundaries 20
2.2 Vortex Sheet Blade Boundaries 20
2.3 Sketch of Flat Plate Cascade 22
2.4 Sketch of Infinitely Thin Cascade 23
2.5 Sketch of Axial Turbomachinery Cascade 25
2.6 Flow Domain 28
2.7 Discontinuous Geometry & Passage Shock: Mach No. Contours 31
2.8 Blades with Zero Camberline 34
2.9 Hyperbolic Tangent Function: Mach No. Contours 39
2.10 Exponential Function: Mach No. Contours 40

3.1 Control Volume 58
3.2 Control Volume Surface 59
3.3 Uniform Square Grid 61

4.1 Typical Sheared H-type Mesh 78
4.2 Prescribed Turning Distribution for Subsonic Cases 80
4.3 Subsonic Case 1: Prescribed Thickness Distribution 83
4.4 Subsonic Case 1: Converged Blade Shape 84
4.5 Subsonic Case 1: Contours of Mach Number in the Blade Passage 85
4.6 Subsonic Case 1: Blade and Velocity Angles - Suction Side . 86
4.7 Subsonic Case 1: Blade and Velocity Angles - Pressure Side 87

4.8 Subsonic Case 1: Pressure Distribution on Blade Surface - Suction Side 88
4.9 Subsonic Case 1: Pressure Distribution on Blade Surface - Pressure Side 89
4.10 Subsonic Case 1: Turning Distributions in Blade Passage . . 90
4.11 Subsonic Case 1: Convergence History 91
4.12 Subsonic Case 2: Prescribed Thickness Distribution 94
4.13 Subsonic Case 2: Converged Blade Shape 95
4.14 Subsonic Case 2: Contours of Mach Number in the Blade Passage 96
4.15 Subsonic Case 2: First Derivative of Camber 97
4.16 Subsonic Case 2: Pressure Distribution on Blade Surface - Suction Side 98
4.17 Subsonic Case 2: Pressure Distribution on Blade Surface - Pressure Side 99
4.18 Subsonic Case 2: Turning Distributions in Blade Passage . . 100
4.19 Subsonic Case 3: Step 1 - Prescribed and Calculated Thickness Distributions Passage 104
4.20 Subsonic Case 3: Step 1 - Blade and Velocity Angles - Suction Side 105
4.21 Subsonic Case 3: Step 1 - Blade and Velocity Angles - Pressure Side 106
4.22 Subsonic Case 3: Step 1 - Contours of Mach Number in the Blade Passage 107
4.23 Subsonic Case 3: Step 1 - Pressure Distribution on Blade Surface - Suction Side 108
4.24 Subsonic Case 3: Step 1 - Pressure Distribution on Blade Surface - Pressure Side 109
4.25 Subsonic Case 3: Step 1 - Turning Distributions in Blade Passage 110
4.26 Subsonic Case 3: Step 2 - Blade and Velocity Angles - Suction Side 113
4.27 Subsonic Case 3: Step 2 - Blade and Velocity Angles - Pressure Side 114
4.28 Subsonic Case 3: Step 2 - Converged Blade Shape 115
4.29 Subsonic Case 3: Step 2 - Contours of Mach Number in the Blade Passage 116

4.30 Subsonic Case 3: Step 2 - Pressure Distribution on Blade Surface - Suction Side 117
4.31 Subsonic Case 3: Step 2 - Pressure Distribution on Blade Surface - Pressure Side 118
4.32 Subsonic Case 3: Step 2 - Turning Distributions in Blade Passage 119
4.33 Subsonic Case 3: Prescribed and Calculated Thickness Distributions 123
4.34 Subsonic Case 3: Converged Blade Shape 124
4.35 Subsonic Case 3: Contours of Mach Number in the Blade Passage 125
4.36 Subsonic Case 3: Pressure Distribution on Blade Surface - Suction Side 126
4.37 Subsonic Case 3: Pressure Distribution on Blade Surface - Pressure Side 127
4.38 Subsonic Case 3: Turning Distributions in Blade Passage . . 128
4.39 Subsonic Case 3: Blade and Velocity Angles - Suction Side . 129
4.40 Subsonic Case 3: Blade and Velocity Angles - Pressure Side 130
4.41 Subsonic Case 3: Convergence History 131
4.42 Prescribed Turning Distribution for Transonic Cases 133
4.43 Transonic Case 1: Prescribed Thickness Distribution 136
4.44 Transonic Case 1: Contours of Mach Number in the Blade Passage 137
4.45 Transonic Case 1: Converged Blade Shape 138
4.46 Transonic Case 1: Pressure Distribution on Blade Surface - Suction Side 139
4.47 Transonic Case 1: Pressure Distribution on Blade Surface - Pressure Side 140
4.48 Transonic Case 1: Turning Distributions in Blade Passage . . 141
4.49 Transonic Case 1: Convergence History 142
4.50 Transonic Case 2: Step 1 - Blade and Velocity Angles - Suction Side 145
4.51 Transonic Case 2: Step 1 - Blade and Velocity Angles - Pressure Side 146
4.52 Transonic Case 2: Step 1 - Prescribed and Calculated Thickness Distributions 147
4.53 Transonic Case 2: Step 1 - Contours of Mach Number in the Blade Passage 148

4.54 Transonic Case 2: Step 1 - Pressure Distribution on Blade Surface - Suction Side 149
4.55 Transonic Case 2: Step 1 - Pressure Distribution on Blade Surface - Pressure Side 150
4.56 Transonic Case 2: Step 1 - Turning Distributions in Blade Passage 151
4.57 Transonic Case 2: Converged Blade Shape 154
4.58 Transonic Case 2: Contours of Mach Number in the Blade Passage 155
4.59 Transonic Case 2: Pressure Distribution on Blade Surface - Suction Side 156
4.60 Transonic Case 2: Pressure Distribution on Blade Surface - Pressure Side 157
4.61 Transonic Case 2: Turning Distributions in Blade Passage . . 158
4.62 Transonic Case 2: Blade and Velocity Angles - Suction Side 159
4.63 Transonic Case 2: Blade and Velocity Angles - Pressure Side 160
4.64 Transonic Case 2: Convergence History 161

Nomenclature

Latin symbols

a	Speed of Sound, $\frac{m}{s}$
c	Chord Length, m
e_t	Total Energy, $\frac{kJ}{kg}$
$\vec{E}$	Flux Vector in x-direction
$\vec{F}$	Flux Vector in y-direction
f	Calculated Camberline, m
G	Growth Factor
Δh_o	Change in Stagnation Enthalpy, $\frac{kJ}{kg}$
J	Jacobian of Transformation
$\dot{m}$	Mass Flow, $\frac{kg}{s}$
$\vec{n}$	Surface Normal Vector
R	Gas Constant, $\frac{kJ}{kg\,K}$
$\vec{R}$	Residual of Inverse Equations
$\vec{R}_T$	Residual of Thickness Correction
SC	Spacing to Chord Ratio

P ..... Pressure, $\frac{N}{m^2}$

P_o ..... Stagnation Pressure, $\frac{N}{m^2}$

P^+ ..... Upper Surface Pressure, $\frac{N}{m^2}$

P^- ..... Lower Surface Pressure, $\frac{N}{m^2}$

Δt ..... Time Step

T ..... Updated Thickness, m

T_{fixed} ..... Fixed Thickness, m

T_{corr} ..... Calculated Thickness Correction, m

$\frac{T_{max}}{SC}$ ..... Maximum Thickness to Spacing Ratio

(u, v) ..... Cartesian Velocity Components, $\frac{m}{s}$

(u^+, v^+) ..... Upper Surface Velocity Components, $\frac{m}{s}$

(u^-, v^-) ..... Lower Surface Velocity Components, $\frac{m}{s}$

$\bar{v}_y$ ..... Mass Flux Average Tangential Velocity, $\frac{m}{s}$

$\Delta\bar{v}_y$ ..... Total Change in Mass Flux Average Tangential Velocity Across Blade Row, $\frac{m}{s}$

$\vec{w}$ ..... Conservative Variable Vector

$\vec{W}$ ..... Solution Vector for Inverse Design Equations

$\dot{W}$ ..... Power, $\frac{kJ}{s}$

(x, y) ..... Cartesian Coordinates, m

$\forall$ ..... Control Volume, m^3

GREEK SYMBOLS

$\alpha^{\pm}$ ..... Function for Upper and Lower Airfoil Surfaces, m

β ..... Inlet Flow Angle, Radians

γ ..... Ratio of Specific Heat Capacities

(ξ, η) ..... Generalized Coordinates

ρ ..... Density, $\frac{kg}{m^3}$

Θ ..... Temperature, K

Θ_0 ..... Stagnation Temperature, K

Υ ..... Internal Energy, $\frac{J}{kg}$

ω ..... Angular Velocity of Blade Row, $\frac{\text{Radians}}{s}$

Chapter 1

Introduction

1.1 Aerodynamic Geometry

In the study of aerodynamics there exist two general types of shapes: airfoils, which are used to generate lift; and turbomachinery blades, which are used to add (compressor) or extract (turbine) energy from the working fluid. A generic airfoil is shown in Fig. (1.1) while a generic turbomachinery blade is shown in Fig. (1.2). The important global flow characteristics of both airfoils and turbomachinery blades are the lift and drag. In the case of turbomachinery blades, flow turning is used synonymously with lift. Flow turning is used in the case of the turbomachinery because this phenomenon can be directly related to power through the Euler Turbine Equations [Laksh. 1996]. The greater curvature of the cascade of turbomachinery blades turns the flow more than a single airfoil and with this turning, comes a greater amount of energy transferred. The turning and the drag produced by the blade are of the most important performance characteristics of a turbomachinery blade.

In order to modify the geometry, designers need a precise concept to

Figure 1.1: Airfoil Shape

Figure 1.2: Turbomachinery Blade Shape

describe the aerodynamic shape. To determine what changes in geometry benefit or adversely affect its aerodynamic performance, designers require a thorough description of the airfoil or blade in order. One such description involves the combination of a camberline and thickness distribution [Abbott 1959][von Mises 1959].

Any aerodynamic shape, whether it is an airfoil or turbomachinery blade, can be described using these components, camberline and thickness. Fig. (1.3) shows a basic aerodynamic shape, with the leading edge, trailing edge, camberline, chord line and thickness as indicated. The chord line is a straight line connecting the leading edge (front) to the trailing edge (rear) of the

airfoil. The camberline is the mean line between the upper and lower blade surfaces while the thickness is defined as the vertical distance from the upper surface to lower surface. Camberline and thickness are generally given as ratios of chord length.

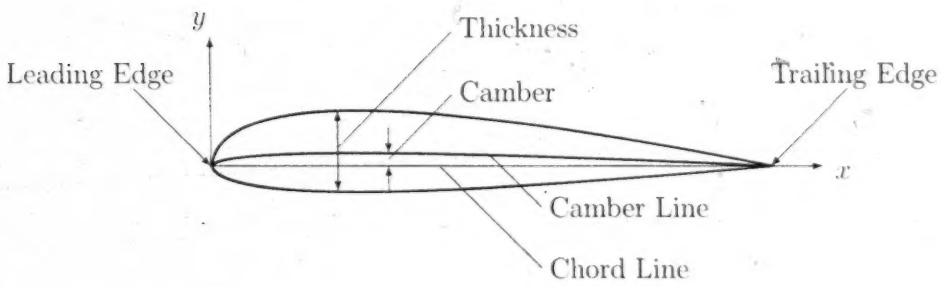

Figure 1.3: Aerodynamic Shape Components

The camberline is associated with the amount of lift, in the case of the airfoil, or turning generated, in the case of the turbomachinery blade. In the turbomachinery case, the angle of flow meeting the blade matches the angle of the camberline at the leading edge and the angle of flow leaving the blade matches the angle of the camberline at the trailing edge. The difference between these angles governs the total amount of turning done by the blade. The more curvature the greater the amount of turning.

Thickness influences drag, choking, shocks and viscous effects such as boundary layer separation. An exceedingly thick blade can produce high drag and thus reducing its efficiency. Choking is caused when the thickness

distribution between a pair of cascade blades is so thick that they cause the flow to become sonic. A typical two dimensional cascade is shown in Fig. (1.4) Supersonic flow between blades must behave like a convergent divergent supersonic nozzle where the flow must shock when the nozzle geometry requires the flow to decelerate to subsonic. Shocks occurring inside turbomachinery cascades cause significant energy losses. Thus designing for the thickness is important in controlling the effects of phenomena which create energy loses such as choking, shocks and drag. Both camberline and thickness are required to redesign a complete aerodynamic shape.

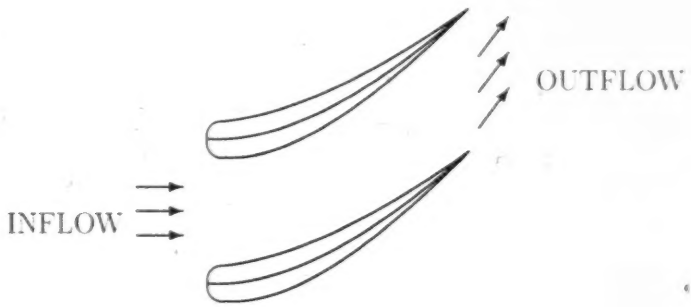

Figure 1.4: 2-D Turbomachinery Cascade

1.2 Background

There are four widely used approaches towards aerodynamic design. These four approaches are experimental analysis, computational analysis, optimization and inverse design.

The first approach involves the experimental analysis of an aerodynamic

shape. Historically aerodynamic shapes were designed graphically, using aesthetics to determine the final shape. The use of early wind tunnels allowed the design of basic airfoil forms such as the Göttingen [Abbott 1959, von Mises 1959] and Clark-Y [Abbott 1959] airfoils. The airfoils were tested in experimental wind tunnels and the performance characteristics were recorded. If designers wanted specific performance characteristics the airfoils were then modified and tested again. This procedure was repeated until an airfoil shape was found which yielded the desired performance characteristics. This design approach was very costly due to construction of many different airfoils. It was also costly due to the experimental facilities required. The entire design was based solely on the experience of the designer and no equations were available to relate the airfoil geometry to the flow.

The second approach to aerodynamic design, computational analysis, performs a similar function as the first in that it also involves analysis of an existing shape. Some examples of computational analysis methods are those of Jameson and Caughy [Jameson and Caughey 1977] and Jameson [Jameson et.al. 1979]. The difference between this approach and the experimental approach is that instead of using wind tunnel experiments to determine the performance characteristics, they are found using a computational simulation of flow around the aerodynamic shape. The computational analysis can determine characteristics such as lift, drag, pressure distributions as well as velocities, densities and other variables. The benefit to this approach over experimental testing is that it is more economical to use a computer to perform an analysis of an airfoil than an experimental facility. The downfall of the computational analysis is that the analysis is performed

on airfoil geometries, which are chosen solely on the designers experience. The desired performance criteria is only achieved through multiple iterations of blade modification and subsequent analysis. This method does not give any insight into the mathematical relationship between the airfoil geometry and the desired performance criteria.

The third approach to aerodynamic design is optimization. Numerical optimization methods begin with a database of many existing airfoils. An objective function is then implemented so that an airfoil from the database of existing airfoils, can be chosen such that its performance characteristics match closest to the desired characteristics. These methods are usually combined with a computational analysis method and have the advantage over stand alone computational analysis in that the best airfoil is found using a mathematical minimizing model. The experience of the designer required to chose an appropriate airfoil is eliminated thus saving time. The methods of Hicks [Hicks 1987] and Eyi and Lee [Eyi and Lee 1995] are examples of this approach. Again the drawback is that no mathematical relation between the airfoil geometry and the performance criteria is found.

The final approach to aerodynamic design is the use of an inverse design method. Inverse design is typically completed using computational methods but some analytical methods do exist [Hawthorne 1984, Tan et.al. 1984]. Instead of the designer analyzing the blade or airfoil and making changes to the geometry, with inverse design the designer specifies some performance criterion and then calculates the physical geometry needed to produce the specified criterion. The performance criteria that can be used as controls are pressure distributions, velocity profiles, turning distributions, lift or drag.

Inverse design methods are becoming increasingly popular throughout the industry. With the ever increasing performance of computers, the potential of these methods are beginning to be realized. Many advances have been made with inverse design techniques and current inverse design methods are now approaching the sophistication level of current analysis methods.

1.3 State of the Art

The history of inverse design is relatively young but there has been development of many different approaches in this time. There has been work with analytical techniques but with the advent of powerful yet inexpensive computers, numerical techniques have dominated. Original methods neglected thickness in the blade description and looked at cascades of infinitely thin blades. As the techniques improved, some methods began to include thickness, even though it was fixed.

There also has been a wide variety of specified design criteria used. Surface pressures and velocities, have been the conventional choice. A more flexible prescribed quantity, that has also been used extensively, called turning distribution, relates the flow turning of a cascade with the boundary pressures.

Since many different theories and approaches to inverse design have been investigated, a flow chart Fig. (1.5), illustrating the various methods along with the authors is included. This flow chart is referenced to show where the previous methods fit into the evolution of the science and to highlight the path chosen for the current work. The comments listed under each author are included as either a benefit, denoted by $\surd$, or a deficiency, denoted by

X.

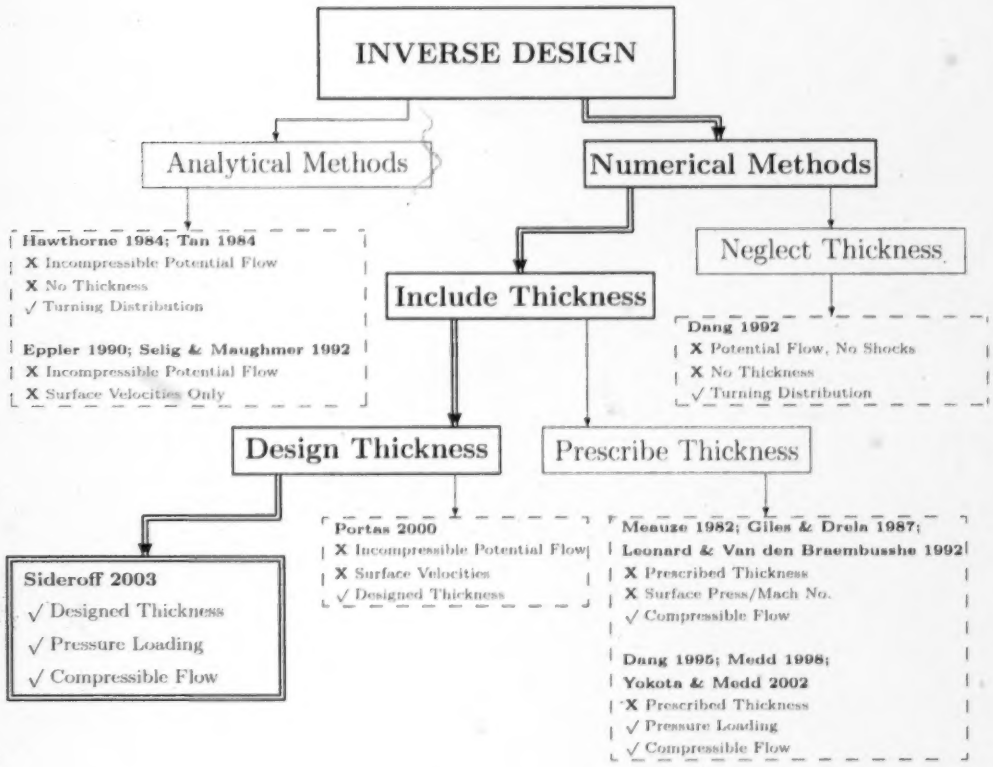

Figure 1.5: Inverse Design Flow Chart

The analytical inverse design techniques of Hawthorne et.al. [Hawthorne 1984] and Tan et.al. [Tan et.al. 1984] investigate the use of the circulation method to construct infinitely thin cascades where the fluid is assumed to be inviscid and incompressible. With these methods, the infinitely thin blades are represented by a sheet of bound vortices and the equations of motion are cast in terms of Clebsch variables. Classical Fourier expansion

techniques were employed to solve the equations for the Clebsch variables. Due to the nature of the reduced equations, rotational flow cannot be modelled downstream of the trailing edge. The use of a passage averaged flow turning was developed and used as the prescribed quantity. These methods also neglect the thickness when considering the design of the cascade. By ignoring the effects of the thickness, obtaining a practical design may be difficult. Under the analytical stream of Fig. (1.5), the methods of Hawthorne and Tan are included with incompressible flow and the neglect of thickness as deficiencies while a benefit is the use of a passage averaged tangential velocity as the prescribed design quantity.

The inverse design method devised by Selig and Maughmer [Selig & Maughmer 1992] uses surface velocity distributions to determine the aerodynamic shape based on conformal mapping methods. The use of conformal mapping only allows for the solution of surface characteristics along with the designed airfoil and not the entire flow field. This is a deficiency in that a flow field solution is required to determine the presence of other characteristics of the airfoil or blade such as choking, shocks or viscous phenomena. The lack of a flow field also occurs with Eppler's [Eppler 1990] inverse design. While both of these methods design the entire aerodynamic shape, they lack a complete flow field solution. These analytical methods based on conformal mapping are also included under the analytical stream of Fig. (1.5). The deficiencies are the lack of a flow field calculation and the assumption of an incompressible fluid.

On the numerical branch, the work of Dang [Dang 1992] employs the circulation method of Hawthorne and Tan but is modified to include a tran-

sonic flow regime. To allow solutions in this regime, the continuity equation is cast in conservative form and solved numerically. In this case, the use of potential flow calculations prevents capturing strong shocks in the flow field. The same passage averaged turning distribution as used by Hawthorne and Tan is used as the prescribed quantity. Again, the effect of thickness is not considered therefore reducing the method's effectiveness for the design of practical blades. This numerical method of Dang now includes compressible flow, a benefit in Fig. (1.5), but calculates only the flow potential and neglects thickness, deficiencies in Fig. (1.5).

The next group of methods extends the assumption of an infinitely thin blade by including the thickness. The method of Jiang and Dang [Jiang & Dang 1997] extends Dang's [Dang 1992] method to handle finite thickness. However, the thickness is arbitrarily prescribed and does not change during the design procedure. One other downfall is that only an incompressible fluid is modeled, thus eliminating transonic effects. Design of more efficient transonic blades is not possible with techniques that neglect thickness or compressibility.

Other methods that include thickness have also been developed that use different design criteria. Techniques devised by Meauze [Meauze 1982], Giles and Drela [Giles & Drela 1987] and Leonard and Van den Braembussche [Leonard & Van den Braembussche 1992] calculate the entire flow field using the Euler equations and inverse design the camberline given pressure distributions or Mach numbers on the blade surfaces. Although a thickness distribution is now included, it is once again not designed and remains constant through the procedure. The generic thickness that is prescribed may

be too thick, causing energy losses due to choking or shocks, or it may have large surface curvature, causing boundary layer separation in a viscous flow. Another limitation is the prescription of pressure or Mach number distributions along the blade surfaces. The assumption required to use pressure distributions is that the blade surfaces must be streamlines of the flow. The limitation is that if these methods were to be extended from two to three dimensions, it would be difficult to predict the location of the streamlines a priori, making it difficult to specify these Mach number and pressure distributions. This limits the specification of the pressure and Mach number distributions to two dimensional flow, hence limiting the future application of this method. As well, specification of both upper and lower surface pressures means that the converged blade shape may not be closed at the trailing edge, i.e. it may have a fish tail geometry at convergence. This is because it is difficult to know what pressures to specify at the leading and trailing edge of the blade. These numerical methods using surface pressure or Mach numbers as the prescribed quantity lie under the numerical-prescribed thickness stream of Fig. (1.5). These methods are deficient in the use of prescribed thickness and surface pressures or Mach numbers but now include compressible calculations which can capture shocks.

The Hodograph method used by Sanz [Sanz 1998] allows linearization of the compressible potential flow equations. This is a numerical benefit but the potential flow equations do not allow calculation of strong shocks. In addition, this method is limited to two dimensions by surface pressure specification and because of the transformation to the Hodograph plane. The transformation to the Hodograph plane is not possible in three dimensions.

A significant improvement of designing camberline are the methods devised by Dang [Dang 1995] and Dang and Isgro [Dang & Isgro 1995]. These methods use a turning distribution instead of pressure distributions, where the pressure boundary condition uses a passage averaged momentum analysis to couple the pressure with the flow turning. A thickness distribution and the turning distribution are used as the prescribed quantities. The benefit of using turning instead of surface pressures or velocities is that it can be related, via the Euler Turbine Equations [Laksh. 1996], to work done on a fluid. Specification of the turning can also easily be extended to three dimensions since it is not limited to knowing the location of the streamlines. The final benefit is that it enforces the Kutta condition, meaning it guarantees that the blade be closed at the trailing edge. As with the previous methods, the design of thickness is still neglected and limits its application for practical designs.

Another method using turning distributions and the Euler Turbine Equations to design transonic turbomachinery blades was developed by Medd [Medd 1998] and Yokota and Medd [Yokota & Medd 2002], the method upon which the present work is based. In this technique the thickness distribution is specified along with the turning distribution, allowing design of the camberline. It uses the compressible Euler equations to solve for the flow field. Therefore the ability to simulate transonic and supersonic flows is gained. Having this ability allows design consideration of choking and shocks in the blade passage. The only deficiency of this method is that it uses a prescribed thickness which does not change throughout the method. Thus it does not have the ability to eliminate choking or shocking in a cascade of turbine

blades due to the thickness. Methods using a constant prescribed thickness have limited usefulness because design of the entire geometry, including both camberline and thickness, is required to redesign an aerodynamic shape. The methods of Dang [Dang 1995], Dang and Isgro [Dang & Isgro 1995], Medd [Medd 1998] and Yokota and Medd [Yokota & Medd 2002] are all deficient in this regard. These methods are shown in the numerical-prescribed thickness stream of Fig. (1.5) where compressible flow calculation and the prescribed turning are benefits while the deficiency is the lack of thickness design.

The only notable work which includes design of the entire blade geometry is that of Portas [Portas 2000]. This method includes design consideration of both the thickness and camberline. With the inclusion of the thickness in the design procedure, the influence of the prescribed design criteria is felt throughout the entire blade geometry, not just the camberline. This method assumes incompressible, potential flow. Important compressible effects, such as choking and shocks, cannot be included into the design of the blade with this method. Another drawback with this design philosophy, is the use of prescribed surface velocity distributions, limiting the possibility of extending this method to three dimensions. The benefits and deficiencies are shown in the numerical-design thickness stream of Fig. (1.5).

1.4 Contributions

In order to correctly design an airfoil or turbomachinery blade the design method needs to incorporate the design of camberline as well as the thickness. A new technique to inversely design the thickness of turbomachinery blades has been developed.

First, using the no-flux condition on the blades, an equation to calculate the thickness from these surface velocities was derived. Then, the resulting first order partial differential equation was transformed into a second order partial differential equation to control the thickness at both the leading and trailing edges.

To minimize problems at the leading edge, caused by H-type shearing of the computational mesh, the thickness equation was rewritten in terms of fixed and corrected quantities. A treatment to control changes near the leading and trailing edges was developed. Various functions were evaluated to produce a thickness without inadvertently introducing any abnormal geometry changes. Finally, the thickness equation was rederived with the inclusion of this leading edge treatment.

A numerical approximation of the thickness equation was constructed to couple the design of the thickness with the existing camberline method. Various numerical constructions were investigated with the final approximation chosen to yield solutions without allowing erroneous mass flow through the blades.

The method developed to design the thickness in this work was coupled with an existing camberline method. The thickness design method presented in this thesis is coupled with the previous work of Medd [Medd 1998] and Yokota and Medd [Yokota & Medd 2002] to create a technique that inversely designs the entire blade geometry. It calculates a two dimensional compressible flow field thus allowing for choking and shocks. It uses turning distribution as its design criteria so the method has the potential to be extended to three dimensions. An airfoil can be designed by camberline alone but the

thickness will be the deciding factor on whether or not the final shape will be practical. A camberline may match a given performance criteria, such as turning distribution, but different thickness distributions will eliminate possible applications since they may cause choking, shocks or boundary layer separation. The key components of this method which separates it from all previous work are the consideration of both thickness and camberline design along with turning distribution as the performance criteria. The developed method is highlighted in the numerical-design thickness stream of Fig. (1.5).

Chapter 2

Inverse Design

2.1 Prescribed Quantity

With the inverse design of an airfoil or turbomachinery blade the geometry is not know a priori therefore some control measure must be prescribed. Some conventional choices for the prescribed quantity in various two dimensional blade-to-blade methods are Mach numbers or pressure distributions on the upper and lower blade surface [Meauze 1982] [Giles & Drela 1987] [Leonard & Van den Braembussche 1992]. These blade surface pressure distributions, in general, are chosen to avoid separation. The problem with using blade surface pressures is that the streamlines need to be known a priori. This is the case in two dimensional cascades where the streamlines of the flow are known to lie on the blade surfaces. This may not be true with three dimensional cascades where significant radial flows exist in the flow passage due to hub, blade tip and shroud interactions. In this work the prescribed flow quantity is the mass-flux averaged tangential velocity distribution derived following the method of Hawthorne et.al. [Hawthorne 1984]

and Tan et.al. [Tan et.al. 1984]. This prescribed flow quantity, for the two dimensional case, can be defined as

$$\bar{v}_y(x) = \frac{\int_+^- \rho\, u(x,y)\, v(x,y)\, dy}{\int_+^- \rho\, u(x,y)\, dy} = \frac{\int_+^- \rho\, u(x,y)\, v(x,y)\, dy}{\dot{m}} \tag{2.1}$$

where the limits of integration + and − denote the upper and lower blade surface respectively, ρ is the density, u and v and the Cartesian components of velocity and $\dot{m}$ is the mass flow.

Another advantage in using the mass-flux averaged tangential velocity distribution is that it can be related to the energy requirements of a turbomachine. Turbomachines extract or supply energy to the working fluid by imparting change in the fluid direction. As shown by the Euler Turbine Equation [Laksh. 1996], the total power of the turbomachine can be related to the flow turning

$$\dot{W} = \dot{m}\omega r \Delta\bar{v}_y = \dot{m}\Delta h_o \tag{2.2}$$

for an axial turbomachine. The variables are defined as: $\dot{W}$ is the power supplied or extracted from the blade row, $\dot{m}$ is the mass flow, ω is the angular velocity of the blade row, r is the radial position form the center of the engine, $\Delta\bar{v}_y$ is the overall change in tangential velocity across the blade row and Δh_o is the change in stagnation enthalpy across the blade row. The stagnation enthalpy is the total enthalpy of the working fluid at the stagnation point and is defined as $h_o = \Upsilon + \frac{P_o}{\rho_o}$, where Υ is internal energy, P_o is the stagnation pressure and ρ_o is the stagnation density.

Coupled with the overall change in the mass-flux averaged tangential velocity, $\Delta\bar{v}_y$, the distribution of $\bar{v}_y$ must be prescribed in the bladed region. This is accomplished by integrating the y-momentum equation from the upper blade surface to the lower blade surface, as shown by Dang [Dang 1995]

$$(P^+ - P^-) = \Delta P = \dot{m}\frac{d\bar{v}_y}{dx} \tag{2.3}$$

where P^+ and P^- are the blade surface pressures. This local rate of change of the prescribed quantity, $\bar{v}_y$ is shown to be related to the blade pressure loading which can be directly applied to the boundary conditions in the bladed region of the flow. The full derivation of this equation is given in Sec. (3.5.3).

Now that $\bar{v}_y$ has been chosen as the prescribed quantity for the inverse design, a relation between the blade surfaces and the flow field must be defined. The camberline and thickness must both be considered when designing the surface of the blades. Previous methods have designed only the camberline leaving the thickness distribution to be specified arbitrarily by the designer. In the case of turbomachinery blades, the upper and lower blade surfaces redirect the flow through a no-flux condition. Therefore the flow through the blade row is dictated by the blade surfaces, which are described as a camberline and thickness. To give the designer complete control of the final design, both must be considered in the inverse design method. With that said, caution must be taken when designing both the camberline and thickness because not all combinations may satisfy the no-flux condition on the upper and lower blade surfaces while remaining faithful to the prescribed turning requirements.

2.2 Blade Boundary Interpretation

To derive our inverse design technique we first need to develop an interpretation of how the flow field is influenced by geometry and then we will derive our equations for thickness and camberline within this framework.

2.2.1 Analysis Methods

In analysis mode, one is usually given a prescribed geometry and calculates the flow field around it. The geometry influences the flow field by forcing the fluid adjacent to the blades upper and lower surfaces to travel parallel to these surfaces. This phenomenon is described mathematically by the no flux condition

$$\vec{V} \cdot \vec{n} = 0 \Big|_{wall} \tag{2.4}$$

and can be seen graphically in Fig. (2.1). The geometry produces a deflection of the overall flow field, changes the velocity field locally and causes a pressure difference across the blades.

If one were interested only in obtaining the overall flow turning between the cascades blades, one could achieve the same flow field by replacing the physical geometry with a vortex sheet boundary condition between the leading and trailing edges of the geometry, shown in Fig. (2.2). This vortex sheet boundary condition would have to specify either the local velocities or the pressures on the upper and lower surfaces of the blade while upstream and downstream of the leading and trailing edges would have to specify a periodic boundary condition.

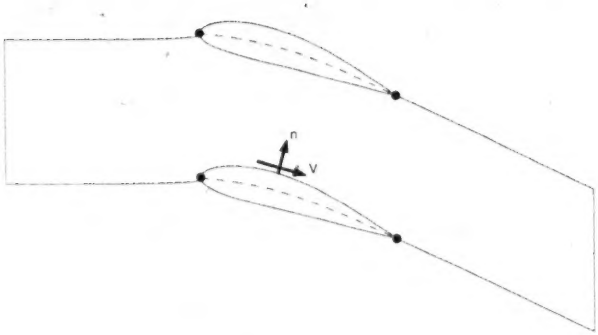

Figure 2.1: No-Flux Blade Boundaries

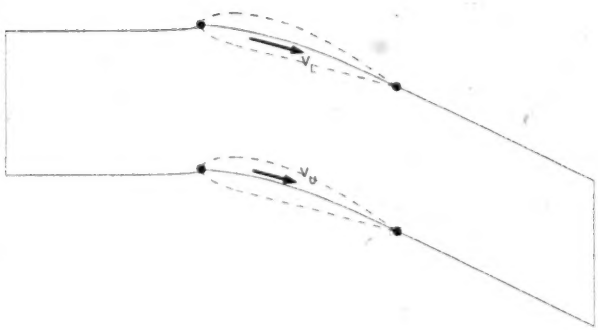

Figure 2.2: Vortex Sheet Blade Boundaries

2.2.2 Inverse Design Methods

In an inverse design, the goal is to achieve a specified turning distribution without knowing the shape of the physical geometry a priori. Given the global flow turning distribution, the pressure differences across the blades can be constructed through Eqn. (2.3). Together with an initial guess of the geometry, this pressure gradient can be used to construct the global flow field. With this solution to the global flow field, the velocities adjacent to the blades upper and lower surfaces can be extracted, and then use the no-flux condition, on the respective surfaces, to construct a second guess of the geometry. This procedure can be repeated until both the flow field and geometry converges upon a unique solution, where the geometry will produce the specified turning distribution

2.3 Relationship between Geometry and No-Flux Condition for Inverse Design

To construct the no-flux condition for the inverse design method we will start with a cascade of flat plates, shown in Fig. (2.3).

The first plate of the cascade can be defined by the surface α_1

$$y - x = 0 \tag{2.5}$$

whose normal can be written as

$$\vec{n_1} = \nabla(y - x) = \nabla(\alpha_1) \tag{2.6}$$

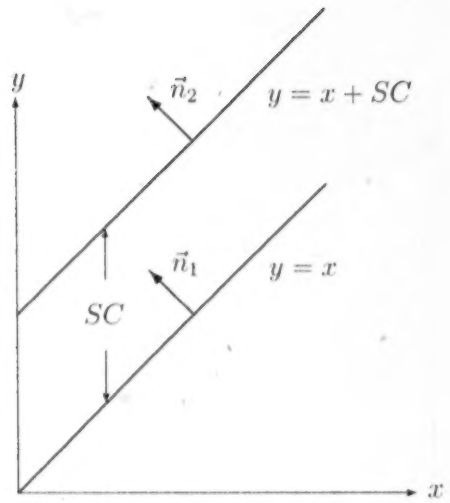

Figure 2.3: Sketch of Flat Plate Cascade

The second plate of the cascade is defined by the surface α_2

$$y - x - SC = 0 \tag{2.7}$$

where the spacing to chord ratio SC is constant and defined as the distance between flat plates. The normal to this surface can be written as

$$\vec{n_2} = \nabla(y - x - SC) = \nabla(\alpha_2) = \nabla(y - x) = \vec{n_1} = \nabla(\alpha_1) \tag{2.8}$$

with the no-flux conditions on each flat plate given by

$$\vec{V}_1 \cdot \vec{n}_1 = \vec{V}_1 \cdot \nabla(y - x) = \vec{V}_1 \nabla \cdot (\alpha_1) = 0 \tag{2.9}$$

$$\vec{V}_2 \cdot \vec{n}_2 = \vec{V}_2 \cdot \nabla(y - x) = \vec{V}_2 \nabla \cdot (\alpha_2) = 0 \tag{2.10}$$

where the velocity vector $\vec{V}_1 = (u_1, v_1)$ are the Cartesian velocities, u and v, along the first flat plate and similarly for $\vec{V}_2$ along the second flat plate.

If instead of a cascade of flat plates, we were given a cascade of infinitely thin turbomachinery blades whose camberlines were not constant, $f(x)$, shown in Fig. (2.4).

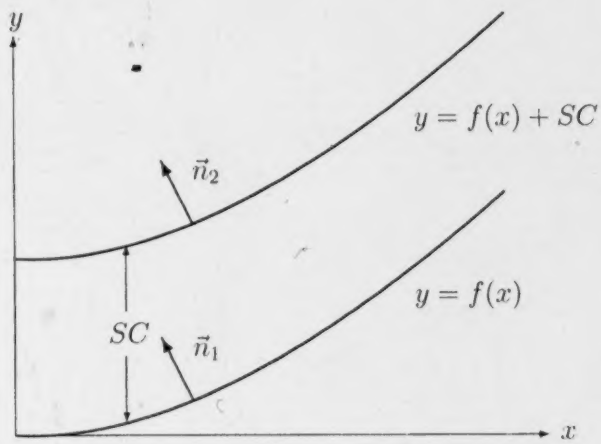

Figure 2.4: Sketch of Infinitely Thin Cascade

Following a similar derivation to previous, the normals to these thin cascade blades can now be written as

$$\vec{n_1} = \nabla(y - f(x)) = \nabla(\alpha_1) \tag{2.11}$$

and

$$\vec{n_2} = \nabla(y - f(x) - SC) = \nabla(\alpha_2) = \nabla(y - f(x)) = \nabla(\alpha_1) = \vec{n_1} \tag{2.12}$$

with the no-flux conditions on each thin blade given by

$$\vec{V_1} \cdot \vec{n}_1 = \vec{V_1} \cdot \nabla(y - f(x)) = \vec{V_1} \cdot \nabla(\alpha_1) = 0 \tag{2.13}$$

$$\vec{V_2} \cdot \vec{n}_2 = \vec{V_2} \cdot \nabla(y - f(x)) = \vec{V_2} \cdot \nabla(\alpha_2) = 0 \tag{2.14}$$

where the velocity vector $\vec{V_1} = (u_1, v_1)$ are the Cartesian velocities, u and v, along the first thin blade surface and similarly for $\vec{V_2}$ along the second thin blade surface.

Finally, adding the thickness distribution, $T(x)$, to the camberline $f(x)$ we obtain a cascade of turbomachinery blades, shown in Fig. (2.5).

Therefore, the normal of the upper blade surface, $\vec{n}^+$ can be written as

$$\vec{n}^+ = \nabla\left(y - \left(f(x) + \frac{T(x)}{2}\right)\right) = \nabla(\alpha^+) = 0 \tag{2.15}$$

and similarly for the lower surface, $\vec{n}^-$ can be written as

$$\vec{n}^- = \nabla\left(y - \left(f(x) - \frac{T(x)}{2}\right)\right) = \nabla(\alpha^-) = 0 \tag{2.16}$$

Finally, the no-flux conditions on the α^+ and α^- surfaces are written as

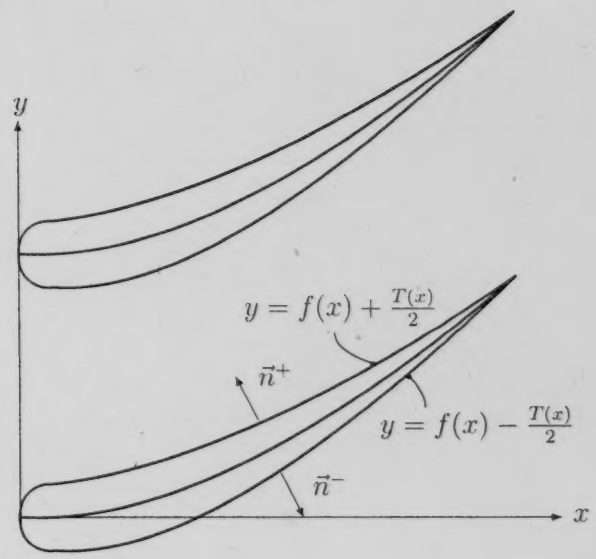

Figure 2.5: Sketch of Axial Turbomachinery Cascade

$$\vec{V}^+ \cdot \vec{n}^+ = \vec{V}^+ \cdot \nabla \left(y - \left(f(x) + \frac{T(x)}{2} \right) \right) = \vec{V}^+ \cdot \nabla(\alpha^+) = 0 \tag{2.17}$$

$$\vec{V}^- \cdot \vec{n}^- = \vec{V}^- \cdot \nabla \left(y - \left(f(x) - \frac{T(x)}{2} \right) \right) = \vec{V}^- \cdot \nabla(\alpha^-) = 0 \tag{2.18}$$

where the velocity vector $\vec{V}^+ = (u^+, v^+)$ are the Cartesian velocities, u and v, along the upper blade surface and similarly for $\vec{V}^-$ along the lower blade surface.

Expanding the ∇ operator

$$u^+ \left(\frac{\partial y}{\partial x} - \frac{\partial f}{\partial x} - \frac{1}{2}\frac{\partial T}{\partial x} \right) + v^+ \left(\frac{\partial y}{\partial y} - \frac{\partial f}{\partial y} - \frac{1}{2}\frac{\partial T}{\partial y} \right) = 0 \tag{2.19}$$

$$u^- \left(\frac{\partial y}{\partial x} - \frac{\partial f}{\partial x} + \frac{1}{2}\frac{\partial T}{\partial x} \right) + v^- \left(\frac{\partial y}{\partial y} - \frac{\partial f}{\partial y} + \frac{1}{2}\frac{\partial T}{\partial y} \right) = 0 \tag{2.20}$$

Since both f and T are functions of only x spatially these equations become

$$u^+ \frac{\partial f}{\partial x} + u^+ \frac{1}{2}\frac{\partial T}{\partial x} - v^+ = 0 \tag{2.21}$$

$$u^- \frac{\partial f}{\partial x} - u^- \frac{1}{2}\frac{\partial T}{\partial x} - v^- = 0 \tag{2.22}$$

These are the equations which govern the upper and lower blade surface. They are derived by determining the appropriate normal vector on the blade surface to satisfy the no-flux condition.

2.3.1 Camberline Generation

As derived by Medd [Medd 1998], a single equation by which the camberline can be calculated is constructed by adding Eqns. (2.21) and (2.22) together and including a pseudo-time derivative used to converge the solution to steady-state.

$$\frac{\partial f}{\partial t^*} + \bar{u}\frac{\partial f}{\partial x} + \frac{\Delta u}{4}\frac{\partial T}{\partial x} - \bar{v} = 0 \tag{2.23}$$

This addition of the no-flux equations ensures the camberline generator satisfies both no-flux equations independently at convergence. During the iteration procedure the camberline generator may allow mass flow through the blades surfaces but once the scheme has converged it satisfies the no-flux condition on the upper and lower blade surfaces while maintaining the prescribed turning requirements.

To prove this, refer to the grid boundaries of a flow domain, Fig. (2.6). Because it is a steady flow and there are no mass sources or sinks, the total mass of the fluid in the domain is constant. Therefore, whatever mass enters the domain must also leave the domain. Flow enters the domain through the left boundary (inflow) and out through right boundary (outflow). The inflow boundary is represented by line segment AH. The outflow boundary is represented by line segment DE. The solid blade surfaces are in the top and bottom boundaries. The fluid flows between two blades, called a passage, therefore the upper surface of the bottom blade is represented by line segment BC and the lower surface of the top blade is represented by line segment FG. The flow domain is extended upstream of the leading edge and downstream of the trailing edge. There are four more individual boundaries in the top and bottom boundaries. These boundaries are periodic because they represent the ability of the fluid to pass between separate passages. Instead of constructing numerous cascade passages, only the flow in a single passage is calculated. The periodic boundaries upstream of the leading edge are periodic with each other. This means the flow entering through the boundary represented by line segment AB is equal to the flow exiting through the boundary represented by line segment GH or vice versa. The periodic boundaries downstream of the trailing edge are also periodic with each other. This means the flow entering through the boundary represented by line segment CD is equal to the flow exiting through the boundary represented by line segment EF or vice versa.

Now that the description of the boundaries is complete, a mass flux balance can be performed on the entire domain. Mass flux through a specific

Figure 2.6: Flow Domain

boundary is represented by $\dot{m}$ with a subscript identifying the boundary in question. Conservation of mass states,

$$\underbrace{\dot{m}_{AH}}_{Inflow} + \underbrace{\dot{m}_{AB}}_{Periodic} + \underbrace{\dot{m}_{BC}}_{Upper\ Blade\ Surface} + \underbrace{\dot{m}_{CD}}_{Periodic} - \cdots$$
$$\underbrace{\dot{m}_{EF}}_{Periodic} - \underbrace{\dot{m}_{FG}}_{Lower\ Blade\ Surface} - \underbrace{\dot{m}_{GH}}_{Periodic} - \underbrace{\dot{m}_{DE}}_{Outflow} = 0 \quad (2.24)$$

the sum of the mass flux through all boundaries is equal to zero.

The mass flux through the boundary AB is equal to the mass flux through boundary GH because they are periodic with each other. The mass flux through the boundary CD is equal to the mass flux through boundary EF also because they are periodic with each other. Therefore,

$$\dot{m}_{AB} = \dot{m}_{GH} \quad \& \quad \dot{m}_{CD} = \dot{m}_{EF}$$

Substituting these into Eqn. (2.24),

$$\underbrace{\dot{m}_{AH}}_{Inflow} + \underbrace{\dot{m}_{BC}}_{Upper\ Blade\ Surface} - \underbrace{\dot{m}_{FG}}_{Lower\ Blade\ Surface} - \underbrace{\dot{m}_{DE}}_{Outflow} = 0 \quad (2.25)$$

In the case of camberline generation the modification of the blade surfaces are through the camberline because the prescribed thickness is constant. During the solution procedure, the camberline equation, Eqn. (2.23), can allow flux through the blade surfaces. This equation is the sum of the equations describing the upper surface, Eqn. (2.21), and the lower surface, Eqn. (2.22). It can be expressed as the sum of the mass flux through these surfaces.

$$\dot{m}_{BC} + \dot{m}_{FG} = 0 \quad (2.26)$$

and rearranged as

$$\dot{m}_{BC} = -\dot{m}_{FG} \quad (2.27)$$

Substituting this into Eqn. (2.25),

$$\underbrace{\dot{m}_{AH}}_{Inflow} + \underbrace{\dot{m}_{DE}}_{Outflow} - 2(\dot{m}_{FG}) = 0 \quad (2.28)$$

By the definition of continuity, when the code converges we know the mass flux through the inflow boundary AH has to equal the mass flux through the outflow boundary DE

$$\dot{m}_{AH} = \dot{m}_{DE} \quad (2.29)$$

Inserting this into Eqn. (2.28) finally yields

$$-2(\dot{m}_{FG}) = 0 \tag{2.30}$$

This says the mass flux through boundary FG has to equal to zero and from Eqn. (2.27) the mass flux through boundary BC also equals zero. Boundaries BC and FG are the blade surfaces. This proves that when the code converges the camberline generator guarantees the blade surfaces will have no mass flux through them and thus they are solid surfaces.

The equation used to generate a camberline was proven to ensure the blade surfaces will be solid once the code converges, however the design of the camberline alone is not enough to guarantee that the entire blade geometry generated will be acceptable. Even though a camberline can be designed from the prescribed quantities not all combinations of camberline and thickness will produce geometries which satisfy all the performance criteria. An example of this is shown in Fig. (2.7). When a constant prescribed thickness is left to be chosen arbitrarily and only the camberline is designed, the final geometry developed a discontinuity due to a passage shock. Using this design methodology there is no way to guarantee that the final geometry will yield satisfactory characteristics.

This illustrates the fact that even though a camberline can be designed not all combinations of camberline and thickness produce good geometries. The reason this can happen during the design procedure is that the thickness distribution is completely arbitrary and does not change throughout the procedure. Using methods where only the camberline is designed causes the

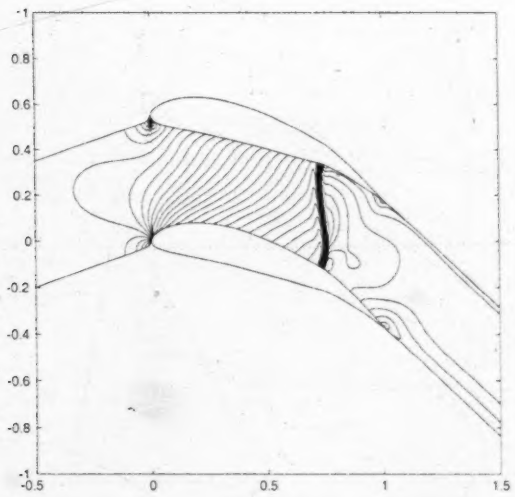

Figure 2.7: Discontinuous Geometry & Passage Shock: Mach No. Contours

designer to lose control over the final design and hence the performance of the blade.

2.3.2 Thickness Generation

The next step in the evolution of blade design is to now include the design of the thickness. Similar to the camberline, the thickness will be derived from a combination of the no-flux equations, Eqns. (2.21) and (2.22).

Starting with Eqns. (2.21) and (2.22) they are subtracted

$$\frac{\Delta u}{2}\frac{\partial f}{\partial x} + \bar{u}\frac{1}{2}\frac{\partial T}{\partial x} = \frac{\Delta v}{2} \tag{2.31}$$

rearranging the equation

$$\frac{1}{2}\bar{u}\frac{\partial T}{\partial x} = \frac{\Delta v}{2} - \frac{\Delta u}{2}\frac{\partial f}{\partial x} \tag{2.32}$$

To simplify the analysis let

$$A = \bar{u} \tag{2.33}$$

$$B = \frac{\Delta v}{2} - \frac{\Delta u}{2}\frac{\partial f}{\partial x} \tag{2.34}$$

Therefore,

$$A\frac{1}{2}\frac{\partial T}{\partial x} = B \tag{2.35}$$

To control the thickness at both the leading and trailing edges, the thickness equation is derived as a second order equation with two boundary conditions. Following the method of Whitham [Whitham 1974], two first order wave equations can be converted into a single second order wave equations. The solution of the thickness will be steady, therefore a time derivative can be added to Eqn. (2.35). The two first order wave equations are obtained by adding both a positive and negative time derivative to Eqn. (2.35). Writing them in operator form

$$\left(\frac{\partial}{\partial t} + A\frac{\partial}{\partial x}\right)\frac{1}{2}T = B \tag{2.36}$$

$$\left(-\frac{\partial}{\partial t} + A\frac{\partial}{\partial x}\right)\frac{1}{2}T = B \tag{2.37}$$

Apply the operator from Eqn. (2.37), $\left(-\frac{\partial}{\partial t} + A\frac{\partial}{\partial x}\right)$, to Eqn. (2.36),

$$\left(-\frac{\partial}{\partial t}+A\frac{\partial}{\partial x}\right)\left(\frac{\partial}{\partial t}+A\frac{\partial}{\partial x}\right)\frac{1}{2}T=\left(-\frac{\partial}{\partial t}+A\frac{\partial}{\partial x}\right)B \tag{2.38}$$

Expand the the term on the right-hand side

$$\left(-\frac{\partial^2}{\partial t^2}-\frac{\partial}{\partial t}\left(C\frac{\partial}{\partial x}\right)+A\frac{\partial^2}{\partial x\partial t}+A\frac{\partial}{\partial x}\left(A\frac{\partial}{\partial x}\right)\right)\frac{1}{2}T=$$

$$\left(-\frac{\partial}{\partial t}+A\frac{\partial}{\partial x}\right)B \tag{2.39}$$

Conversely, perform the same procedure for Equation (2.37)

$$\left(-\frac{\partial^2}{\partial t^2}+\frac{\partial}{\partial t}\left(A\frac{\partial}{\partial x}\right)-A\frac{\partial^2}{\partial x\partial t}+A\frac{\partial}{\partial x}\left(A\frac{\partial}{\partial x}\right)\right)\frac{1}{2}T=$$

$$\left(\frac{\partial}{\partial t}+A\frac{\partial}{\partial x}\right)B \tag{2.40}$$

Adding Equations (2.39) and (2.40) yields a second-order equation for the thickness based on the surface velocities and camberline.

$$\frac{\partial^2 T}{\partial t^2}=A\frac{\partial}{\partial x}\left(A\frac{\partial T}{\partial x}\right)-2A\frac{\partial B}{\partial x}=\frac{\partial T}{\partial t} \tag{2.41}$$

Due to the difficulty in solving the second order thickness equation using a multi-step time advancement scheme with a second derivative of thickness with respect to time, it is exchanged with a first derivative in time. This is possible because the solution of the thickness will be steady. The derivative of thickness with respect to time is included to allow the use of multi-step time advancement scheme. The benefit of this scheme over others is that the stability of the equation is easily controlled.

A combination of the no-flux equations is desired that removes the no-flux condition on the upper and lower blade surfaces. The reason for this is the thickness equation in any other form may not be easily solved and a solution will not always be attainable. An obvious example where this would be true is the design of the thickness of turbine blades with a prescribed zero camberline shown in Fig. (2.8).

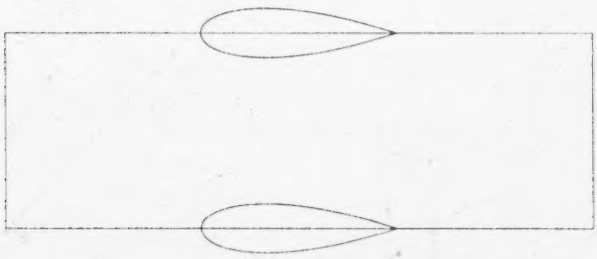

Figure 2.8: Blades with Zero Camberline

A zero camberline is a straight horizontal line connecting the leading and trailing edges. The lower surface would result from the addition of half of the thickness to the zero camberline and similarly, the upper surface surface would result the subtraction of half of the thickness from the zero camberline. The thickness is symmetric about the the camberline therefore modification of the thickness will cause equal but opposite changes in the blade surfaces. Because of this there is no way for the thickness to change the overall direction of the flow while maintaining the no-flux condition on the blade surfaces. This illustrates that a solution would be difficult to attain

when you construct the thickness equation such that the no-flux conditions on the upper and lower surfaces of the blade are enforced. If, however the no-flux condition is removed then a solution can be obtained because mass-flux is allowed through the blade surfaces and can now turn the flow according to the specified turning requirements. Therefore the equation for the thickness was derived to allow the flux through the blade surfaces.

To prove this recall Fig. (2.6) and its description from Sec. (2.3.1). Another mass flux balance can be performed on the entire domain. Mass flux through a specific boundary is represented by $\dot{m}$ with a subscript identifying the boundary in question. Conservation of mass states,

$$\underbrace{\dot{m}_{AH}}_{Inflow} + \underbrace{\dot{m}_{AB}}_{Periodic} + \underbrace{\dot{m}_{BC}}_{Upper\ Blade\ Surface} + \underbrace{\dot{m}_{CD}}_{Periodic} - \cdots$$
$$\underbrace{\dot{m}_{EF}}_{Periodic} - \underbrace{\dot{m}_{FG}}_{Lower\ Blade\ Surface} - \underbrace{\dot{m}_{GH}}_{Periodic} - \underbrace{\dot{m}_{DE}}_{Outflow} = 0 \quad (2.42)$$

the sum of the mass flux through all boundaries is equal to zero.

The mass flux through the boundary AB is equal to the mass flux through boundary GH because they are periodic with each other. The mass flux through the boundary CD is equal to the mass flux through boundary EF also because they are periodic with each other. Therefore,

$$\dot{m}_{AB} = \dot{m}_{GH} \quad \& \quad \dot{m}_{CD} = \dot{m}_{EF}$$

Substituting these into Eqn. (2.42),

$$\underbrace{\dot{m}_{AH}}_{Inflow} + \underbrace{\dot{m}_{BC}}_{Upper\ Blade\ Surface} - \underbrace{\dot{m}_{FG}}_{Lower\ Blade\ Surface} - \underbrace{\dot{m}_{DE}}_{Outflow} = 0 \quad (2.43)$$

In the case of thickness generation the modification of the blade surfaces are through the thickness because the prescribed camberline is constant. During the solution procedure the thickness equation, Eqn. (2.41) can allow flux through the blade surfaces. This equation is the difference of equations describing the upper surface, Eqn. (2.21), and the lower surface, Eqn. (2.22). It can be expressed as the difference of the mass flux through these surfaces.

$$\dot{m}_{BC} - \dot{m}_{FG} = 0 \tag{2.44}$$

and rearranged as

$$\dot{m}_{BC} = \dot{m}_{FG} \tag{2.45}$$

Substituting this into Eqn. (2.43),

$$\underbrace{\dot{m}_{AH}}_{Inflow} + \underbrace{\dot{m}_{FG}}_{Upper\ Blade\ Surface} - \underbrace{\dot{m}_{FG}}_{Lower\ Blade\ Surface} - \underbrace{\dot{m}_{DE}}_{Outflow} = 0 \tag{2.46}$$

By the definition of continuity, when the code converges we know the mass flux through the inflow boundary AH has to equal the mass flux through the outflow boundary DE

$$\dot{m}_{AH} = \dot{m}_{DE} \tag{2.47}$$

Inserting this into Eqn. (2.46) finally yields

$$\dot{m}_{FG} - \dot{m}_{FG} = 0 \tag{2.48}$$

This states the mass flux through boundary FG can be to equal to zero, the no-flux condition, or not necessarily equal to zero, the periodic condition. This proves that when the code converges the thickness generator can allow flux through the blade surfaces.

Eqn. (2.31) is used derive the thickness equation. This equation is the subtraction of the no-flux equations, Eqns. (2.21) and (2.22). The implication is that when the solution has converged global mass conservation will be satisfied but not necessarily on the individual blade surfaces. This implies that the mass flux entering one blade surface exits the other blade surface, or simply are periodic boundaries. Even though mass flux is allowed through the blade surfaces, it now will allow a solution to the thickness equation, where a solution previously would have been difficult. The design of the thickness now feels the no-flux conditions on the upper and lower blade surfaces, but does not necessarily enforce them. Once the solution for the thickness has converged, the camberline generator is then turned on to enforce the no-flux conditions on each blade surface and to complete the turning requirements. The entire blade shape is designed from a thickness and a camberline which both are designed with influence from the prescribed turning distribution.

2.3.3 Thickness Correction and Update

Problems at the leading edge due to the excessive shearing of the grid were found to significantly affect the solution of the thickness downstream. Therefore, special consideration of the calculation of the thickness needs attention.

To allow more detailed attention of the thickness at the leading edge, the thickness equation is written in terms of a fixed thickness, T_{fixed}, and a corrected thickness term T_{corr}

$$T(x) = T_{fixed}(x) + T_{corr}(x) \tag{2.49}$$

Rederiving Eqn. (2.41) with the inclusion of this correction equation

$$\frac{\partial\left(T_{fixed} + T_{corr}\right)}{\partial t} = A\frac{\partial}{\partial x}\left(A\frac{\partial\left(T_{fixed} + T_{corr}\right)}{\partial x}\right) - 2A\frac{\partial B}{\partial x} \tag{2.50}$$

Expanding the terms containing both T_{fixed} and T_{corr} and ignoring the $\frac{\partial\left(T_{fixed}\right)}{\partial t}$ because it is constant. The equation used to solve for the thickness correction is

$$\frac{\partial T_{corr}}{\partial t} = A\frac{\partial}{\partial x}\left(A\frac{\partial T_{fixed}}{\partial x}\right) + A\frac{\partial}{\partial x}\left(A\frac{\partial T_{corr}}{\partial x}\right) - 2A\frac{\partial B}{\partial x} \tag{2.51}$$

and reiterating,

$$\begin{aligned} A &= \bar{u} \\ B &= \frac{\Delta v}{2} - \frac{\Delta u}{2}\frac{\partial f}{\partial x} \end{aligned}$$

Continuing with the analysis into a method to minimize the effects of the leading edge, a new equation similar to Eqn. (2.49) was used to update the thickness. A new strategy was needed to allow local modification of the thickness near the leading edge. A function which would only allow small

changes of the thickness near the leading edge and increase toward the trailing edge was used. The new thickness update equation is written as

$$T = T_{fixed}(x) + \mu(x)T_{corr}(x) \tag{2.52}$$

The initial function chosen was a hyperbolic tangent function of the form

$$\mu = 0.9\left(\frac{\tanh(px - q) + 1}{2}\right) \tag{2.53}$$

where various values of p, q were tried and x is the axial location along the chord from leading edge to trailing edge. The value of 0.9 is a limiting factor used to help minimize pollution of the leading edge effects downstream. An example, where $p = 15$ and $q = 3$ were used, with the actual function is shown along with the final blade design in Fig. (2.9)

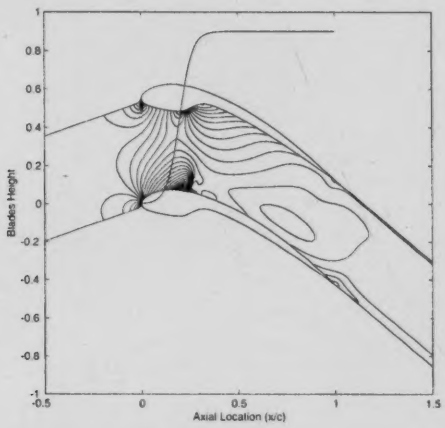

Figure 2.9: Hyperbolic Tangent Function: Mach No. Contours

This function yielded undesirable results, shown by the final designed blade. Due to the nature of the hyperbolic tangent function, a large bump developed in the leading edge region

Instead a function of the following form was chosen

$$\mu = 0.9\left(1 - e^{-rx}\right) \tag{2.54}$$

where various values of r were tried. This exponential function was chosen because it avoided introducing bumps into the blade surfaces as was the case with the hyperbolic tangent function. A value of $r = 8$ was chosen to be used for the leading edge function treatment, shown in Fig. (2.10). This value was chosen because at 0.4 axial chord location the value of the function was approximately at 95% of the maximum and was found that this was sufficiently far enough downstream of the leading edge to avoid any adverse affects.

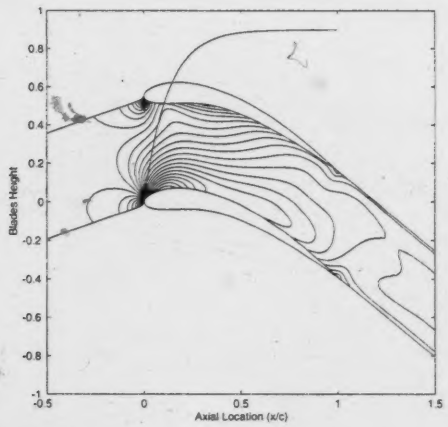

Figure 2.10: Exponential Function: Mach No. Contours

2.4 Conservation Equations

In a control volume the equations of mass, momentum and energy of an inviscid, compressible fluid can be written, respectively, in integral form as

$$\frac{D}{Dt}\iiint_{\forall} \rho \, d\forall = \iiint_{\forall} \left[\frac{D\rho}{Dt} + \rho \nabla \cdot \vec{V}\right] d\forall = 0 \tag{2.55}$$

$$\frac{D}{Dt}\iiint_{\forall} \rho \vec{V} \, d\forall + \iint_{S} P\vec{n} \, dS = 0 \tag{2.56}$$

$$\frac{D}{Dt}\iiint_{\forall} \rho e_t \, d\forall + \iint_{S} P\vec{V} \cdot \vec{n} \, dS = 0 \tag{2.57}$$

These equations are integrated over the control volume $\forall$ bounded by the surface S. The unit vector $\vec{n}$ acts outward normal to dS which is a small element of the surface S. The variable ρ is the density, $\vec{V}$ is the velocity vector of the fluid, P is the pressure and $e_t = \Upsilon + \frac{\vec{V}\cdot\vec{V}}{2}$ is the total energy of the fluid, with Υ as the internal energy.

The integral form of the equations, Eqns. (2.55)−(2.57), can be converted to differential form by use of the Transport theorem [Serrin 1959] and converting the surface integrals to volume integrals using the divergence theorem. Written in both vector and index notation

$$\frac{\partial \rho}{\partial t} + \nabla \cdot (\rho \vec{V}) = 0 \quad ; \quad \frac{\partial \rho}{\partial t} + \frac{\partial (\rho v_i)}{\partial x_i} = 0 \tag{2.58}$$

$$\rho \frac{D\vec{V}}{Dt} = -\nabla P \quad ; \quad \rho \frac{Dv_i}{Dt} = -\frac{\partial P}{\partial x_i} \tag{2.59}$$

$$\rho \frac{De_t}{Dt} = -\nabla (P\vec{V}) \quad ; \quad \rho \frac{De_t}{Dt} = -\frac{\partial (Pv_i)}{\partial x_i} \tag{2.60}$$

Expressing Eqns. (2.58)−(2.60) in conservation form (see derivation Appendix A):

$$\frac{\partial \rho}{\partial t} + \frac{\partial (\rho v_i)}{\partial x_i} = 0 \tag{2.61}$$

$$\frac{\partial \rho v_i}{\partial t} + \frac{\partial (\rho v_i v_j)}{\partial x_i} = -\frac{\partial P}{\partial x_i} \tag{2.62}$$

$$\frac{\partial (e_t)}{\partial t} + \frac{\partial (e_t v_i)}{\partial x_i} = -\frac{\partial (P v_i)}{\partial x_i} \tag{2.63}$$

The differential form of the equations of motion Eqn. (2.61)−(2.63) can now be expressed in the two dimensional Cartesian coordinate system. The following system of first-order partial differential equations results,

$$\frac{\partial \vec{w}}{\partial t} + \frac{\partial \vec{E}}{\partial x} + \frac{\partial \vec{F}}{\partial y} = 0 \tag{2.64}$$

Where:

$$\vec{w} = \begin{Bmatrix} \rho \\ \rho u \\ \rho v \\ \rho e_t \end{Bmatrix} \qquad \vec{E} = \begin{Bmatrix} \rho u \\ \rho u^2 + P \\ \rho uv \\ (\rho e_t + P)u \end{Bmatrix} \qquad \vec{F} = \begin{Bmatrix} \rho v \\ \rho uv \\ \rho v^2 + P \\ (\rho e_t + P)v \end{Bmatrix}$$

The vector $\vec{w}$ is the conservative variable vector and the vectors $\vec{E}$ and $\vec{F}$ are the flux vectors. The variables u and v are the Cartesian velocity components of the velocity in the x and y directions respectively and ρ, P and e_t are the same as previously defined.

The system of equations used for the inverse design will be the integral form of Eqn. (2.64) where the spatial derivatives are converted from volume integrals to surface integrals using the divergence theorem

$$\int_{\forall} \frac{\partial \vec{w}}{\partial t} d\forall + \oint_{s} \left(\vec{E} n_x + \vec{F} n_y \right) dS = 0 \tag{2.65}$$

For closure, the pressure and total energy of a calorically perfect gas are related using the equation of state:

$$P = (\gamma - 1) \left(\rho e_t - \rho \frac{\vec{V} \cdot \vec{V}}{2} \right) \tag{2.66}$$

where $\gamma = 1.4$ is the ratio of specific heat capacities for air.

These equations coupled with the equation for the camberline and thickness, combine to make the complete system of equations needed for the solution of the inverse design problem.

2.4.1 Equation Classification

By rewriting the partial differential form of equations of motion Eqn. (2.64) in quasi-linear form as follows

$$\frac{\partial \vec{w}}{\partial t} + \overline{\overline{A}}_x \frac{\partial \vec{w}}{\partial x} + \overline{\overline{A}}_y \frac{\partial \vec{w}}{\partial y} = 0 \tag{2.67}$$

Where:

$$\overline{\overline{A}}_x \equiv \frac{\partial \vec{E}}{\partial \vec{w}} =$$

$$\begin{bmatrix} 0 & 1 & 0 & 0 \\ \frac{\gamma-3}{2}u^2 + \frac{\gamma-1}{2}v^2 & (3-\gamma)u & -(\gamma-1)v & (\gamma-1) \\ -uv & v & u & 0 \\ -\gamma u \frac{e_t}{\rho} + (\gamma-1)u|\vec{V}|^2 & \gamma \frac{e_t}{\rho} - \frac{\gamma-1}{2}(v^2+3u^2) & -(\gamma-1)uv & \gamma u \end{bmatrix}$$

$$\overline{\overline{A}}_y \equiv \frac{\partial \vec{F}}{\partial \vec{w}} =$$

$$\begin{bmatrix} 0 & 0 & 1 & 0 \\ -uv & v & u & 0 \\ \frac{\gamma-3}{2}v^2 + \frac{\gamma-1}{2}u^2 & -(\gamma-1)u & (3-\gamma)v & (\gamma-1) \\ -\gamma v\frac{e_t}{\rho} + (\gamma-1)v|\vec{V}|^2 & -(\gamma-1)uv & \gamma\frac{e_t}{\rho} - \frac{\gamma-1}{2}(u^2+3v^2) & \gamma v \end{bmatrix}$$

it is possible to classify this system of equations.

The eigenvalues of the two matrices $\overline{\overline{A}}_x$ and $\overline{\overline{A}}_y$ define the behavior of the solution of the equations of motion. If the eigenvalues of the matrices are all real, the system of equations is said to be hyperbolic. The eigenvalues are obtained as solutions of the equations

$$det\left|\lambda_x \overline{\overline{I}} - \overline{\overline{A}}_x\right| = 0\,,\; det\left|\lambda_y \overline{\overline{I}} - \overline{\overline{A}}_y\right| = 0 \tag{2.68}$$

Where λ_x and λ_y are the eigenvalues of $\overline{\overline{A}}_x$ and $\overline{\overline{A}}_y$ respectively and $\overline{\overline{I}}$ is the identity matrix.

The eigenvalues of the matrices $\overline{\overline{A}}_x$ and $\overline{\overline{A}}_y$ can be shown to be

$$\begin{aligned} \lambda_{x_1} = \lambda_{x_2} &= u & \lambda_{y_1} = \lambda_{y_2} &= v \\ \lambda_{x_3} &= u + a & \lambda_{y_3} &= v + a \\ \lambda_{x_4} &= u + a & \lambda_{y_4} &= v + a \end{aligned}$$

where a is the speed of sound and is defined by $a = \sqrt{\gamma R \Theta}$.

2.4.2 Non-dimensionalization

The non-dimensional form of the equations can be obtained by using the dimensional variables

P_o = upstream stagnation pressure

Θ_o = upstream stagnation temperature

R = gas constant

c = axial chord length

to non-dimensionalize the variables.

$$\tilde{x} = \frac{x}{c} \quad ; \quad \tilde{y} = \frac{y}{c}$$

$$\tilde{u} = \frac{u}{\sqrt{\gamma R \Theta_o}} \quad ; \quad \tilde{v} = \frac{v}{\sqrt{\gamma R \Theta_o}}$$

$$\tilde{P} = \frac{P}{P_o} \quad ; \quad \tilde{\rho} = \frac{\rho R \Theta_o}{P_o}$$

Substitution of these non-dimensional variables into the inverse design equations results in a set of equations that look similar to the dimensional form of the equations.

Chapter 3

Numerical Methods

3.1 Solution Sequence

The numerical approximations for the equations derived in the previous chapter are given in the following sections. These numerical equations are applied in the following sequence for a single stage of the time advancement scheme to converge the solution to steady state.

I. *Update Conservation Equations*

Begin by calculating the artificial dissipation for each grid cell. Next the flux vectors of the conservation equations Eqns. (2.65) are calculated. The grid geometrics, which are the surface projections of each face of a grid cell, are then calculated and multiplied by the appropriate flux vectors. Once this has been completed all components for a single cell are added together along with the artificial dissipation to create the residuals for each cell. The residuals are then used to update the solution through the stage equation

$$\vec{W}^{(K)} = \vec{W}^{(0)} + \alpha_K \, \Delta t \, \vec{R}(\vec{W}^{(K-1)})$$

where $\vec{W}$ is the solution vector, K is stage number, Δt is the time step, α_K is the stage coefficient and $\vec{R}(\vec{W}^{(K-1)})$ is the residual.

Once the solutions to the conservation equations has been updated, two things can happen: the calculation of the thickness or the calculation of the camberline.

II. A. *Update Thickness*

Read the updated solution vector of the flow equations and the camberline. Calculate the u and v Cartesian velocities and interpolate them to the blade surfaces. Use these surface velocities along with the camberline to calculate the residual of the thickness correction equation, Eqn. (2.51). Update the solution of the thickness correction through a two-stage Runge-Kutta time advancement scheme used for the thickness. Once the thickness correction has been updated, calculate the new thickness with the thickness update equation

$$T^N = T_{fixed} + \mu \, T^N_{corr}$$

where T^N is the updated thickness, T_{fixed} is the fixed thickness, μ is the correction function, T^N_{corr} is the updated thickness correction and N is the time level. The updated thickness is then used to reconstruct the y-coordinates.

B. *Update Camberline*

Read the updated solution vector of the flow equations and the thickness. Calculate the u and v Cartesian velocities and interpolate them to the blade surfaces. Use these surface velocities along with the thickness to calculate the residual of the camberline equation, Eqn. (2.23). Update the solution of the camberline through the same time advancement scheme used for the flow equations. The new camberline is then used to reconstruct the y-coordinates.

III. *Update Turning Schedule*

Update the schedule of the actual turning $\bar{v}_y$ through the passage using the velocities from the updated solution vector. The updated turning distribution will be used in the next time step to calculate the boundary pressures through the pressure/momentum boundary condition Eqn. (2.3).

This is the series of steps taken to complete one stage of a single pseudo-time step used for the convergence of inverse design procedure.

3.2 Thickness Generator

Reiterating the thickness correction equation, Eqn. (2.51)

$$\frac{\partial T_{corr}}{\partial t} = A\frac{\partial}{\partial x}\left(A\frac{\partial T_{fixed}}{\partial x}\right) + A\frac{\partial}{\partial x}\left(A\frac{\partial T_{corr}}{\partial x}\right) - 2A\frac{\partial B}{\partial x}$$

Because the numerically approximated derivatives are derived using a

Taylor series expansion under the assumption of a uniform grid, Eqn. (2.51) is transformed into a generalized coordinate system. Using the transformation

$$\xi = \xi(x) \Longleftrightarrow x = x(\xi) \tag{3.1}$$

Performing the chain rule, Eqn. (2.49) becomes

$$\frac{\partial T_{corr}}{\partial t} = A\frac{\partial}{\partial \xi}\left(A\frac{\partial T_{fixed}}{\partial \xi}\frac{\partial \xi}{\partial x}\right)\frac{\partial \xi}{\partial x} + A\frac{\partial}{\partial \xi}\left(A\frac{\partial T_{corr}}{\partial \xi}\frac{\partial \xi}{\partial x}\right)\frac{\partial \xi}{\partial x} + 2A\frac{\partial B}{\partial \xi}\frac{\partial \xi}{\partial x} \tag{3.2}$$

To simplify, the definition of the determinant of the Jacobian and its inverse in one dimension respectively are

$$|J| = \frac{\partial x}{\partial \xi} \qquad ; \qquad \frac{1}{|J|} = \frac{\partial \xi}{\partial x} \tag{3.3}$$

Substitution of this into Eqn. (3.2)

$$\frac{\partial T_{corr}}{\partial t} = \frac{A}{|J|}\frac{\partial}{\partial \xi}\left(\frac{A}{|J|}\frac{\partial T_{fixed}}{\partial \xi}\right) + \frac{A}{|J|}\frac{\partial}{\partial \xi}\left(\frac{A}{|J|}\frac{\partial T_{corr}}{\partial \xi}\right) + \frac{2A}{|J|}\frac{\partial B}{\partial \xi} \tag{3.4}$$

3.2.1 Time Advancement

The solution to the thickness equation is steady, therefore a two stage Runge-Kutta time-stepping scheme was chosen to converge the residual of the thickness correction to zero.

$$\begin{aligned} T_{corr}^{(0)} &= T_{corr}^{N} \\ T_{corr}^{(1)} &= T_{corr}^{(0)} + \alpha_1 \Delta t \vec{R}_T\left(T_{corr}^{(0)}\right) \\ T_{corr}^{(2)} &= T_{corr}^{(0)} + \alpha_2 \Delta t \vec{R}_T\left(T_{corr}^{(1)}\right) \\ T_{corr}^{N+1} &= T_{corr}^{(2)} \end{aligned} \tag{3.5}$$

The stage coefficients, α_1 and α_2 were chosen to be $\frac{1}{2}$ and 1, respectively, to maintain second order time accuracy. The residual of the thickness correction $\vec{R}_T$ is defined as

$$\vec{R}_T = \frac{A}{|J|}\frac{\partial}{\partial x}\left(\frac{A}{|J|}\frac{\partial T_{fixed}}{\partial \xi}\right) + \frac{A}{|J|}\frac{\partial}{\partial x}\left(\frac{A}{|J|}\frac{\partial T_{corr}}{\partial \xi}\right) + \frac{2A}{|J|}\frac{\partial B}{\partial \xi} \tag{3.6}$$

The thickness correction calculated from Eqn. (3.5) alone is not enough to update the thickness at every time level. The thickness update equation, Eqn. (2.52), is used to update the thickness every time level. Given a thickness correction calculated at the new time level, $T_{corr_i}^{N+1}$ the thickness is updated at the same new time level from Eqn. (2.52)

$$T_i^{N+1} = T_{fixed_i} + \mu_i T_{corr_i}^{N+1} \tag{3.7}$$

where $\mu_i = 0.9\,(1 - e^{-8x_i})$ is used.

3.2.2 Spatial Discretization

To allow for higher accuracy when calculating Eqn. (3.6), the spatial derivatives are constructed with fourth order central finite differences

$$\begin{aligned}\vec{R}_T &= \frac{A_i}{|J|_i}\left(\frac{G_{i+\frac{3}{2}} + 27G_{i+\frac{1}{2}} - 27G_{i-\frac{1}{2}} + G_{i-\frac{3}{2}}}{30\Delta\xi}\right) \\ &+ \frac{A_i}{|J|_i}\left(\frac{H_{i+\frac{3}{2}} + 27H_{i+\frac{1}{2}} - 27H_{i-\frac{1}{2}} + H_{i-\frac{3}{2}}}{30\Delta\xi}\right) \\ &+ \frac{2A_i}{|J|_i}\frac{B_{i+1} - B_{i-1}}{2\Delta\xi}\end{aligned} \tag{3.8}$$

where

$$G_{i+\frac{1}{2}} = \frac{A_{i+\frac{1}{2}}}{|J|_{i+\frac{1}{2}}} \frac{\partial T_{fixed}}{\partial \xi}\bigg|_{i+\frac{1}{2}} \quad ; \quad H_{i+\frac{1}{2}} = \frac{A_{i+\frac{1}{2}}}{|J|_{i+\frac{1}{2}}} \frac{\partial T_{corr}}{\partial \xi}\bigg|_{i+\frac{1}{2}} \tag{3.9}$$

and the respective derivatives are written as

$$\frac{\partial T}{\partial \xi}\bigg|_{i+\frac{1}{2}} = \frac{T_{i+2} + 27T_{i+1} - 27T_i - T_{i-1}}{30\Delta\xi} \tag{3.10}$$

With $\Delta\xi$ chosen to be 1 for simplicity.

The velocity combinations A_i and B_i are interpolated from the blade surface velocities in the neighbouring cell centers.

$$\begin{aligned} A_i &= (\bar{u})_i \\ B_i &= \left(\frac{\Delta v}{2}\right)_i - \left(\frac{\Delta u}{2}\bar{v}\right)_i \end{aligned}$$

The velocity components of A_i and B_i are defined as

$$\begin{aligned} \bar{u} &= \frac{1}{2}\left(u_i^+ + u_i^-\right) \quad ; \quad \bar{v} = \frac{1}{2}\left(v_i^+ + v_i^-\right) \\ \Delta u &= \left(u_i^+ - u_i^-\right) \quad ; \quad \Delta v = \left(v_i^+ - v_i^-\right) \end{aligned}$$

and the surface velocities used in the velocity combinations are

$$\begin{aligned} u_i^+ &= \frac{1}{2}\left(u^i_{camb} + u_{i,j=2}\right) \quad ; \quad v_i^+ = \frac{1}{2}\left(v^i_{camb} + v_{i,j=2}\right) \\ u_i^- &= \frac{1}{2}\left(u^i_{camb} + u_{i,j=MY}\right) \quad ; \quad v_i^- = \frac{1}{2}\left(v^i_{camb} + v_{i,j=MY}\right) \\ u^i_{camb} &= \frac{1}{2}\left(u_{i,j=2} + u_{i,j=MY}\right) \quad ; \quad v^i_{camb} = \frac{1}{2}\left(v_{i,j=2} + v_{i,j=MY}\right) \end{aligned}$$

The velocities $u_{i,j=2}$ and $u_{i,j=MY}$ from the conservation equations refer to the cell-centered values in the cells adjacent to the upper and lower blade surfaces respectively.

3.2.3 Boundary Conditions

The benefit of posing the thickness equation in terms of second order derivatives is to allow control over the thickness at both the leading and trailing edges. This was done to ensure the leading and trailing edges would both be closed. Thus the thickness is set to zero there and at any point upstream of the leading edge and downstream of the trailing edge.

$$T(le) = T(te) = 0 \tag{3.11}$$

3.2.4 Numerical Stability and Time Step

The thickness equation is solved using a explicit multistep time advancement scheme similar to that of the flow equations. Therefore, a Von Neumann stability analysis is used to find an appropriate time step for the thickness equation. The equation used to solve for the thickness is similar to a non-linear non-homogeneous diffusive equation. To simplify the analysis a linear homogeneous diffusive equation of the form

$$\frac{\partial y}{\partial t} = A^2 \frac{\partial^2 y}{\partial x^2} \tag{3.12}$$

is used as a model equation, assuming A is constant.

Discretizing the model equation using a second order accurate central finite difference for the spatial term and a forward difference for the time derivative and following the analysis of Patankar [Patankar 1986].

$$\frac{y_i^{N+1} - y_i^N}{\Delta t} = A^2 \left(\frac{y_{i+1}^N - 2y_i^N + y_{i-1}^N}{\Delta x^2} \right) \tag{3.13}$$

If the exact solution of the equation is y_i^N and the numerical solution is represented as $\tilde{y}_i^N$ then the difference between these values is the error ε_i^N. This can be expressed as:

$$\tilde{y}_i^N = y_i^N - \varepsilon_i^N \tag{3.14}$$

By substituting Eqn. (3.14) into Eqn. (3.13) the equation can be separated into two parts. The first is a function of the exact solution which is equal to zero and can be removed, leaving an equation that is a function of the error ε_i^N.

$$\frac{\varepsilon_i^{N+1} - \varepsilon_i^N}{\Delta t} = A^2 \left(\frac{\varepsilon_{i+1}^N - 2\varepsilon_i^N + \varepsilon_{i-1}^N}{\Delta x^2} \right) \tag{3.15}$$

The error term can now be decomposed using Fourier modes.

$$\begin{aligned} \varepsilon_i^N &= e^{At} e^{ikx} \\ \varepsilon_{i+1}^{N+1} &= e^{A(t+\Delta t)} e^{ik(x+\Delta x)} \end{aligned}$$

Substituting the Fourier modes into Eqn. (3.15)

$$\frac{e^{A(t+\Delta t)}e^{ikx} - e^{At}e^{ikx}}{\Delta t} = A^2\left(\frac{e^{At}e^{ik(x+\Delta x)} - 2e^{At}e^{ikx} + e^{At}e^{ik(x-\Delta x)}}{(\Delta x)^2}\right) \quad (3.16)$$

and dividing through by $e^{At}e^{ikx}$.

$$\frac{e^{At}}{\Delta t} = A^2\left(\frac{e^{ik\Delta x} - 2 + e^{-ik\Delta x}}{(\Delta x)^2}\right) \quad (3.17)$$

Rearranging Eqn. (3.17) gives:

$$e^{At} = 1 + \frac{A^2\Delta t}{(\Delta x)^2}\left(e^{ik\Delta x} + e^{-ik\Delta x} - 2\right) \quad (3.18)$$

First using the series identity $\cos(x) = \frac{e^{ix}+e^{-ix}}{2}$ in Eqn. (3.18)

$$e^{At} = 1 + \frac{2A^2\Delta t}{(\Delta x)^2}\left(\cos(k\Delta x) - 1\right) \quad (3.19)$$

and then using the trigonometric identity $\sin^2(\frac{k\Delta x}{2}) = \frac{1-\cos(k\Delta x)}{2}$, Eqn. (3.19) becomes:

$$e^{At} = 1 - \frac{4A^2\Delta t}{(\Delta x)^2}\sin^2\left(\frac{k\Delta x}{2}\right) \quad (3.20)$$

An amplification factor G is the ratio of the error amplitudes at two consecutive time levels and is written as

$$G = \frac{\varepsilon_i^{N+1}}{\varepsilon_i^N} = \frac{e^{A(t+\Delta t)}e^{ikx}}{e^{At}e^{ikx}} = e^{A\Delta t} \quad (3.21)$$

and for the error to not grow in time

$$|G| \leq 1 \quad (3.22)$$

Therefore, Eqn. (3.20) becomes

$$\left|e^{At}\right| = \left|1 - \frac{4A^2\Delta t}{(\Delta x)^2}\sin^2\left(\frac{k\Delta x}{2}\right)\right| \leq 1 \tag{3.23}$$

Examining both possibilities

(i) Positive

$$1 - \frac{4A^2\Delta t}{(\Delta x)^2}\sin^2\left(\frac{k\Delta x}{2}\right) \leq 1$$

$$\Longrightarrow \frac{4A^2\Delta t}{(\Delta x)^2}\sin^2\left(\frac{k\Delta x}{2}\right) \geq 0 \quad \text{which is always true}$$

(i) Negative

$$-\left(1 - \frac{4A^2\Delta t}{(\Delta x)^2}\sin^2\left(\frac{k\Delta x}{2}\right)\right) \leq 1$$

$$\frac{4A^2\Delta t}{(\Delta x)^2}\sin^2\left(\frac{k\Delta x}{2}\right) - 1 \leq 1$$

$$\frac{4A^2\Delta t}{(\Delta x)^2}\sin^2\left(\frac{k\Delta x}{2}\right) \leq 2$$

$0 \leq sin^2\left(\frac{k\Delta x}{2}\right) \leq 1$ for all $\Re(\Delta x)$, therefore

$$\frac{A^2\Delta t}{(\Delta x)^2} \leq \frac{1}{2} \quad \Longrightarrow \quad \Delta t \leq \frac{(\Delta x)^2}{2C^2} \tag{3.24}$$

where A is calculated from Eqn. (2.33).

This is the equation used to calculate a time step size for the thickness generator to maintain stability. The solution of the thickness equation will be a steady one, therefore to ensure quickest convergence a local timestep can be calculated every iteration of the scheme. Within a single iteration, this method calculates a time step for each cell and advances the solution on a cell by cell basis.

3.3 Camberline Generator

For completeness, the description of the camberline generator as derived by Medd [Medd 1998] is included. Using a second order central finite difference on the camberline and thickness terms Eqn. (2.23) becomes

$$\frac{\partial f}{\partial t^*} = -\bar{u}\frac{(f_{i+1} - f_{i-1})}{\Delta x} - \frac{\Delta u}{4}\frac{(T_{i+1} - T_{i-1})}{\Delta x} + \bar{v} \tag{3.25}$$

This discretization along with the addition of a linear, second difference artificial dissipation term, reduces the method to a first order upwind scheme which keeps the camberline as smooth as possible.

Discretization of the velocity combinations is done in the following manner

$$\bar{u} = \frac{1}{2}\left(u_i^+ + u_i^-\right) \quad ; \quad \bar{v} = \frac{1}{2}\left(v_i^+ + v_i^-\right)$$
$$\Delta u = \left(u_i^+ - u_i^-\right) \quad ; \quad \Delta v = \left(v_i^+ - v_i^-\right)$$

and the surface velocities used in the velocity combinations

$$u_i^+ = \frac{1}{2}\left(u_{camb}^i + u_{i,j=2}\right) \quad ; \quad v_i^+ = \frac{1}{2}\left(v_{camb}^i + v_{i,j=2}\right)$$
$$u_i^- = \frac{1}{2}\left(u_{camb}^i + u_{i,j=MY}\right) \quad ; \quad v_i^- = \frac{1}{2}\left(v_{camb}^i + v_{i,j=MY}\right)$$
$$u_{camb}^i = \frac{1}{2}\left(u_{i,j=2} + u_{i,j=MY}\right) \quad ; \quad v_{camb}^i = \frac{1}{2}\left(v_{i,j=2} + v_{i,j=MY}\right)$$

The velocities $u_{i,j=2}$ and $u_{i,j=MY}$ refer to the cell-centered value in the cells adjacent to the upper and lower blade surfaces respectively.

3.4 Flow Field Integrator

3.4.1 Time Advancement

A multi-stage time advancement scheme based on the one proposed by Jameson et.al. [Jameson et.al. 1979] is used to converge the solution of the Euler equations to steady state. The method is an explicit scheme meaning the solution is known at the current time level N, and advances the solution by some time step Δt to the solution at the next time level, $N+1$. First defining the solution vector

$$\vec{W} = \left\{ \begin{array}{c} \forall \vec{w} \\ f \end{array} \right\} \tag{3.26}$$

Where $\forall$ is the cell volume, $\vec{w}$ is the conservative solution vector previously defined and f is the camberline. The camberline is included in the solution vector because it was chosen by Medd [Medd 1998] to be coupled with the multi-stage scheme for the flow equations. A four-stage scheme is used to converge the solution

$$\begin{aligned} \vec{W^{(0)}} &= \vec{W^N} \\ \vec{W^{(1)}} &= \vec{W^N} - \alpha_1 \Delta t \vec{R}(\vec{W^{(0)}}) \\ \vec{W^{(2)}} &= \vec{W^N} - \alpha_2 \Delta t \vec{R}(\vec{W^{(1)}}) \\ \vec{W^{(3)}} &= \vec{W^N} - \alpha_3 \Delta t \vec{R}(\vec{W^{(2)}}) \\ \vec{W^{(4)}} &= \vec{W^N} - \alpha_4 \Delta t \vec{R}(\vec{W^{(3)}}) \\ \vec{W^{N+1}} &= \vec{W^4} \end{aligned} \tag{3.27}$$

The stage coefficients are chosen for convergence acceleration but because the explicit method is used only for convergence purposes the coefficients need not be chosen for time accuracy. The values used are $\alpha(1) = \frac{1}{4}$, $\alpha(2) = \frac{1}{3}$, $\alpha(3) = \frac{1}{2}$ and $\alpha(4) = 1$. The residual, $\vec{R}$ is defined as the following

$$\vec{R} = \begin{pmatrix} \forall \frac{\partial \vec{w}}{\partial t} \\ \frac{\partial f}{\partial t} \end{pmatrix} = \begin{pmatrix} -\oint (E\vec{n}_x + F\vec{n}_y) \\ -\bar{u}\frac{\partial f}{\partial x} - \frac{\Delta u}{4}\frac{\partial T}{\partial x} + \bar{v} \end{pmatrix} \tag{3.28}$$

3.4.2 Spacial Discretization

The spatial discretization used for the flow equations and the geometry equations is the finite volume scheme. In using this scheme the entire domain is divided up into small control volumes where the solutions to flow equations exist. Both the volume integral and the surface integral of Eqn. (2.65) contain spatial derivatives which require attention. Consider the following quadrilateral control volume, (i,j)

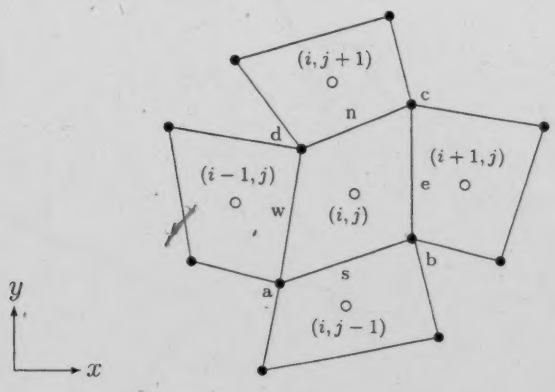

Figure 3.1: Control Volume

Where the indices i and j indicate the cell centers, n, e, s, w are the cell faces of the (i, j) cell and a, b, c, d are the vertices. The mean value theorem is used to approximate the values of the solution at the cell centers. Since the variable is approximated to have no spatial variation within the cell, the volume integral of Eqn. (2.65) becomes

$$\int_{\forall} \frac{\partial \vec{w}}{\partial t} d\forall \approx \frac{\partial \vec{w}}{\partial t} \Delta\forall \tag{3.29}$$

Where $\forall$ is the volume of the cell with unit depth and is found as follows

$$\Delta\forall = \frac{1}{2} |\Delta x_{ac} \Delta y_{bd} - \Delta x_{bd} \Delta y_{ac}| \tag{3.30}$$

Now consider the following control volume surface element s from Fig. (3.1)

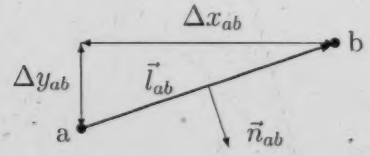

Figure 3.2: Control Volume Surface

Where

$$\Delta x_{ab} = x_b - x_a$$

$$\Delta y_{ab} = y_b - y_a$$

and $\vec{l}_{ab}$ is the vector describing the control volume surface s from a to b, defined as

$$\vec{l}_{ab} = (\Delta x_{ab})\vec{e}_x + (\Delta y_{ab})\vec{e}_y$$

By satisfying the conditions $\vec{n}_{ab} \cdot \vec{l}_{ab} = 0$ and $|\vec{n}_{ab}| = |\vec{l}_{ab}|$, the outward normal vector $\vec{n}_{ab}$ can be shown to be

$$\vec{n}_{ab} = (\Delta y_{ab})\vec{e}_x + (-\Delta x_{ab})\vec{e}_y$$

The values of E and F are now required on each face of the cell in order to evaluate the surface integral. There are two approximations made to obtain these surface fluxes. First the mean value theorem is used to approximate the variation of the fluxes along the faces, as the average at the center of the face. Second, since only the cell-centered values are known, the mean value on the face must be approximated by an interpolation scheme using the cell-centered values in the neighbouring cells.

This approximation states that the face values are constant along the length of the face and the integral can be written as

$$\oint_S (E\vec{n}_x + F\vec{n}_y)\, dS \approx \sum_{k=1}^{K} (E_k \Delta y_k - F_k \Delta x_k) \tag{3.31}$$

with K being the number of faces on the cell.

For a quadrilateral element

$$\begin{aligned} \sum_{face}^{4} (E_k \Delta y_k - F_k \Delta x_k) &= (E_s \Delta y_s - F_s \Delta x_s) \\ &+ (E_e \Delta y_e - F_e \Delta x_e) \\ &+ (E_n \Delta y_n - F_n \Delta x_n) \\ &+ (E_w \Delta y_w - F_w \Delta x_w) \end{aligned} \tag{3.32}$$

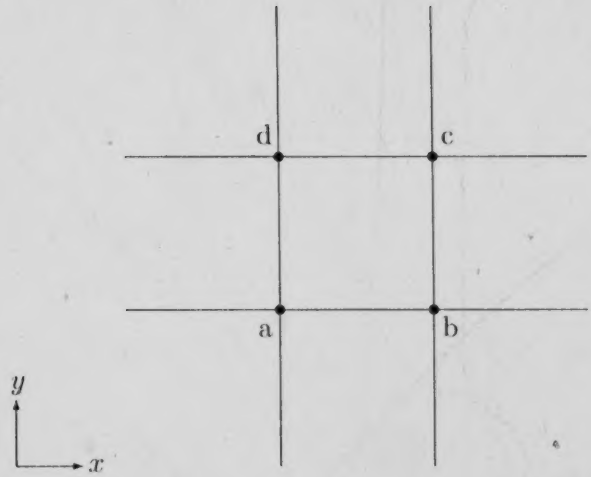

Figure 3.3: Uniform Square Grid

Using a linear interpolation of the cell-centered solutions to approximate the face-centered values

$$E_e = E_{i+\frac{1}{2},j} = \frac{1}{2}\left(E_{i+1,j} + E_{i,j}\right) \tag{3.33}$$

$$F_e = F_{i+\frac{1}{2},j} = \frac{1}{2}\left(F_{i+1,j} + F_{i,j}\right) \tag{3.34}$$

for the east face of the cell and similarly for the remaining faces.

Applying Eqn. (3.33) to the uniform square grid of Fig. (3.3), the finite volume discretization can be reduced to

$$\vec{R} = \frac{(E_e - E_w)\Delta y}{\Delta x \Delta y} + \frac{(F_e - F_w)\Delta x}{\Delta x \Delta y} \tag{3.35}$$

since,

$$\Delta x = x_b - x_a = -(x_d - x_c) \tag{3.36}$$

$$\Delta y = y_c - y_b = -(y_a - y_d) \tag{3.37}$$

Substitution of Eqns. (3.33) and (3.34) into Eqn. (3.38) reduces the equation to the following central finite difference approximation

$$\vec{R} = \frac{E_{i+1,j} - E_{i-1,j}}{2\Delta x} + \frac{F_{i,j+1} - F_{i,j-1}}{2\Delta y} \tag{3.38}$$

Substitution of the following Taylor series expansion for $E_{i+1,j}$ and $E_{i-1,j}$

$$E_{i+1,j} = E_{i,j} + \frac{\Delta x}{1!}\frac{\partial E}{\partial x} + \frac{\Delta x^2}{2!}\frac{\partial^2 E}{\partial x^2} + \frac{\Delta x^3}{3!}\frac{\partial^3 E}{\partial x^3} \tag{3.39}$$

$$E_{i-1,j} = E_{i,j} - \frac{\Delta x}{1!}\frac{\partial E}{\partial x} + \frac{\Delta x^2}{2!}\frac{\partial^2 E}{\partial x^2} - \frac{\Delta x^3}{3!}\frac{\partial^3 E}{\partial x^3} \tag{3.40}$$

and similar equations for $F_{i+1,j}$ and $F_{i-1,j}$ into Eqn. (3.38) gives the residual of the exact equation plus the truncated terms

$$\vec{R} = \frac{\partial E}{\partial x} + \frac{\partial F}{\partial y} + \frac{\Delta x^3}{3!}\frac{\partial^3 E}{\partial x^3} + \frac{\Delta y^3}{3!}\frac{\partial^3 F}{\partial y^3} \tag{3.41}$$

The leading truncation terms are shown and are of order $0(\Delta x^2, \Delta y^2)$. Therefore, the finite volume discretization reduces to a central finite difference approximation on a uniform square grid, which gives second order accuracy.

3.4.3 Artificial Dissipation

Since the finite volume scheme can be reduced to central differences on a uniform grid, the addition of artificial dissipation is required to prevent odd-even decoupling and shock overshoots. To maintain the conservative form of the equations, the dissipation is added following the method of Jameson et.al. [Jameson et.al. 1979]

$$\int_{\forall} \frac{\partial \vec{w}}{\partial t} + \oint_S \left(\overline{\overline{Q}} \vec{w} + \overline{\overline{D}} \vec{w} \right) = 0 \tag{3.42}$$

Where $\overline{\overline{Q}}$ is the spatial operator of the original equation and $\overline{\overline{D}} = d_\xi + d_\eta$ is the artificial dissipation. A combination of non-linear second and fourth differences are added in the grid directions (ξ, η) and are used as follows

$$d_\xi = \left(\epsilon_\xi^{(2)} |\lambda_\xi|_{max} \Delta\xi \frac{\partial \vec{w}}{\partial \xi} - \epsilon_\xi^{(4)} |\lambda_\xi|_{max} \Delta\xi^3 \frac{\partial^3 \vec{w}}{\partial \xi^3} \right) \tag{3.43}$$

$$d_\eta = \left(\epsilon_\eta^{(2)} |\lambda_\eta|_{max} \Delta\eta \frac{\partial \vec{w}}{\partial \eta} - \epsilon_\eta^{(4)} |\lambda_\eta|_{max} \Delta\eta^3 \frac{\partial^3 \vec{w}}{\partial \eta^3} \right) \tag{3.44}$$

Where $|\lambda|_max$ is taken to be the maximum eigenvalue of the Euler equations in that cell

$$|\lambda_\xi|_{max} = |V_\xi| + |a_1|, |\lambda_\eta|_max = |V_\eta| + |a_2| \tag{3.45}$$

The velocities V_ξ and V_η are the velocities normal to the cell faces and a_1 and a_2 are the local speed of sound on the faces. The terms $\epsilon_\xi^{(2)}$ and $\epsilon_\xi^{(4)}$ are defined as

$$\left(\epsilon_\xi^{(2)} \right)_{i+\frac{1}{2},j} = \kappa^{(2)} max[(\nu_\xi)_{i,j}\ ,\ (\nu_\xi)_{i+1,j}] \tag{3.46}$$

$$\left(\epsilon_\xi^{(4)} \right)_{i+\frac{1}{2},j} = max\left[0\ ,\ \kappa^{(4)} - \left(\epsilon_\xi^{(2)} \right)_{i+\frac{1}{2},j} \right] \tag{3.47}$$

and they are used to add the second difference term near shocks to prevent overshoots and remove the fourth difference term that can be destabilizing in that region. A value of $\kappa^{(2)} = 2.0$ was found to keep the solution smooth

while a value of $\kappa^{(4)} = \frac{1}{12}$ was found to capture discontinuous regions without smearing.

The shocked region is found using the following switching function ν_ξ

$$(\nu_\xi)_{i,j} = \frac{|P_{i+1,j} - 2P_{i,j} + P_{i-1,j}|}{|P_{i+1,j}| + |2P_{i,j}| + |P_{i-1,j}|} \tag{3.48}$$

which is based on the local pressure gradient.

In the region of low pressure gradient, only the fourth difference is used to prevent odd-even decoupling which will maintain the second order accuracy of the finite volume scheme. In a region of high pressure gradient the fourth difference is turned off and only the second difference term is used to capture the shock.

3.4.4 Numerical Stability and Time Step

The pseudo-time stepping scheme used to converge the flow equations to steady state is an explicit one. A four stage Runge-Kutta explicit multistep technique was implemented to drive the solution of the flow equations to convergence. Therefore, stability and time step size must be considered.

This work is an extension Medd [Medd 1998] and the same two dimensional flow field integrator is used. The Von Neumann stability analysis performed by Medd on the following linear, constant coefficient model equation

$$\frac{\partial u}{\partial t} + \bar{\bar{c}}\frac{\partial u}{\partial x} = k\Delta x^3 \frac{\partial^4 u}{\partial x^4} \tag{3.49}$$

was deemed again to be sufficient to choose a time step size for the time advancement of the flow equations. Upon deriving the equation for the growth

factor of an explicit four stage Runge-Kutta time integrator, Medd graphically found the limiting Courant number, defined as $Cn = \bar{\bar{c}}\frac{\Delta t}{\Delta x}$, where $\bar{\bar{c}}$ is the local wave speed, which satisfied stability and maximized the rate of convergence. A $Cn = 2.0$ was chosen but due to the inclusion of the new technique for the thickness design, the author chose a $Cn = 1.0$ to ensure stability for any design procedure.

3.5 Boundary Conditions for Flow Equations

3.5.1 Inflow and Outflow Boundaries

The method used to specify the inlet and outlet boundary conditions is based on the method of characteristics. The signs of the eigenvalues from Eqn. (2.68) determine whether the information propagates in to or out of the computational domain. If the sign is positive, information travels left to right, the direction of the flow, and travels in the opposite direction if the sign is negative. Two possibilities exist for each of the boundary conditions.

Subsonic Inflow

For a subsonic inflow condition, three of the eigenvalues are positive so three physical conditions must be specified upstream of the domain. The physical conditions chosen are the stagnation pressure P_o, the stagnation temperature Θ_o and the inlet flow angle β. The fourth boundary condition is obtained using a second order extrapolation to obtain the static pressure P. the primitive variables ρ, u, v, e_t can now be found using the isentropic relations as well as the definition of the Mach number

$$\frac{P_o}{P} = \left(1 + \frac{\gamma - 1}{2} M^2\right)^{\frac{\gamma}{\gamma-1}} \tag{3.50}$$

$$\frac{\Theta_o}{\Theta} = 1 + \frac{\gamma - 1}{2} M^2 \tag{3.51}$$

$$M = \frac{|V|}{\sqrt{\gamma R \Theta}} \tag{3.52}$$

and the following geometric relations using the specified flow angle

$$u = \frac{|V|}{\sqrt{1 + tan^2\beta}} \qquad v = u\, tan\beta$$

By using the perfect gas law and the equation of state, the remaining primitive variables can be calculated as follows

$$\begin{aligned} \rho &= \frac{P}{\Theta} \\ e_t &= \frac{P}{\gamma - 1} + \frac{1}{2}\rho\left(u^2 + v^2\right) \end{aligned}$$

Once these variables have been found the conservative variables of Eqn. (2.65) are easily calculated.

Supersonic Inflow

For supersonic inflow, all of the eigenvalues are positive which means that four physical conditions must be specified. In addition to P_o, Θ_o and β the inlet Mach number M is chosen as the fourth condition. The above equations can then be rearranged to give the flow variables on the inflow boundary.

Subsonic Outflow

With the subsonic outflow boundary only one physical condition and three extrapolated quantities are required. The physical condition chosen is the back pressure P_{back} and ρ, u and v are obtained from inside the domain using a second order accurate extrapolation. The one remaining variable e_t, can be calculated using the equation of state.

Supersonic Outflow

Since all the eigenvalues are positive with supersonic flow, all the variables are extrapolated using a second order accurate method from the interior of the domain to the outflow boundary.

3.5.2 Periodic Boundary

The calculation of an entire row of blades can be done by calculating the flow through two of the blades while enforcing periodicity in the region upstream and downstream of the blade since the flow in the passages above and below are also the flow through the identical blades. The solution along the bottom edge of the domain is put into the boundary above the top edge. Similarly, the solution along the top of the domain is used as the boundary value on the bottom

3.5.3 Blade Surfaces

Analysis Mode

In a conventional calculation, where the solution around a fixed geometry is required, the boundary condition enforced on the solid surfaces is the no-flux condition. This can be stated as

$$\vec{V} \cdot \vec{n} = 0 \tag{3.53}$$

where $\vec{V}$ is the velocity on the surface of the blade and $\vec{n}$ is the unit vector normal to the surface. Thus, pressure is the only value that is required on the surface of the blade. All other surface flux values are set to zero to enforce the no-flux boundary condition and pressure is obtained from the equation of state using a zeroth order extrapolation of the primitive variables from the adjacent cell center.

Inverse Mode

For the inverse problem, the blade is required to produce a specified amount of power. Flow turning can be related to power through the Euler Turbine Equation [Laksh. 1996]. Reiterating Eqn. (2.2),

$$\dot{W} = \dot{m}\omega r \Delta \bar{v}_y = \dot{m} \Delta h_o$$

An equation is now needed to impose the flow turing condition on the blade. Following the analysis of Dang [Dang 1995] and Dang and Isgro [Dang & Isgro 1995] the y-component of the momentum equation of Eqn.

(2.59) can be integrated in the pitchwise direction to give the relation between the blade pressure loading and the mass averaged tangential velocity, $\bar{v}_y$. Integrating from the upper blade surface (+) through the passage to the lower surface (−)

$$\int_{+}^{-} \rho \frac{Dv}{Dt} dy = -\int_{+}^{-} \frac{\partial P}{\partial y} dy \tag{3.54}$$

the equation becomes a pressure difference, or jump, across the blade

$$(P^{+} - P^{-}) = \Delta P = \int_{+}^{-} \rho \frac{Dv}{Dt} dy \tag{3.55}$$

Restating the mass flux averaged tangential velocity, $\bar{v}_y$

$$\bar{v}_y(x) = \frac{\int_{+}^{-} \rho u v dy}{\dot{m}} \tag{3.56}$$

and differentiating with respect to x, assuming $\dot{m}$ is constant

$$\dot{m} \frac{d\bar{v}_y}{dx} = \frac{\partial}{\partial x} \int_{+}^{-} \rho u v dy \tag{3.57}$$

Then using Leibnitz's theorem on the right hand side of the equation

$$\dot{m} \frac{d\bar{v}_y}{dx} = \int_{+}^{-} \frac{\partial}{\partial x}(\rho u v) dy + \left[(\rho u v)^{-}\right] \frac{dy^{-}}{dx} - \left[(\rho u v)^{+}\right] \frac{dy^{+}}{dx} \tag{3.58}$$

and expanding using the product rule, the equation becomes

$$\dot{m} \frac{d\bar{v}_y}{dx} = \int_{+}^{-} \left[\rho u \frac{\partial v}{\partial x} + v \frac{\partial}{\partial x}(\rho u)\right] dy + \rho u v \frac{dy^{-}}{dx} - \rho u v \frac{dy^{+}}{dx} \tag{3.59}$$

By adding and subtracting $\rho\frac{\partial v}{\partial t}$ and $\rho v\frac{\partial v}{\partial y}$ and using continuity, Eqn. (2.58)

$$\dot{m}\frac{d\bar{v}_y}{dx} = \int_+^- \left\{\rho\left[\frac{\partial v}{\partial t} + u\frac{\partial v}{\partial x} + v\frac{\partial v}{\partial y}\right] - \rho\frac{\partial v}{\partial t} - \rho v\frac{\partial v}{\partial y} + v\left[-\frac{\partial \rho}{\partial t} - \frac{\partial}{\partial y}(\rho v)\right]\right\} + \left[(\rho uv)^-\right]\frac{dy^-}{dx} - \left[(\rho uv)^+\right]\frac{dy^+}{dx} \tag{3.60}$$

then collecting terms

$$\dot{m}\frac{d\bar{v}_y}{dx} = \int_+^- \left[\rho\frac{Dv}{Dt}dy - \frac{\partial}{\partial t}(\rho v) - \frac{\partial}{\partial y}(\rho v^2)\right]dy - \left[(\rho uv)^-\right]\frac{dy^-}{dx} - \left[(\rho uv)^+\right]\frac{dy^+}{dx} \tag{3.61}$$

and expanding the derivatives

$$\dot{m}\frac{d\bar{v}_y}{dx} = \int_+^- \rho\frac{Dv}{Dt}dy - \int_+^- \frac{\partial}{\partial t}(\rho v)dy - (\rho v^2)^- + (\rho v^2)^+ + \left[(\rho uv)^-\right]\frac{dy^-}{dx} - \left[(\rho uv)^+\right]\frac{dy^+}{dx} \tag{3.62}$$

The derivatives $\frac{dy^+}{dx}$ and $\frac{dy^-}{dx}$ can be obtained by taking the derivative of the equations of the blade surfaces with respect to x

$$\frac{dy^+}{dx} = \frac{\partial}{\partial x}\left(f + \frac{T}{2}\right) \quad ; \quad \frac{dy^-}{dx} = \frac{\partial}{\partial x}\left(f - \frac{T}{2}\right) \tag{3.63}$$

Substituting these equations into the equations for the upper and lower blade surfaces, Eqns. (2.21) and (2.22) and rearranging gives

$$\frac{dy^+}{dx} = \frac{u^+}{v^+} \quad ; \quad \frac{dy^-}{dx} = \frac{u^-}{v^-} \tag{3.64}$$

Substitution of these equations into Eqn. (3.62) and assuming steady state, yields

$$\dot{m}\frac{d\bar{v}_y}{dx} = \int_+^- \rho \frac{Dv}{Dt} dy \tag{3.65}$$

By substituting this equation into Eqn. (3.55) becomes the final form of the blade pressure loading, Eqn. (2.3)

$$\Delta P = \dot{m}\frac{d\bar{v}_y}{dx}$$

This equation is then used on the boundary of the blade to impose the pressure jump condition. Using a first order Taylor series expansion, the pressure on the upper and lower surfaces can be obtained

$$P^+ = P_{camb} + \frac{\Delta P}{2} \tag{3.66}$$

$$P^- = P_{camb} - \frac{\Delta P}{2} \tag{3.67}$$

where

$$P_{camb} = \frac{1}{2}\left(P_{i,j=2} + P_{i,j=MY}\right)$$

The objective of this inverse design method is to design a blade that produces a specified amount of flow turning $\Delta\bar{v}_y$ that follows the shape of

the input turning distribution. These values are required input from the designer. The total turning $\Delta\bar{v}_y$ is chosen from the work requirement of that row of blades and the shape of the distribution is chosen based primarily on designer experience. One family of turning shapes used by Dang [Dang 1995] and Medd [Medd 1998] are

$$\frac{d\bar{v}_y}{dx} = Kx^m (1-x)^n \tag{3.68}$$

With this, the Kutta condition is satisfied at both the leading and trailing edges and m and n are used to adjust the general shape of the curve as well as moving the location of the maximum value. The constant K is defined as

$$K = \frac{\Delta\bar{v}_y}{\int_{le}^{te} x^m (1-x)^n \, dx} \tag{3.69}$$

where

$$\Delta\bar{v}_y = \int_{le}^{te} \frac{d\bar{v}_y}{dx} dx$$

The value of $\frac{d\bar{v}_y}{dx}$ must be adaptive to the flow field such that, the total turning requirement is satisfied. This is done by generating the average tangential velocity distribution $\bar{v}_y(x)$ in the bladed region

$$\bar{v}_y(x) = \bar{v}_y(le) + \int_{le}^{x} \frac{d\bar{v}_y}{dx} dx \tag{3.70}$$

This equation states that the average tangential velocity starts at $\bar{v}_y(le)$ at the leading edge, which is obtained from the solution of the flow field, and

is incremented along the axial chord of the blade by the partial area under the curve until the trailing edge value is obtained, which is $\bar{v}_y(te) = \bar{v}_y(le) + \Delta\bar{v}_y$.

The turning distribution that satisfies both the total turning and the turning shape can then be obtained by differentiating $\bar{v}_y(x)$ with respect to x

$$\frac{d\bar{v}_y}{dx} = \frac{d}{dx}(\bar{v}_y)$$

It is this equation that is used in Eqn. (2.3) to generate the blade pressure boundary condition.

For the inverse method, the blade surface is permeable during the iteration process. The blade geometry is updated by aligning it with the flow during the transient time marching process. Since the blade is permeable, all of the primitive variables must be given as boundary conditions on the blade surface. The first variable is the pressure which enforces the turning requirement. The second variable is the y-component of velocity v, which this can be calculated using a combination of the no-flux equations, Eqns. (2.21) and (2.22). Subtracting these two equations to produce

$$\Delta v = v^+ - v^- = \Delta u \frac{\partial f}{\partial x} + \bar{u}\frac{\partial T}{\partial x} \tag{3.71}$$

this can be used to construct the v velocity on the upper and lower blade surfaces using a first order Taylor series expansion as follow

$$\begin{aligned} v^+ &= v_{camb} + \frac{\Delta v}{2} \\ v^- &= v_{camb} - \frac{\Delta v}{2} \end{aligned}$$

where

$$v_{camb} = \frac{1}{2}\left(v_{i,j=2} + v_{i,j=MY}\right)$$

This velocity jump condition is similar to the treatment for the pressure jump condition. The third value is obtained from interpolation of the u velocity as follows

$$\begin{aligned} u^{+} &= \frac{1}{2}\left(u_{i,j=2} + u_{camb}\right) \\ u^{-} &= \frac{1}{2}\left(u_{i,j=MY} + u_{camb}\right) \end{aligned}$$

where

$$u_{camb} = \frac{1}{2}\left(u_{i,j=2} + u_{i,j=MY}\right)$$

The fourth and final boundary condition comes from a zeroth order extrapolation of density, ρ, from the adjacent cell center value. To find the last primitive variable, the equation of state is used to calculate e_t on both the upper and lower blade surfaces. With all of these values defined, all of the boundary conditions are specified for the inverse problem.

Chapter 4

Design Procedure and Results

When including the design of the thickness into the inverse design technique the hyperbolic nature of the camberline equation overrides the influence of the thickness. By allowing both the camberline and thickness to evolve simultaneously with the solution of the flow equations, the influence of the camberline dominates over the influence of the thickness. In the design cases where the design of the thickness is included an appropriate procedure was found and shown to allow the thickness to influence the final design. Along with a detailed description of the design procedure and intermediate results, the benefits of the final results compared to results from an existing design method are shown.

The effect of including the design of the thickness along with the camberline is shown to prove that without the effect of thickness, the design of the entire blade may not yield a practical solution. Five different test cases are presented: three in subsonic flow and two in transonic flow. The first subsonic test case reiterates a previous test case of Medd's [Medd 1998] and is included to show that given smooth prescribed turning and thick-

ness distributions, a camberline can be designed. It also proves that when the camberline generator has converged, the blade surfaces generated will be aligned with the flow, i.e. no mass flux crossing the surfaces. This is important because the camberline generator will be used in the full design procedure.

The second subsonic test case illustrates that design of the camberline alone is not enough to ensure the final blade will be acceptable. Small oscillations are introduced into the prescribed thickness to cause oscillations in the surface pressures. It is these pressure oscillations which may cause separation in a real flow. From this test case it is evident that design of the camberline alone is insufficient.

The final subsonic test case now employs the new design procedure. The steps taken in the design procedure are included to show how design of the thickness can remediate the pressure oscillations and the design of the camberline is used to enforce the no-flux conditions on the blade surfaces.

The first transonic test case again reiterates a previous test case of Medd's [Medd 1998]. Consideration of only the camberline again generates a blade with limited application. The prescribed thickness was too thick and caused a strong passage shock. The camberline developed a discontinuity to account for the discontinuous nature of the shock. Therefore, the final blade surfaces contain discontinuities and it is again evident in the pressure distributions that separation would occur in a real flow.

The second and final transonic test considers thickness design using the new design procedure. This test cases clearly illustrates design of thickness along the camberline is needed to generate a smooth blade. The resulting

blade generated no shocks in the passage therefore eliminating the large oscillations in the pressure. By fixing these pressure oscillations the possibility of the flow separating was greatly reduced.

All of the design calculations were performed on sheared H-type meshes, Fig. (4.1), with a numerical domain consisting of 192 X 32 cells and 128 cells in the bladed region. The domain was extended one chord upstream and downstream of the leading and trailing edges, respectively. Grid lines were clustered near the leading and trailing edges in the x-direction and near the blade surfaces in the y-direction. The pressure coefficient, C_P, used in the results is defined as $C_P = \frac{P}{P_o}$, where P is the local pressure and P_o is the stagnation pressure.

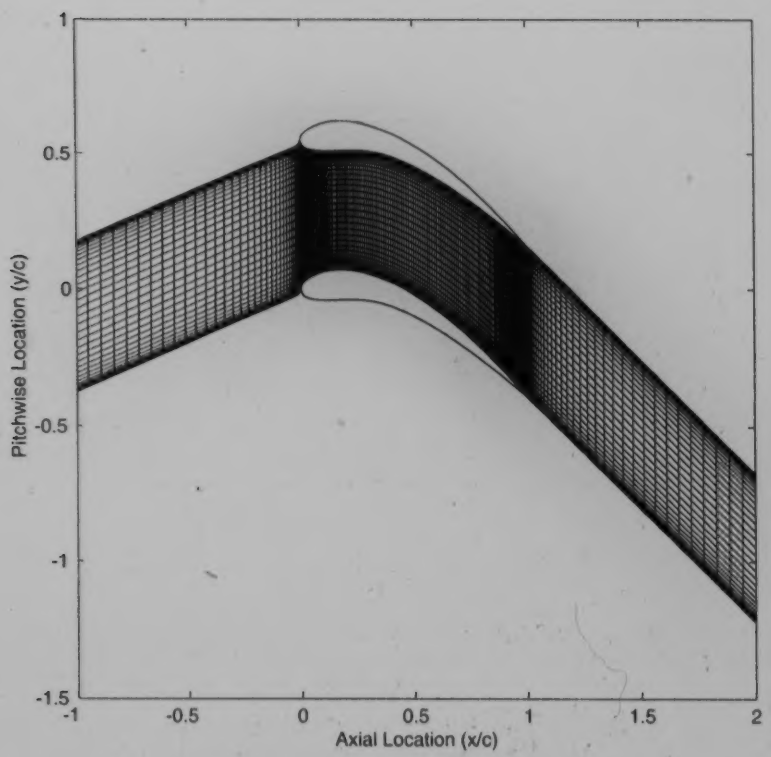

Figure 4.1: Typical Sheared H-type Mesh

4.1 Subsonic Test Cases

Turbomachinery operate in a wide variety of flow regimes. A very common one is the subsonic flow regime. An example would be turbines used to generate electricity. Therefore a series of test cases in the subsonic flow regime are presented. The first test case shows that given a smooth prescribed turning and thickness distributions, a camberline can be designed which generates smooth blade surfaces and enforces the no-flux condition. Then, when a smooth turning along with an oscillating thickness are prescribed, the camberline can not produce smooth blade surfaces. These unsmoothed surfaces yield undesirable aerodynamic characteristics. Finally, when using a design procedure where both the thickness and the camberline are designed, a blade with smooth surfaces can be generated even though an initially oscillatory thickness is prescribed. Thus showing that the problems with the previous test case are alleviated. Smooth blade surfaces are important because large changes in the curvature may cause separation in a real flow. Blade surface pressure distributions identify areas where this may be a problem.

The following subsonic test cases use different design procedures to produce a low Mach number turbine blade, and all use the same input parameters except the prescribed thicknesses and camberlines. The cascade is designed by specifying a back pressure of $P = 0.9P_o$, a spacing to chord ratio of $SC = 1$ and an inlet flow angle at $\beta = 0°$. The same smooth turning distribution is prescribed in all subsonic cases. It is generated from $\frac{d\bar{v}}{dx} = Kx^m(1-x)^n$ where $m = \frac{1}{4}$ and $n = \frac{7}{4}$ shown in Fig. (4.2), the scalar constant K is found from Eqn. (3.69) and the total turning specified as $\Delta\bar{v}_y = -0.25\sqrt{\gamma R\Theta_o}$.

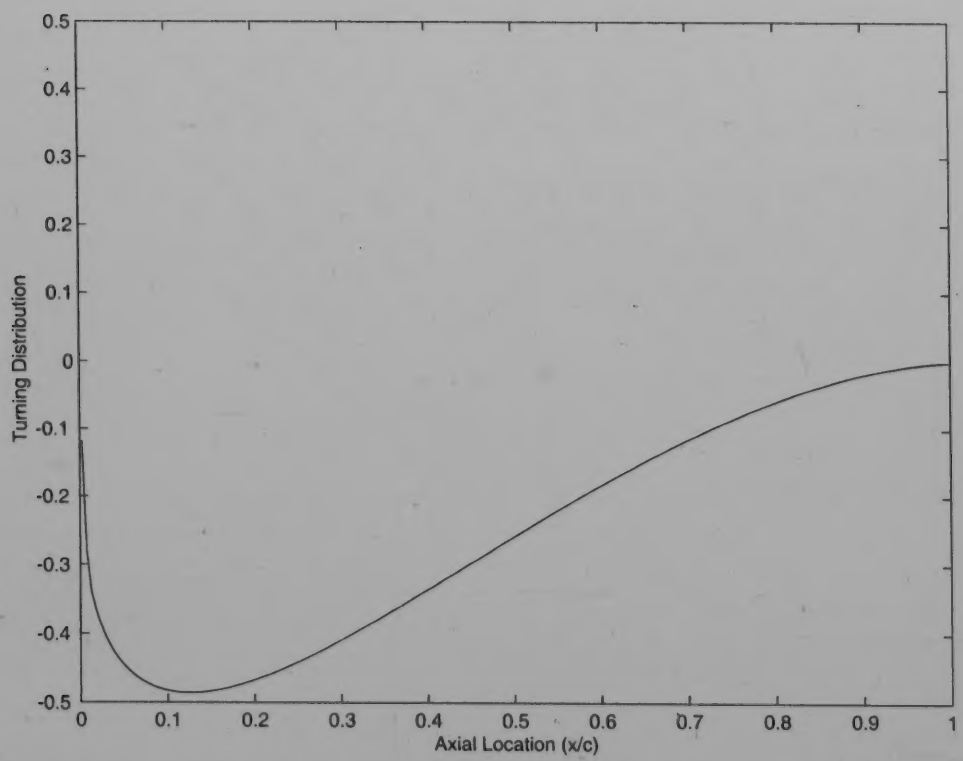

Figure 4.2: Prescribed Turning Distribution for Subsonic Cases

4.1.1 Subsonic Case 1: Camberline Generation - Smooth Prescribed Thickness

This test case is reiterated from Medd [Medd 1998] and is included to provide conclusive evidence that the camberline generator enforces the no-flux condition on the blade surfaces. A smooth thickness distribution of the form $T = kx^{\frac{1}{2}}(1-x)$ is prescribed, shown in Fig. (4.3), where the constant k is chosen to ensure a maximum thickness to spacing ratio of $\frac{T_{max}}{S} = 0.25$. This thickness distribution is arbitrarily chosen based on aesthetics. The initial camberline is guessed based on the inlet flow angle and the initial turning distribution.

The smooth prescribed turning and thickness distributions produce the converged blade shape shown in Fig. (4.4). The prescribed turning and thickness were smooth, therefore the camberline generated was also smooth, seen as the mid-line in Fig. (4.4). The combination of the smooth prescribed thickness and smooth generated camberline produces a blade with smooth surfaces. The converged flow in Fig. (4.5) show the smooth behavior of the flow through the passage.

The camberline generator is derived from the addition of Eqns. (2.21) and (2.22) therefore the no-flux condition is satisfied on each individual blade surface. In Figs. (4.6) and (4.7) the angle of the blade surfaces and flow are shown. If the the flow is parallel with the blade surfaces then there is no mass flux across the surfaces. The area that is of interest in these figures is in the bladed region, an axial location of 0 to 1. The flow angle closely follows the angle of the blade on both the suction and pressure blade surfaces. This further proves that the camberline generator possesses the ability to align

the flow with the blade surfaces at convergence.

As a consequence of the smooth blade surfaces, the blade pressure distributions, Figs. (4.8) and (4.9) were also smooth across the blade row. Again the area of importance in these figures is the bladed region, an axial location of 0 to 1. The smooth pressure distributions across the blade are to be expected, as the actual turning distribution matches the prescribed distribution. Fig. (4.10) clearly shows that the actual turning distribution matches the prescribed turning for the full length of the blade. Therefore, the global turning requirement and the local turning requirements were met.

The solution was converged to steady state when the the maximum residual reached machine zero, shown in Fig. (4.11).

Text resumes on page 92

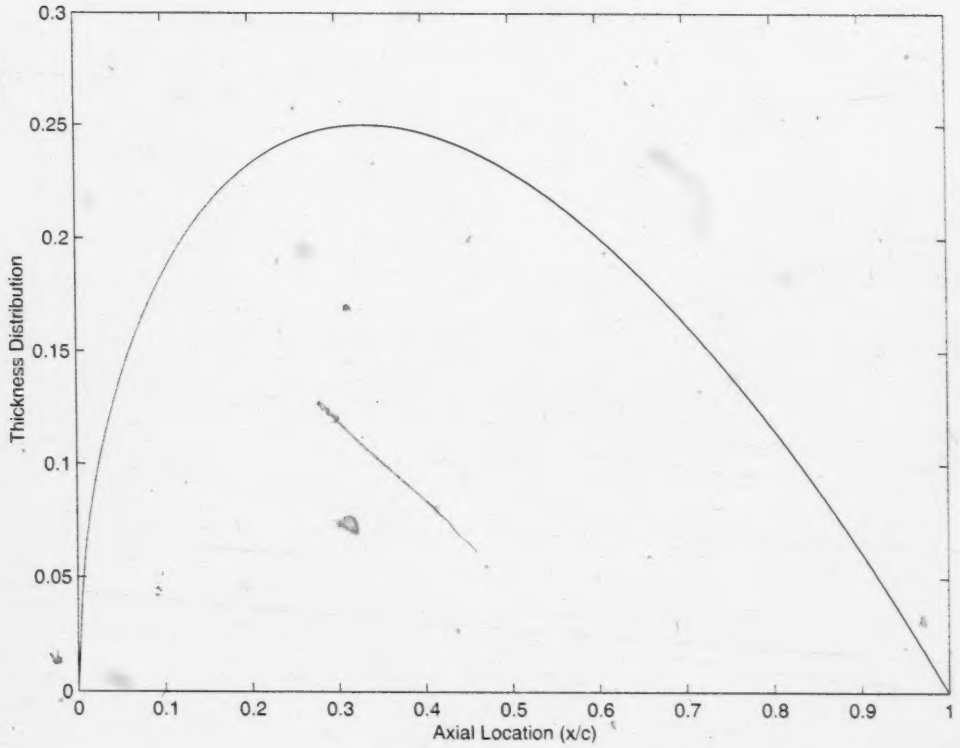

Figure 4.3: Subsonic Case 1: Prescribed Thickness Distribution

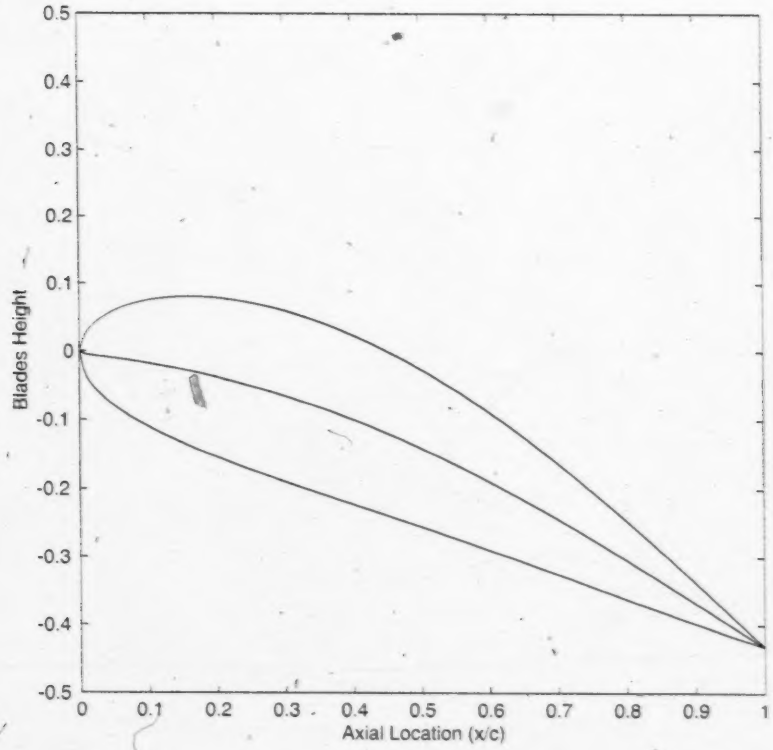

Figure 4.4: Subsonic Case 1: Converged Blade Shape

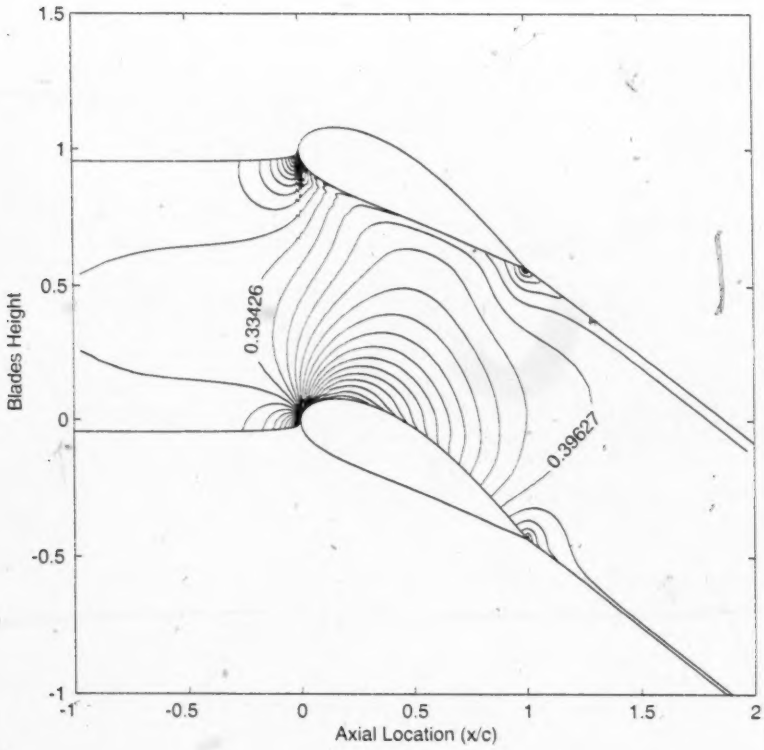

Figure 4.5: Subsonic Case 1: Contours of Mach Number in the Blade Passage

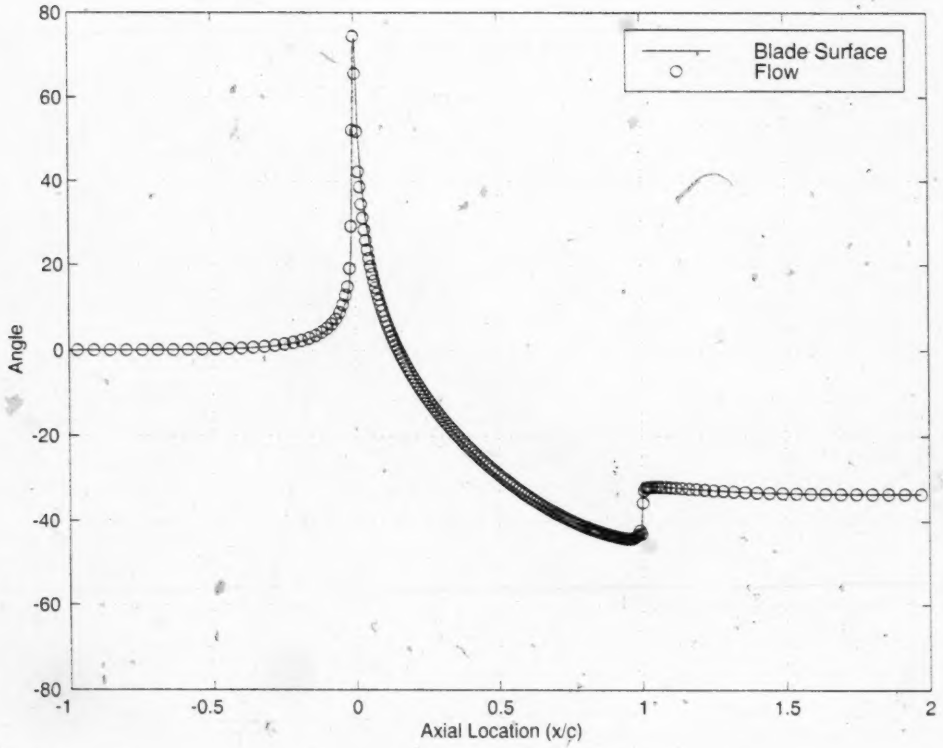

Figure 4.6: Subsonic Case 1: Blade and Velocity Angles - Suction Side

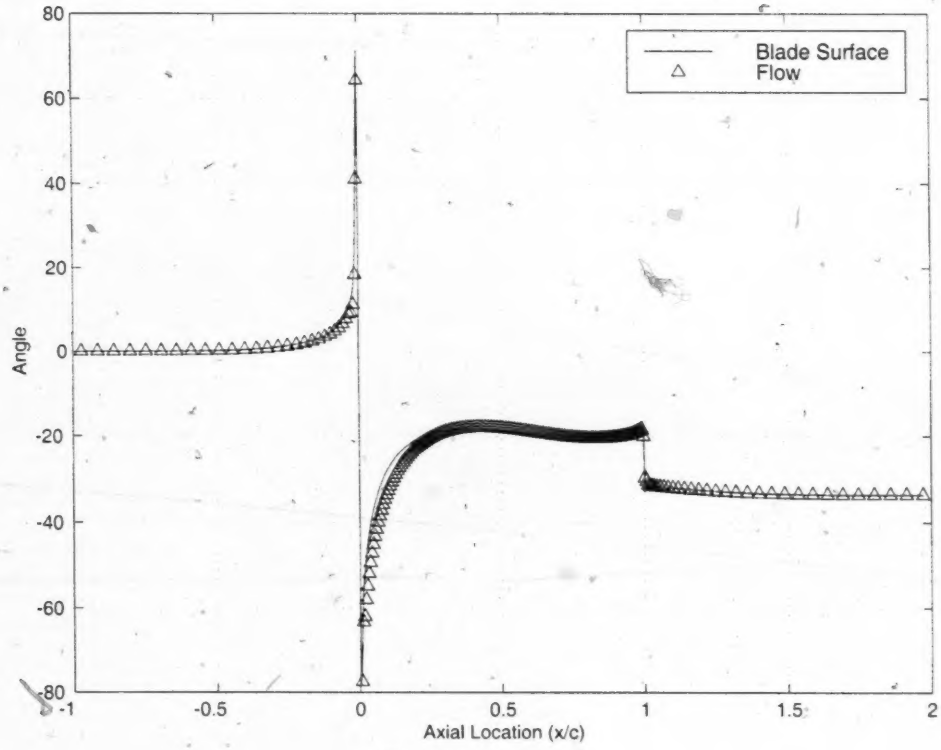

Figure 4.7: Subsonic Case 1: Blade and Velocity Angles - Pressure Side

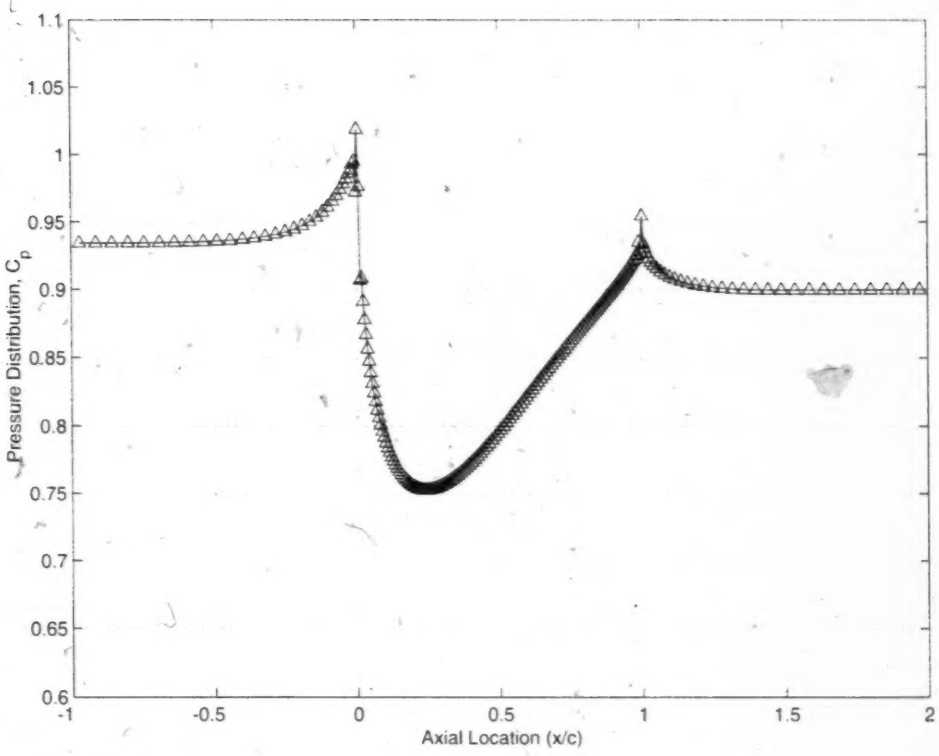

Figure 4.8: Subsonic Case 1: Pressure Distribution on Blade Surface - Suction Side

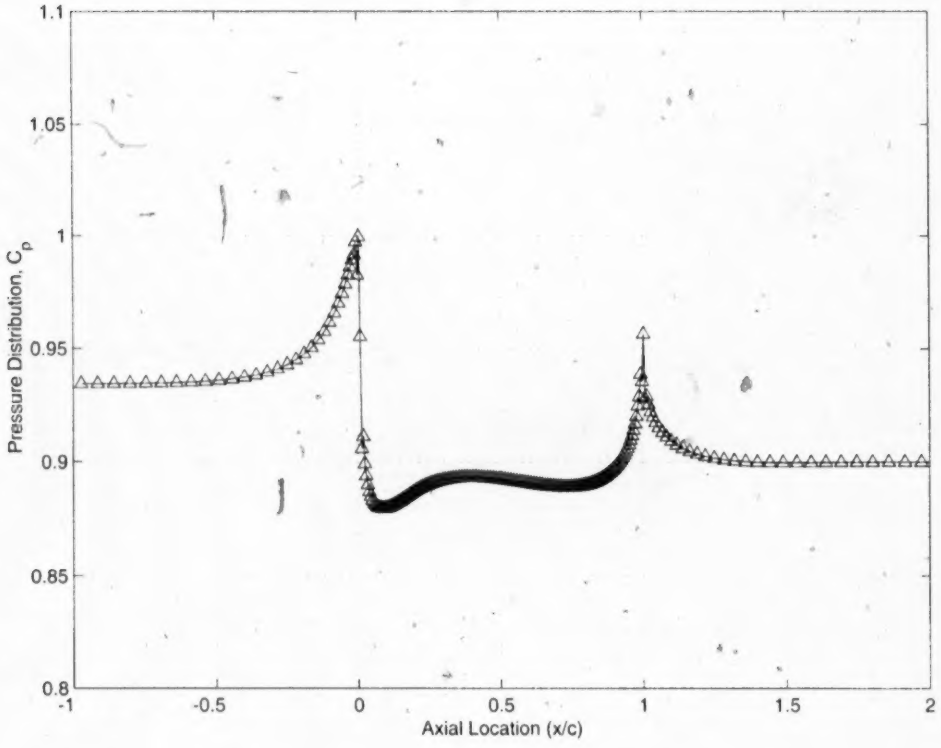

Figure 4.9: Subsonic Case 1: Pressure Distribution on Blade Surface - Pressure Side

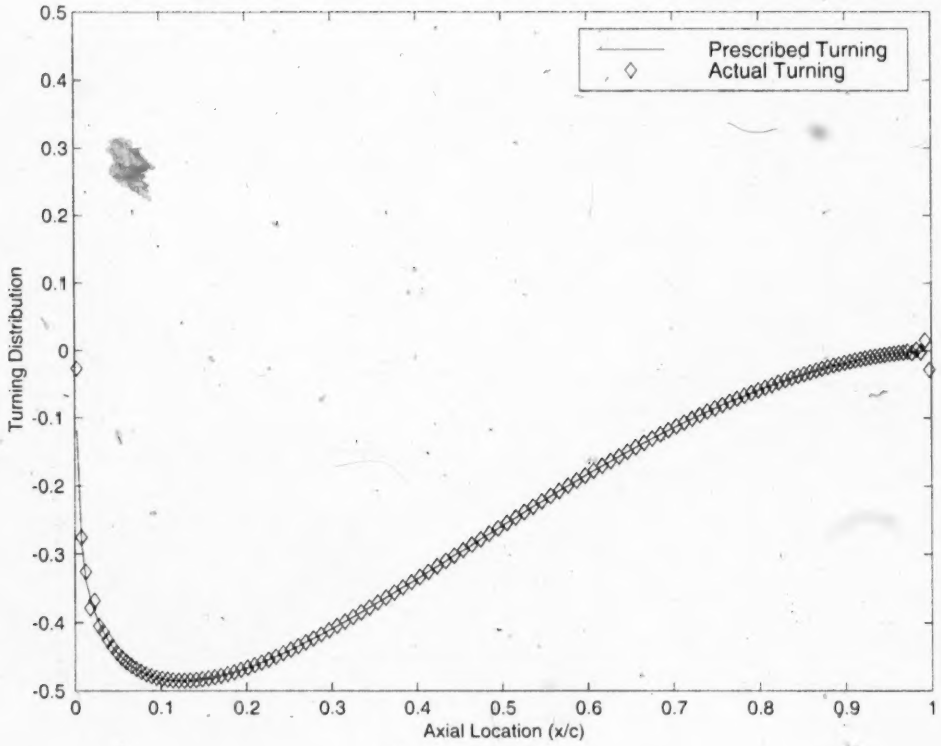

Figure 4.10: Subsonic Case 1: Turning Distributions in Blade Passage

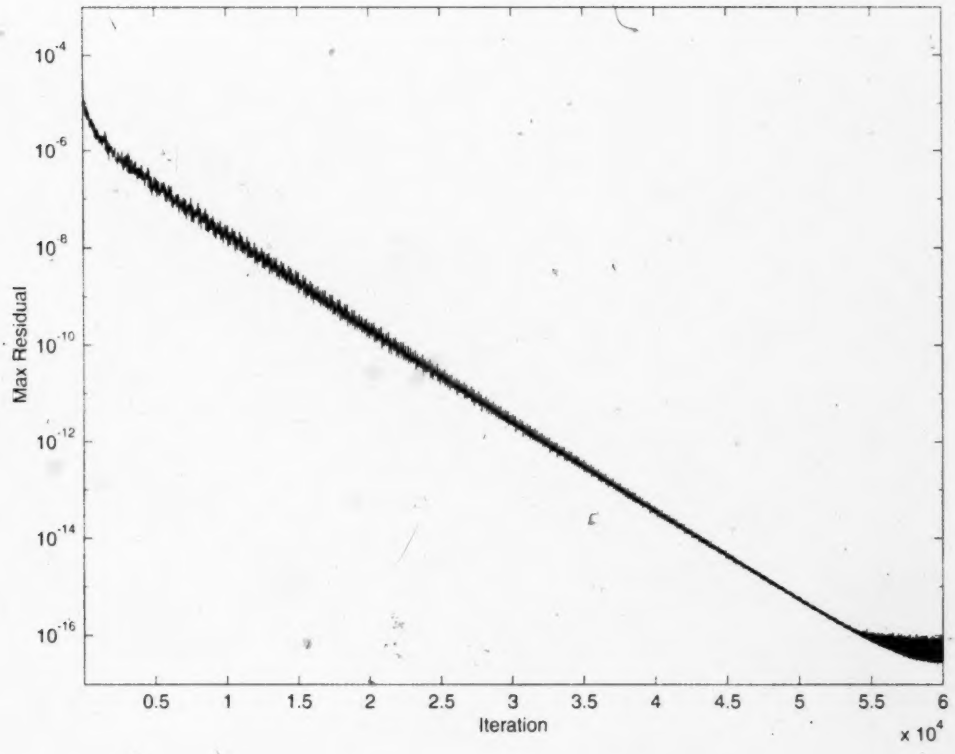

Figure 4.11: Subsonic Case 1: Convergence History

4.1.2 Subsonic Case 2: Camberline Generation - Oscillations in Prescribed Thickness

When the camberline equation converges the no-flux condition will be satisfied, however there still is no guarantee that camberline design will always produce a blade with acceptable characteristics. The following test case illustrates that the inverse design of camberline alone does not satisfy this condition.

The arbitrarily prescribed thickness distribution shown in Fig. (4.12) has oscillations added manually near axial positions of 0.6 and 0.7 of the chord with a maximum thickness to spacing ratio of $\frac{T_{max}}{S} = 0.25$. The purpose of these oscillations is to introduce oscillations in the blade surfaces. These blade surfaces will then cause large oscillations in the pressure distributions which could lead to separation in a real flow. The camberline does not have the ability to correct for these oscillations in the blade surfaces.

The oscillations in the blade surfaces from the thickness distribution is shown in the converged blade of Fig. (4.13). These oscillations in the blade surfaces clearly affect the flow through the blade passage as shown in Fig. (4.14). The flow has to adjust around the blade surface oscillations.

The resulting camberline, the mid-line in Fig. (4.13), tried to compensate for the oscillations in the blade surfaces by creating some small camberline oscillations. These camberline oscillations are not evident in Fig. (4.13) but upon inspection of a plot of the first derivative of the camberline $\frac{\partial f}{\partial x}$, Fig. (4.15), oscillations are clearly seen at approximately the same axial location as the thickness oscillations. Because of the manner in which the thickness is added to camberline, the camberline generator isn't successful in removing

these blade surface oscillations.

These blade surfaces oscillations may not affect the overall performance of the blade in an inviscid flow but would have drastic repercussions in a real flow. The oscillations in the blade surfaces cause large pressure oscillations shown Figs. (4.16) and (4.17). Another issue arises in that there is a conflict of competing influences between the smooth turning distribution and the pressure oscillations. The smooth turning distribution tries to enforce smooth pressures along the blade surfaces through the pressure/momentum boundary condition, Eqn. (2.3). The flow has to adjust dramatically around the blade surface oscillations and causes the large pressure oscillations. Therefore, the actual turning distribution, shown in Fig. (4.18) contain oscillations in the same axial locations. This is a deficiency because even though the total turning requirement was met, the local oscillations in the actual turning distribution are problematic.

This demonstrates that even though a camberline was designed the blade shape generated has problems. The design of camberline alone does not guarantee that the final blade shape will have desirable properties. Since a prescribed thickness that contained oscillations was chosen, the local oscillations in the blade surface produced oscillations in the pressure distribution which could potentially lead to separation, if they are too large. It can be concluded from this that consideration of the thickness must be included when designing a blade.

Text resumes on page 101

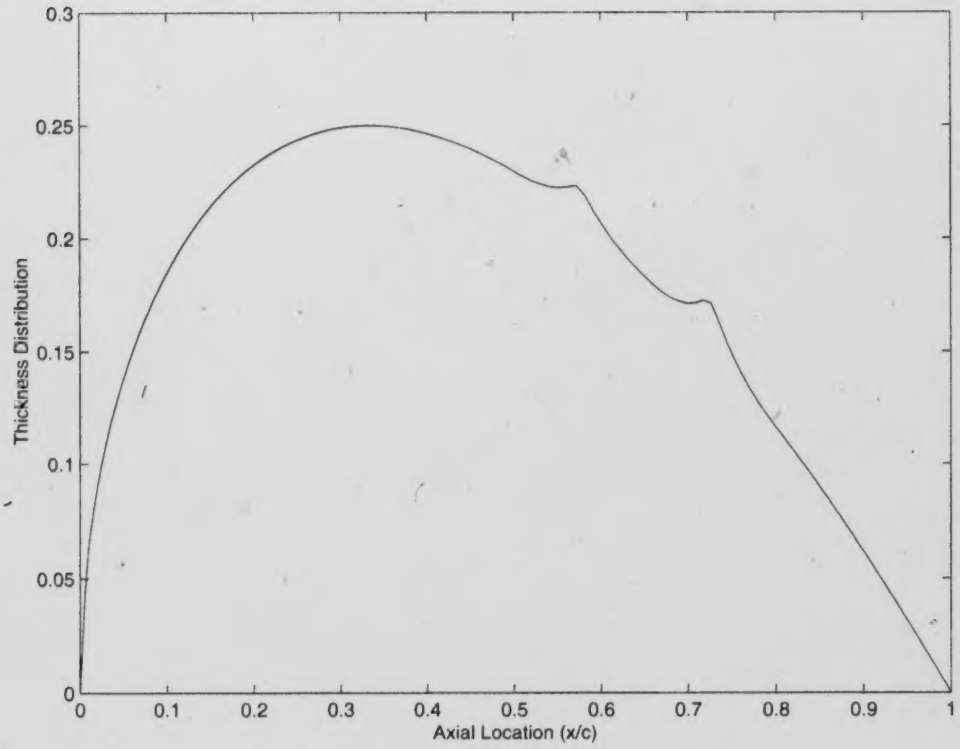

Figure 4.12: Subsonic Case 2: Prescribed Thickness Distribution

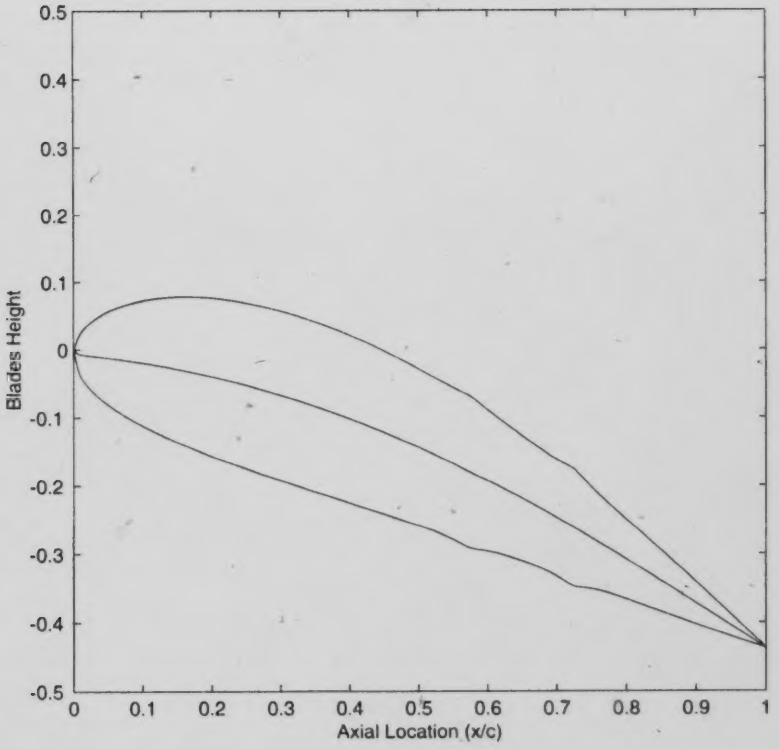

Figure 4.13: Subsonic Case 2: Converged Blade Shape

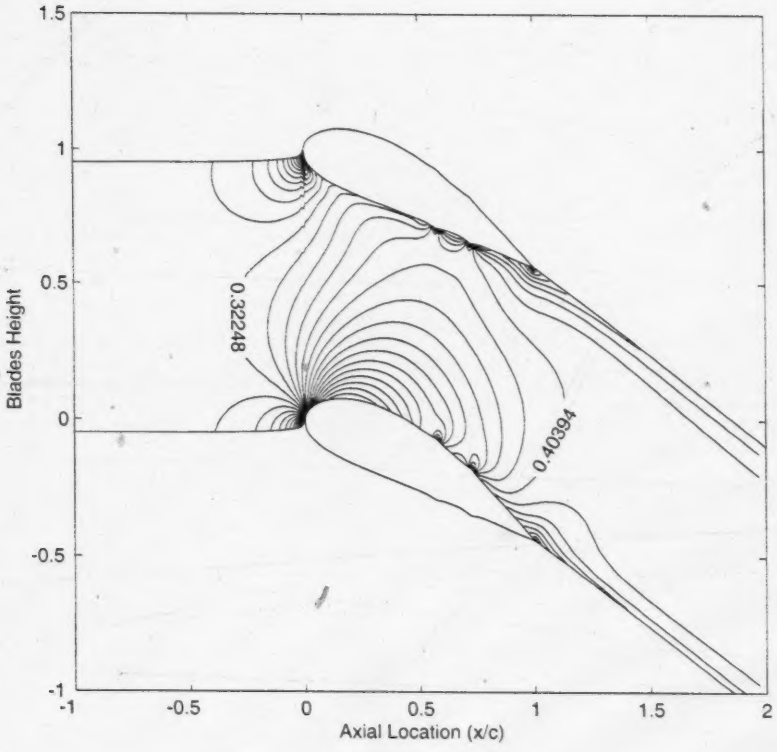

Figure 4.14: Subsonic Case 2: Contours of Mach Number in the Blade Passage

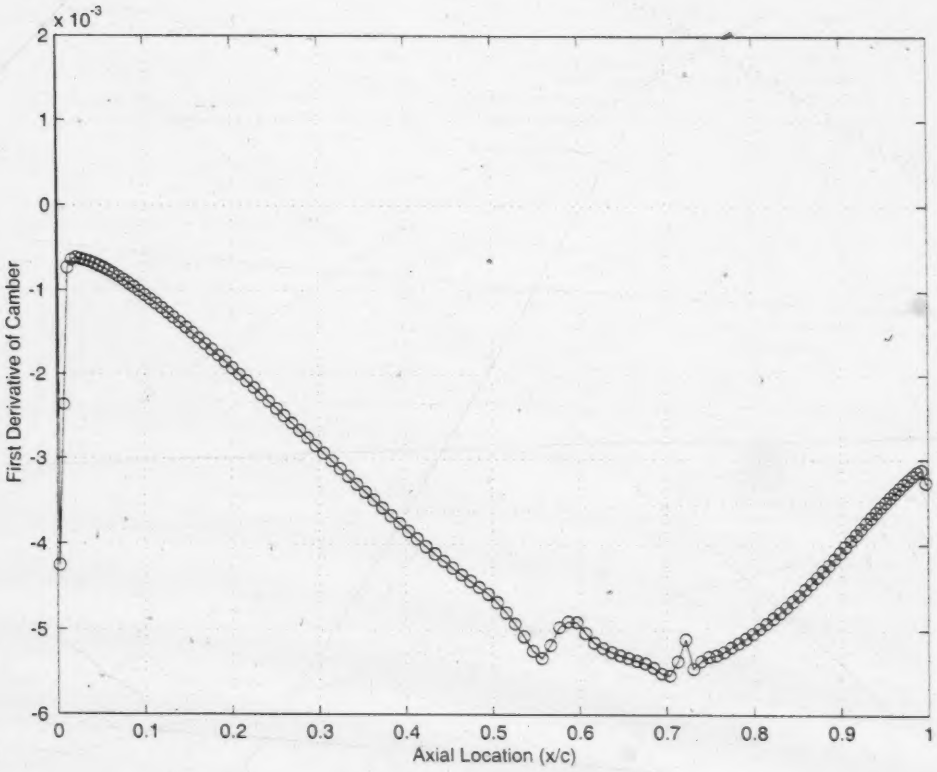

Figure 4.15: Subsonic Case 2: First Derivative of Camber

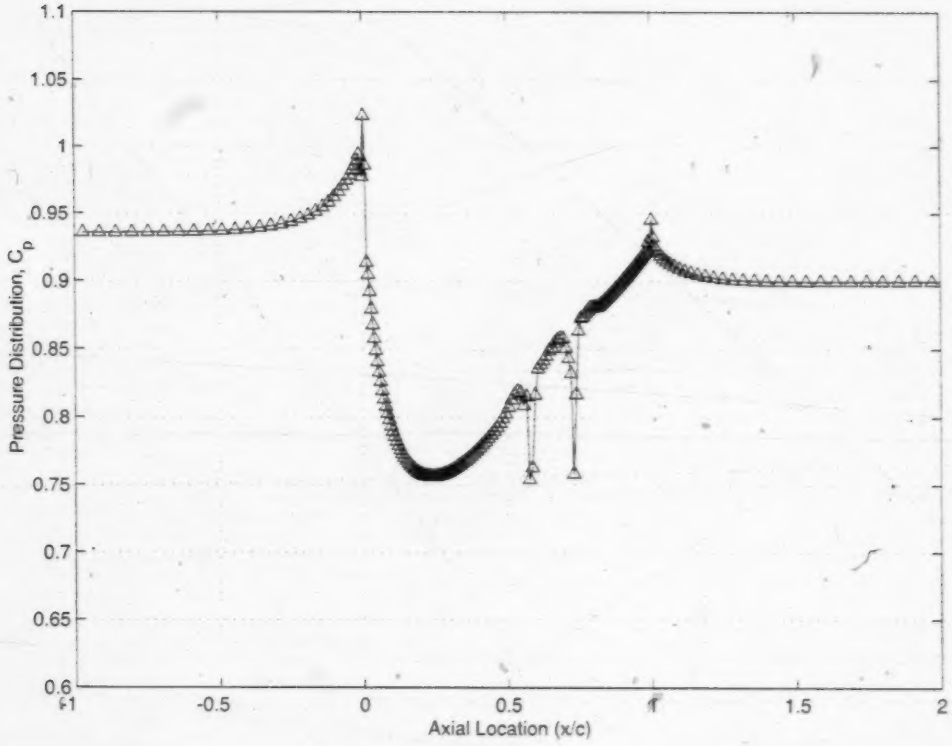

Figure 4.16: Subsonic Case 2: Pressure Distribution on Blade Surface - Suction Side

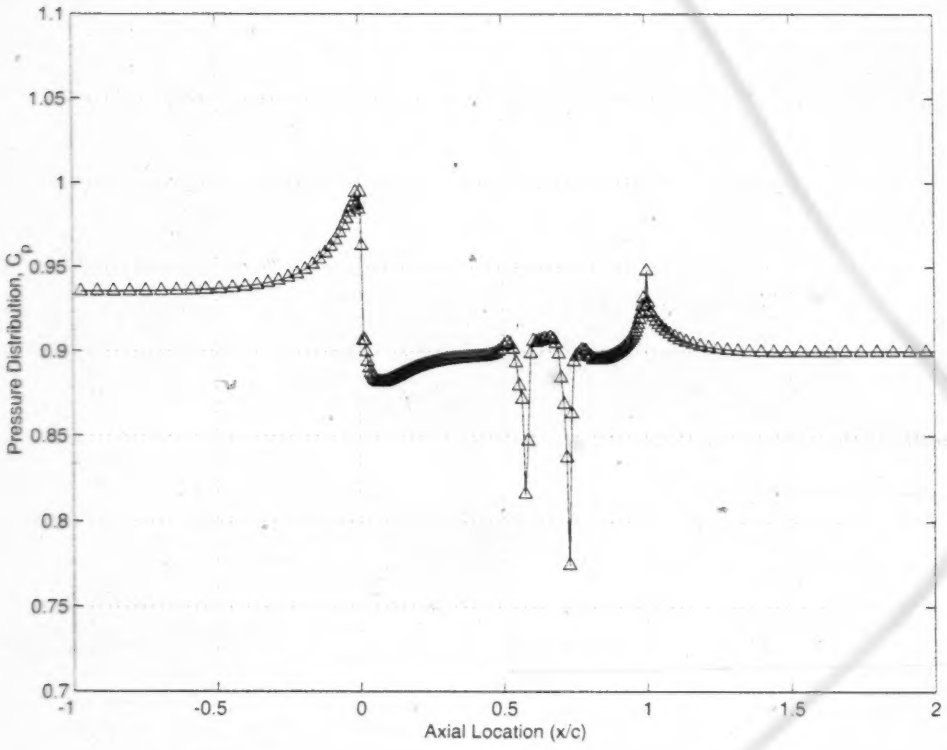

Figure 4.17: Subsonic Case 2: Pressure Distribution on Blade Surface - Pressure Side

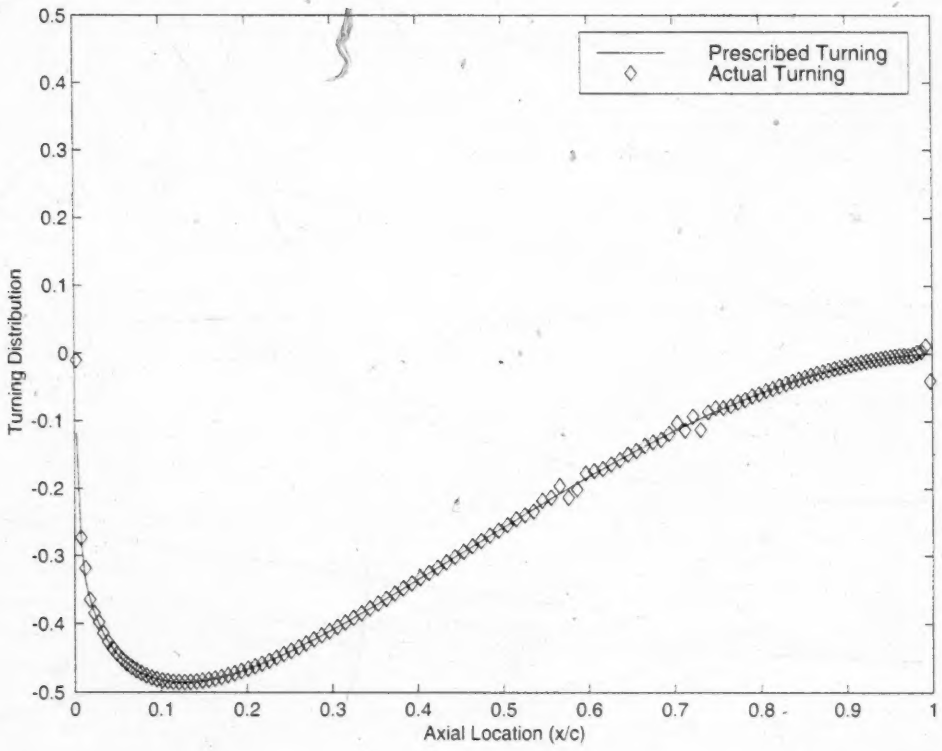

Figure 4.18: Subsonic Case 2: Turning Distributions in Blade Passage

4.1.3 Subsonic Case 3: New Design - Oscillations in Prescribed Thickness

The previous subsonic test case using a prescribed thickness with oscillations proved that even though a camberline was designed this was not enough to ensure that all aerodynamic characteristics would be satisfactory. Therefore a new design procedure is implemented to include the influence of the thickness along with the camberline.

Step 1: Thickness Generation

To complete the argument that the camberline design does not guarantee acceptable blade geometries, the same subsonic blade will be designed but using the new design procedure. Now that the design of the thickness is required, the camberline is initially prescribed. Along with the same smooth prescribed turning distribution, the previously generated camberline is used is used as a first guess. The design of the thickness is performed first. Due to the hyperbolic nature of the camberline, when both evolve simultaneously, it prevents the thickness is prevented from having any influence on the final design. Therefore, the thickness is allowed to be influenced by the prescribed turning while holding the camberline fixed.

The equation for the thickness, Eqn. (2.51), contains both surface velocities and camberline. To avoid being dominated by a discrepancy between the initial geometry and flow field, the same initial flow field, thickness and camberline are used. The evolution of the thickness will then be dominated by the influence of the turning and not by the initial discrepancy between the geometry and flow field. The overall benefit of the new design procedure is

illustrated more clearly by redesigning the previously ill-designed geometry from subsonic test case 2.

The initial thickness is the same thickness used previously containing the oscillations at approximate axial locations of 0.6 and 0.7. The initial thickness distribution is shown as the solid line in Fig. (4.19). The prescribed camberline is the converged camberline from the previous test case, therefore it has some small oscillations in it. The small oscillations can be seen by referring to Fig. (4.15) of the previous test case. This thickness is now allowed to change and can allow mass flux across the blade surfaces. This is clearly illustrated in plots of angle of blade surfaces and flow shown in Figs. (4.20) and (4.21). Again, the region of interest is across the blade, an axial location of 0 to 1. Note that, on the pressure side surface, the angle of the blade does not match the angle of the flow in the region of the oscillations. This indicates mass flux through the blade surface at these locations.

The thickness equations smoothed out the oscillations in the initial thickness shown in Fig. (4.19) as the line with triangular symbols. The influence of the smooth turning distribution has caused the thickness to smooth out. Since the oscillations in the blade surfaces have been smoothed out and mass flux is allowed across the blade surfaces, the flow through the passage, shown converged flow field Fig. (4.22), does not contain large contours around the location of the blade surface oscillations. A final benefit of this is that the large surface pressure oscillations seen in the previous test case have been significantly reduced, clearly shown in suction and pressure side pressure distributions, Figs. (4.23) and (4.24) respectively.

At this point, the thickness is smoother but because the camberline was

held constant it still contains small oscillations. The smoother thickness and mass flux across the blades surfaces led to an actual turning distribution which almost matches the prescribed, shown in Fig. (4.25), but is still not perfect. To eliminate the mass flux and complete all the turning requirements, the next step in the procedure will be to hold the thickness constant and allow the design of the camberline correct these deficiencies.

Text resumes on page 111

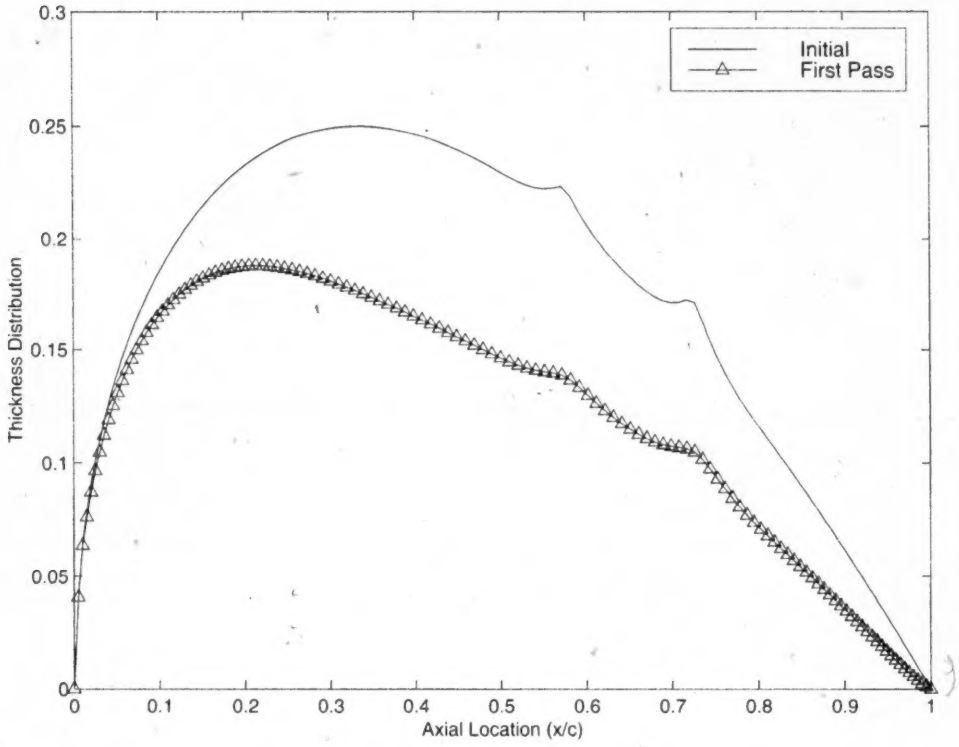

Figure 4.19: Subsonic Case 3: Step 1 - Prescribed and Calculated Thickness Distributions Passage

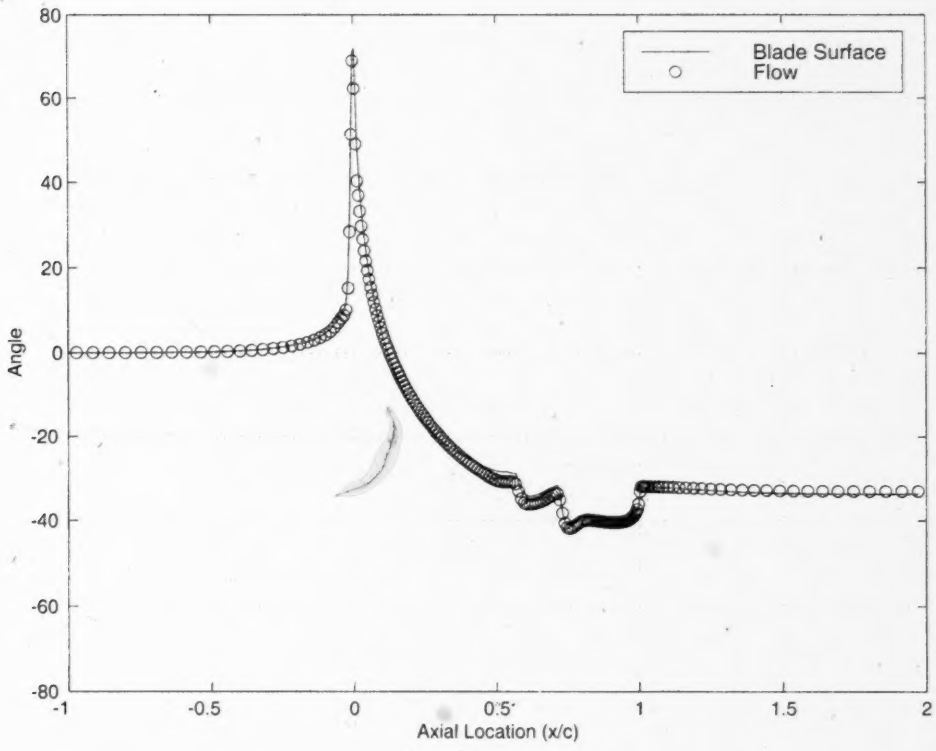

Figure 4.20: Subsonic Case 3: Step 1 - Blade and Velocity Angles - Suction Side

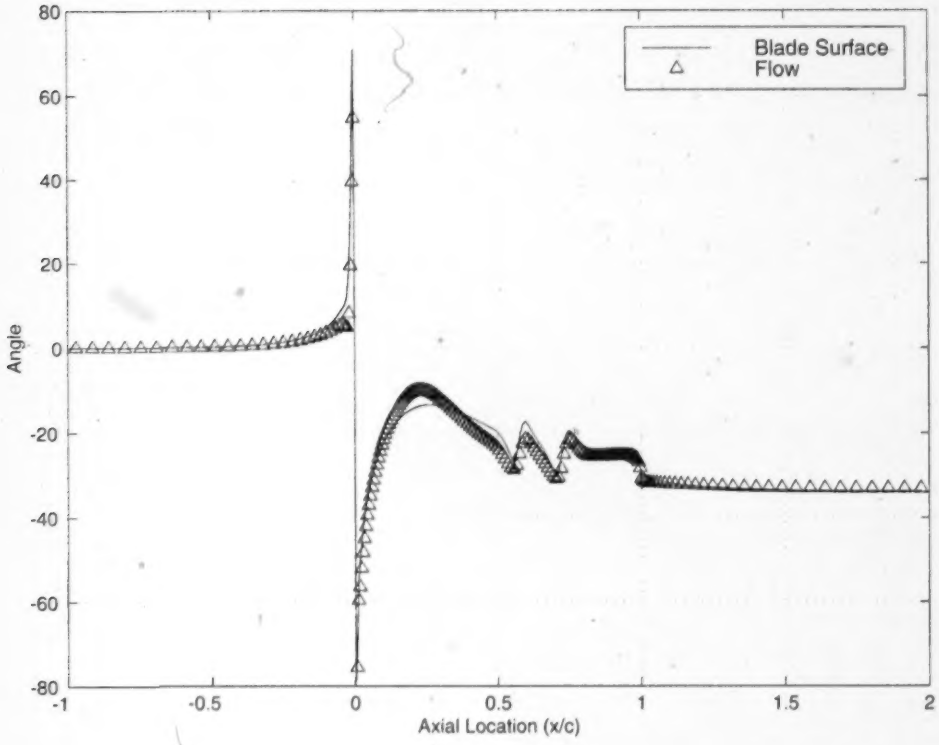

Figure 4.21: Subsonic Case 3: Step 1 - Blade and Velocity Angles - Pressure Side

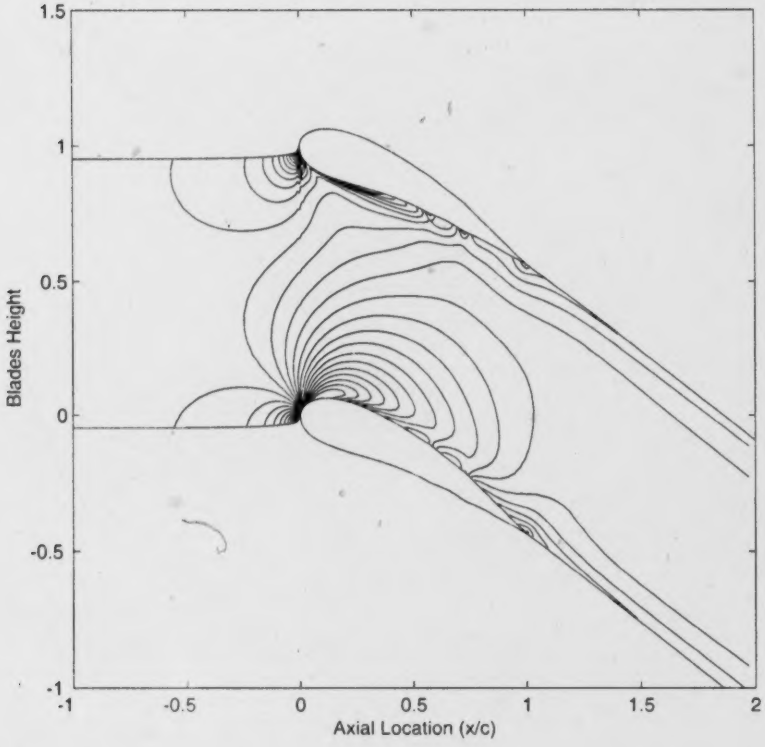

Figure 4.22: Subsonic Case 3: Step 1 - Contours of Mach Number in the Blade Passage

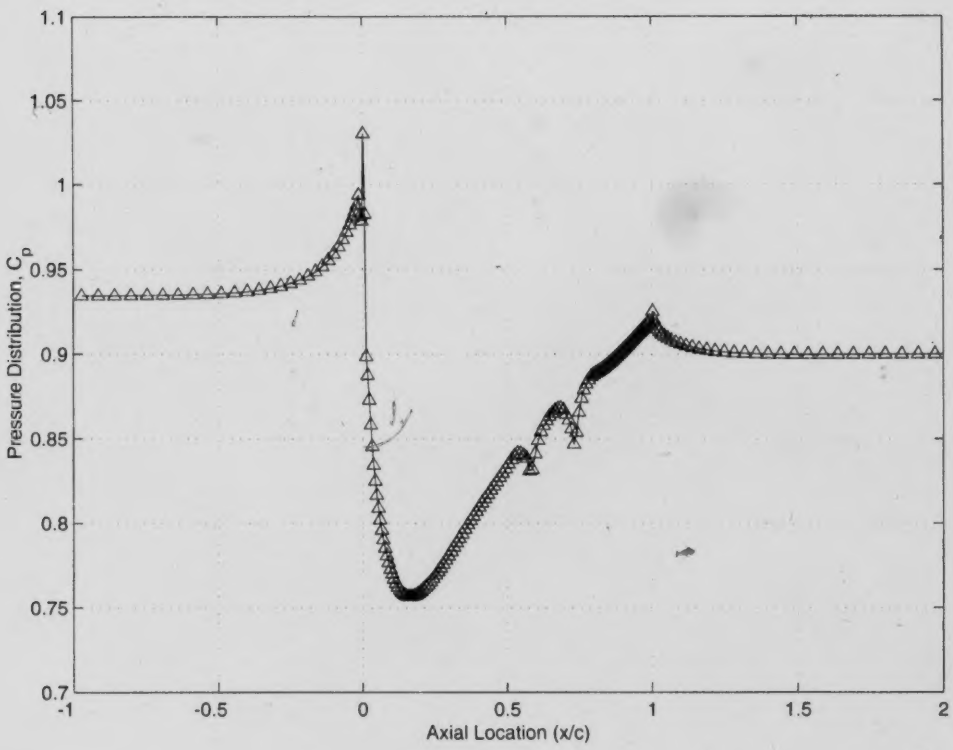

Figure 4.23: Subsonic Case 3: Step 1 - Pressure Distribution on Blade Surface - Suction Side

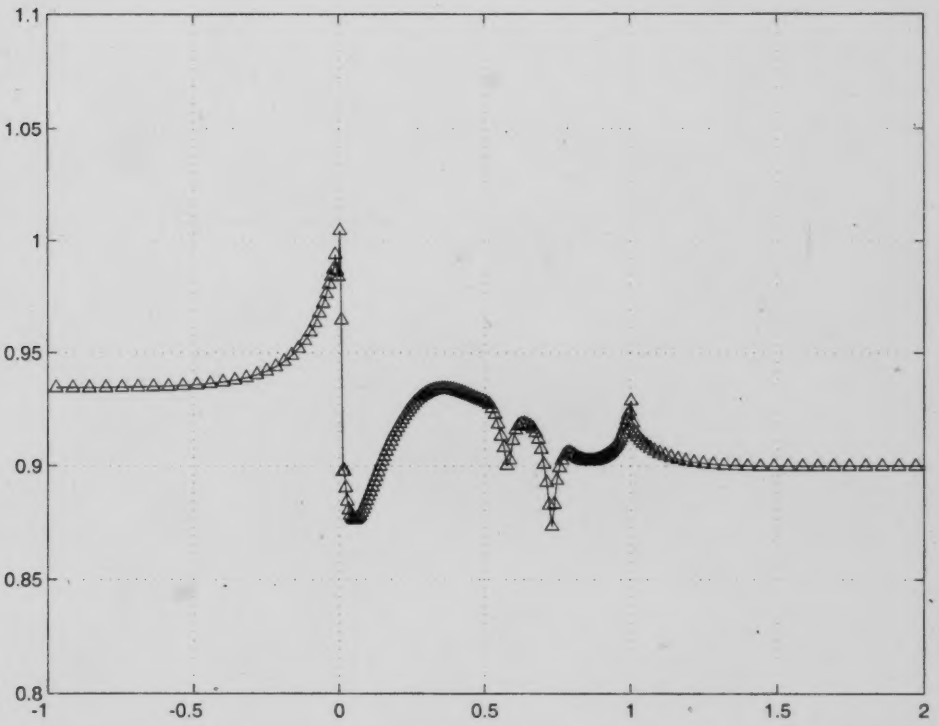

Figure 4.24: Subsonic Case 3: Step 1 - Pressure Distribution on Blade Surface - Pressure Side

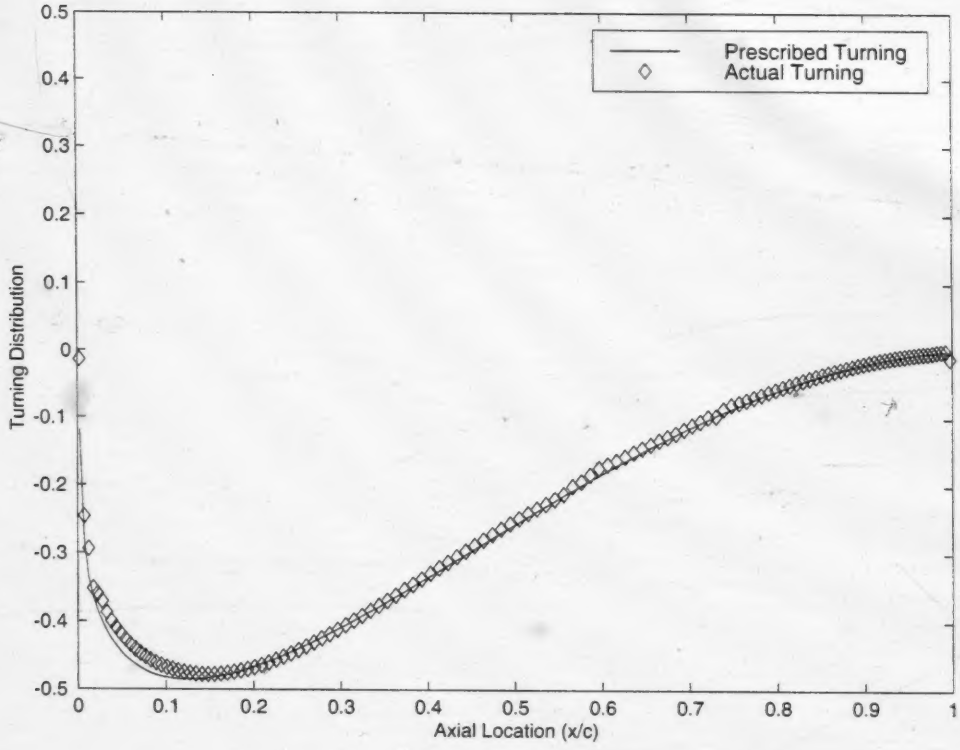

Figure 4.25: Subsonic Case 3: Step 1 - Turning Distributions in Blade Passage

Step 2: Camberline Generation

The next step in the design procedure is to hold the new thickness constant and allow the camberline to change. After the first step in the procedure there was mass flux across the blade surfaces and the turning requirements were not complete. To alleviate the remaining problems, the thickness is then constant and the camberline is modified. The camberline generator can now remove the oscillations present in the initial camberline. As well, the camberline generator can eliminate the mass flux across the blades surfaces, as shown in Figs. (4.26) and (4.27). Note that, on the pressure side (Fig. (4.27)), in the region of the oscillations, the flow now matches the angle of the blade closely. The converged blade surfaces, shown Fig. (4.28), have much smaller oscillations than test case 2. This is even more evident in the plot of the Mach number contours through the blade passage, shown in Fig. (4.29), where the contours around the region of the oscillations are much less noticeable.

As a result of the reduction in size and smoothing of the blade surface oscillations, the surface pressure distributions, shown Figs. (4.30) and (4.31), are much better than that of the blade from the second subsonic test case. By being able to smooth out or eliminate oscillations in the pressure distributions, the possibility of separation in a real flow is greatly reduced.

A final benefit of the smoothing and reduction of the blade surface oscillations is seen in the actual turning distribution. The oscillations in the actual turning distribution, shown in Fig. (4.32) have almost been completely eliminated. Only very small oscillations occur in the region of the blade surface oscillations.

A method has been developed which can eliminate unwanted anomalies in the aerodynamic characteristics of the blade. The characteristics of the converged blade are still not quite perfect, therefore another iteration of the entire procedure is applied to this blade again to generate a blade that matches the turning distribution perfectly. The combination of this step with the first one is the new design procedure. By allowing the thickness to be designed first, and then allowing the camberline to change, both now have influence on the final design.

Text resumes on page 120

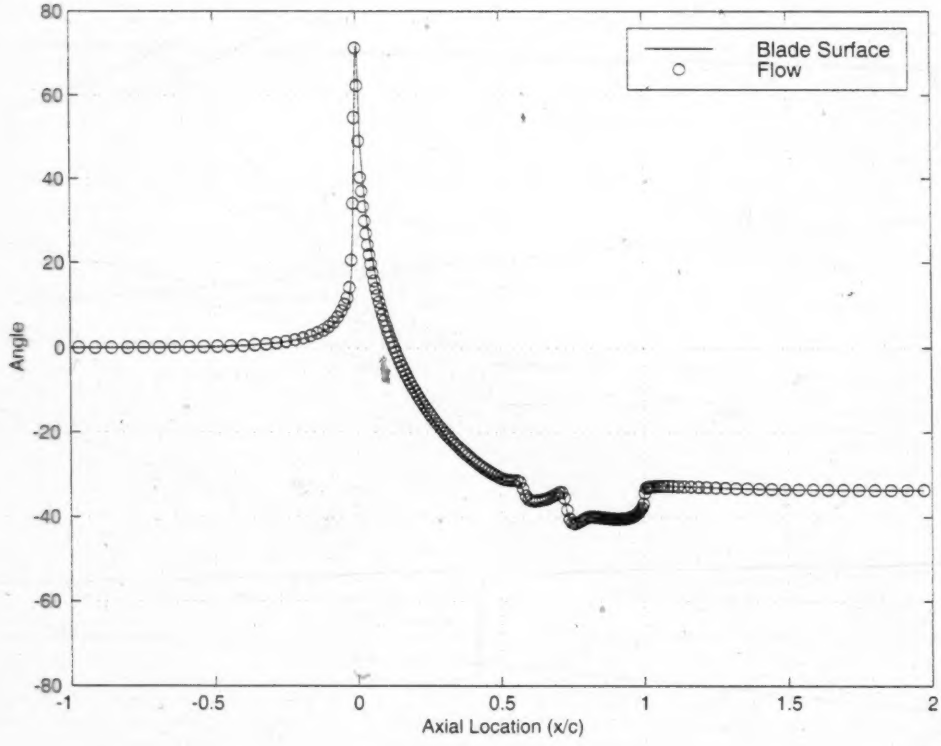

Figure 4.26: Subsonic Case 3: Step 2 - Blade and Velocity Angles - Suction Side

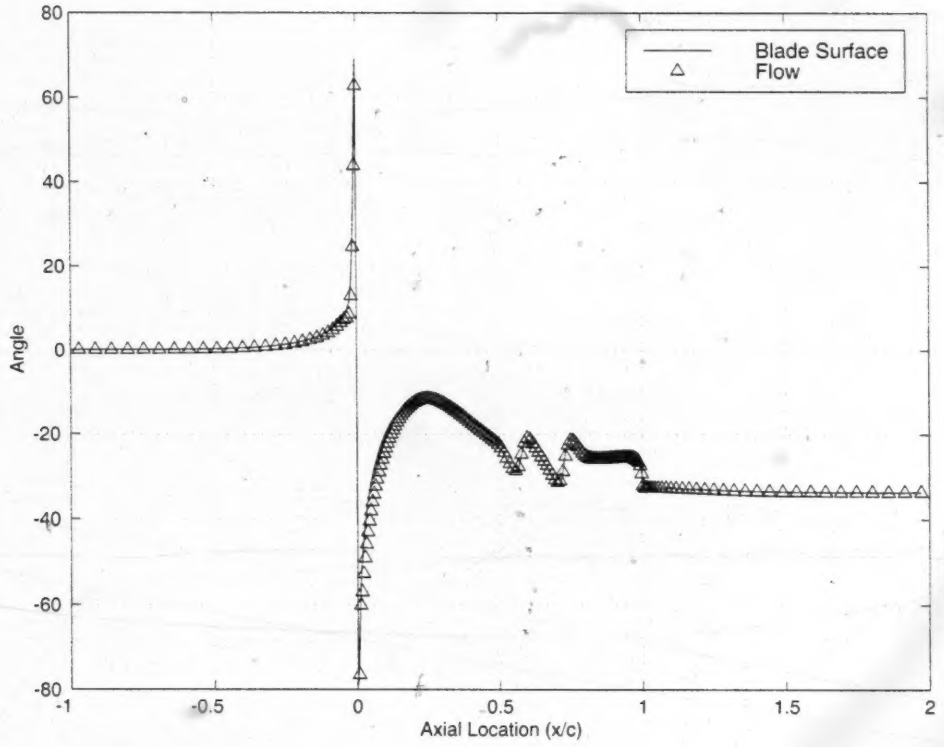

Figure 4.27: Subsonic Case 3: Step 2 - Blade and Velocity Angles - Pressure Side

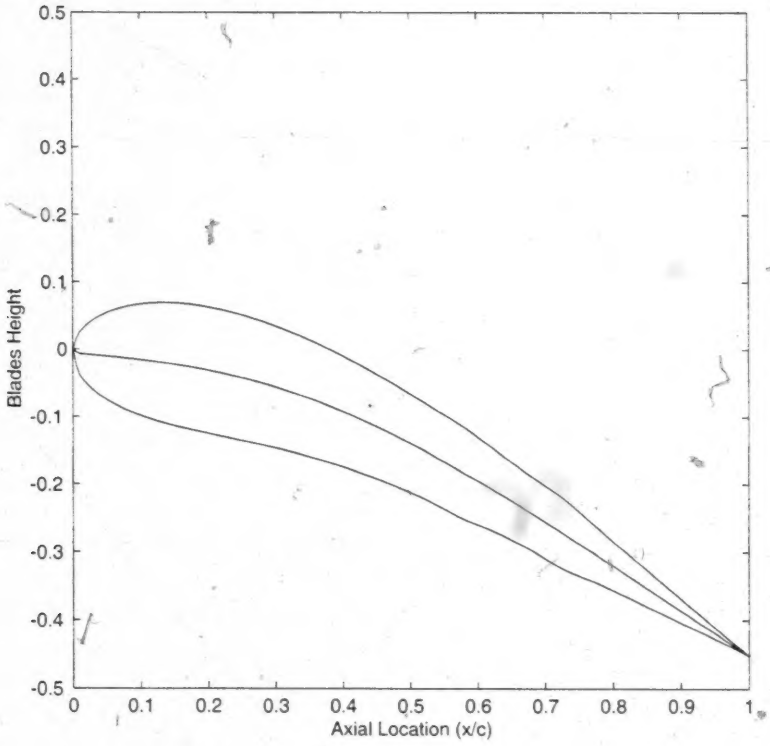

Figure 4.28: Subsonic Case 3: Step 2 - Converged Blade Shape

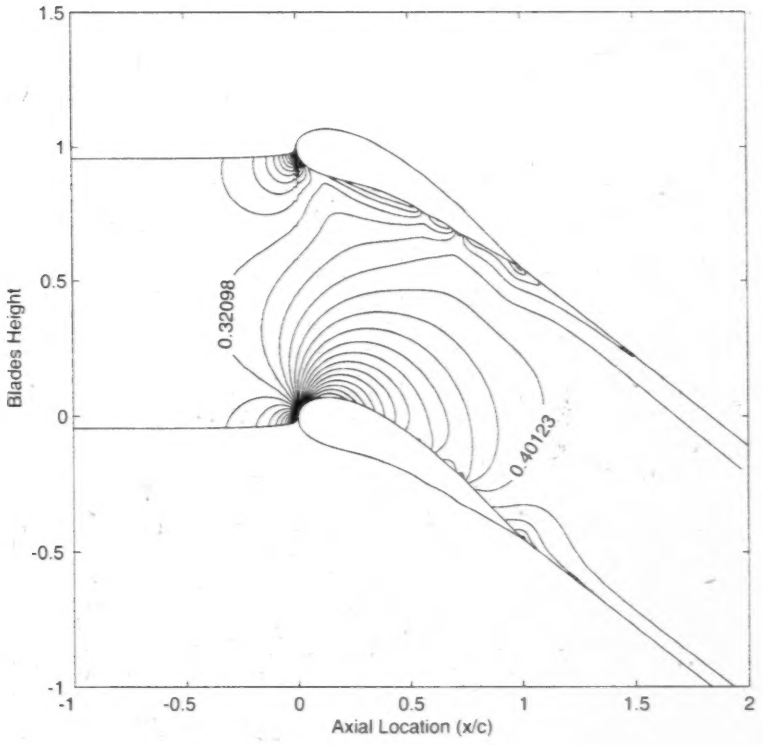

Figure 4.29: Subsonic Case 3: Step 2 - Contours of Mach Number in the Blade Passage

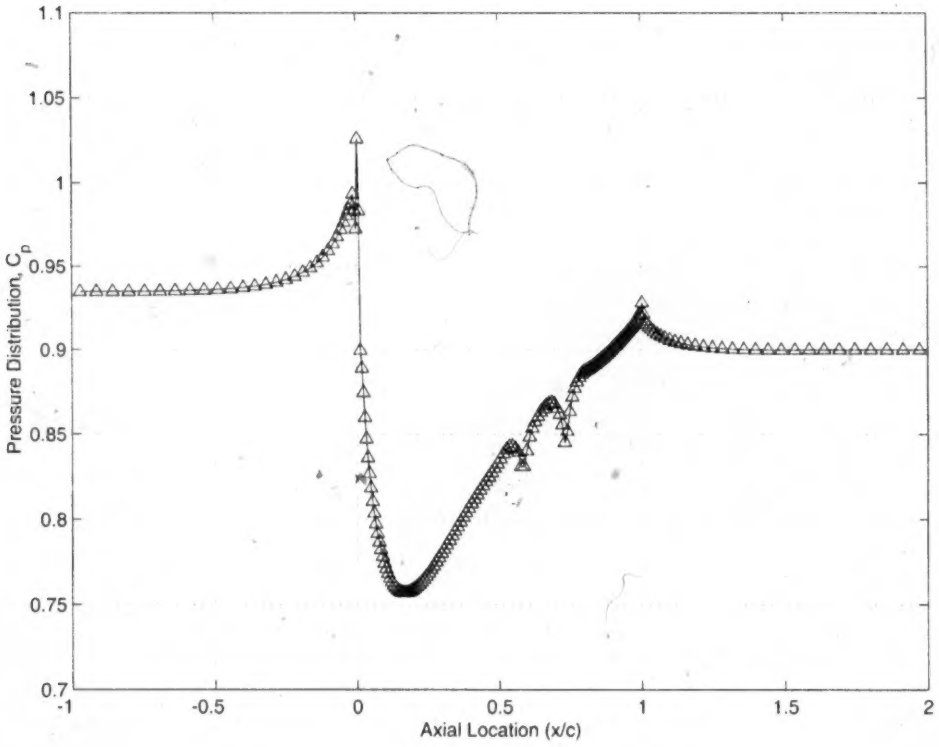

Figure 4.30: Subsonic Case 3: Step 2 - Pressure Distribution on Blade Surface - Suction Side

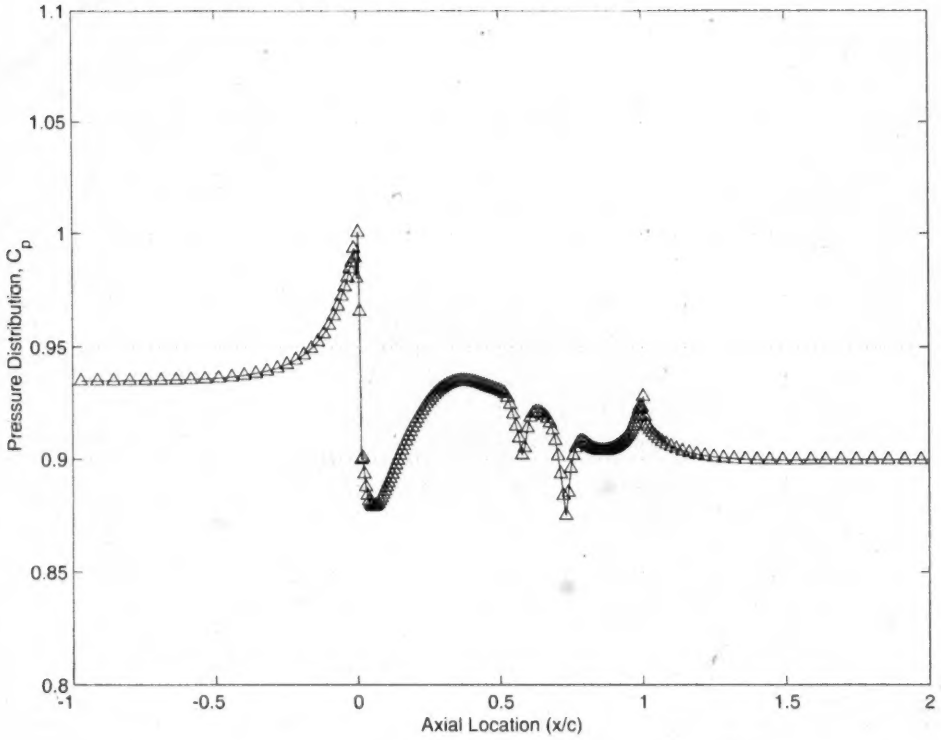

Figure 4.31: Subsonic Case 3: Step 2 - Pressure Distribution on Blade Surface - Pressure Side

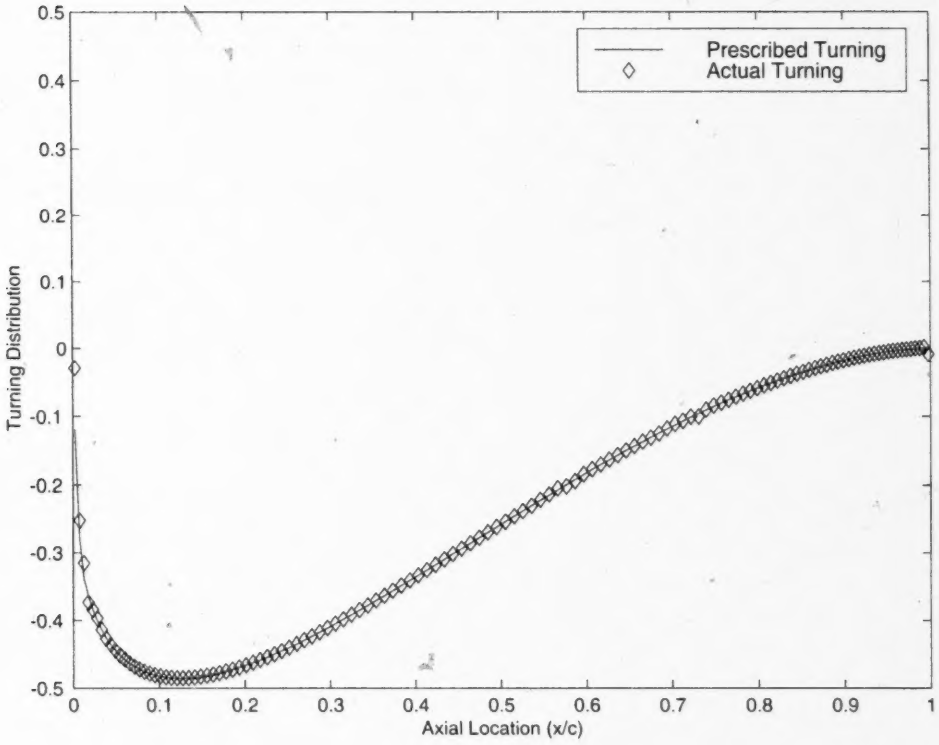

Figure 4.32: Subsonic Case 3: Step 2 - Turning Distributions in Blade Passage

Repeat of Design Procedure

Starting with the final thickness and flow field from the first pass, another iteration of the design procedure is required to remediate the small oscillations in the blade surfaces, actual turning distribution and pressure distributions. For the second pass of the design procedure, the prescribed camberline from the first step is used. The reason is because the designed thickness from the first pass was designed based on this camberline. By restarting the thickness design with a different camberline will cause the thickness to converge to a different solution.

The full design procedure (Steps 1 and 2) was performed once again. The plot comparing the initial thickness, thickness from the first pass and thickness from the second pass is shown in Fig. (4.33). Upon each consecutive pass of the design procedure the oscillations in the thickness have been reduced and smoothed. This is because the thickness is allowed to change and is influenced by the smooth turning distribution. Although the maximum thickness is reduced again, it is noted that the relative amount by which it did this is considerably less than after the first pass.

The blade surfaces seen in Fig. (4.34) contain almost no visible oscillations where they were previously at approximate axial locations of 0.6 and 0.7. This is due to smoothing of thickness distribution. The benefit of the smooth blade surfaces is evident in Fig. (4.35), where there is almost no change of the flow field around the previous location of the blade surface oscillations.

Further benefit is illustrated by the pressure distributions of Figs. (4.36) and (4.37) where the oscillations are considerably smaller than the large os-

cillations present in the pressure distributions of the previous test case. Of notable interest is the actual turning distribution shown in Fig. (4.38). It now contains no oscillations thus meeting the global and local turning requirements. To be complete, to show that the camberline generator enforces the no-flux condition, plots of angle of the blade and flow on both surfaces are shown in Figs. (4.39) and (4.40). This provides conclusive evidence that once the camberline has converged mass flux through the blades is eliminated. Repeated iterations of this procedure would converge the blade to a final, unchanging shape and would undoubtedly have all oscillations removed in the turning and pressure distributions. The convergence history is shown in Fig. (4.41). The jump in the residual at 60,000 iterations is due to the calculation changing from design of thickness, Step 1, to design of the camberline, Step 2.

The purpose of these subsonic test cases was to provide conclusive evidence that design of both the camberline and thickness is required when constructing a blade. Clear evidence was shown through the surface pressure distributions. By eliminating oscillations in the pressure distributions there is a less likely chance that separation would occur with the design in a real flow. The first test case was used to show that the camberline generator enforces the no-flux condition on the blade surfaces when it was converged. The second test was used to show that an arbitrarily prescribed thickness can cause the final geometry to yield undesirable characteristics. This was illustrated through the large oscillations in the pressure distributions caused by the oscillations present in the blade surfaces. The final test case, the description of a design procedure including both camberline and thickness

results, shows how consideration of thickness design can alleviate the problems previously encountered when only camberline was considered.

Text resumes on page 132

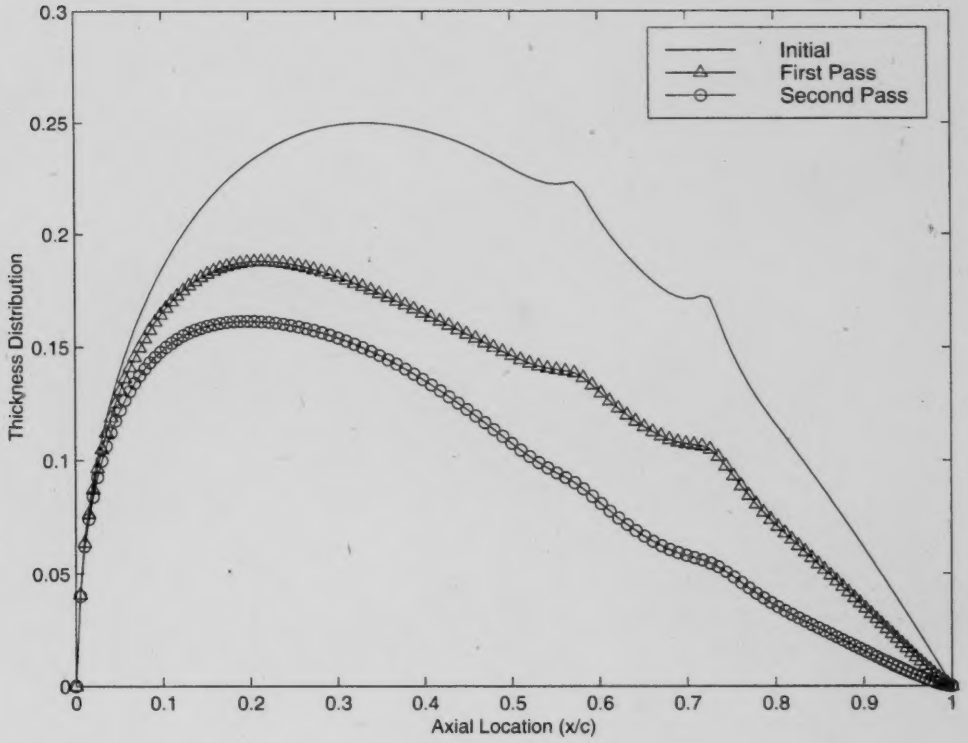

Figure 4.33: Subsonic Case 3: Prescribed and Calculated Thickness Distributions

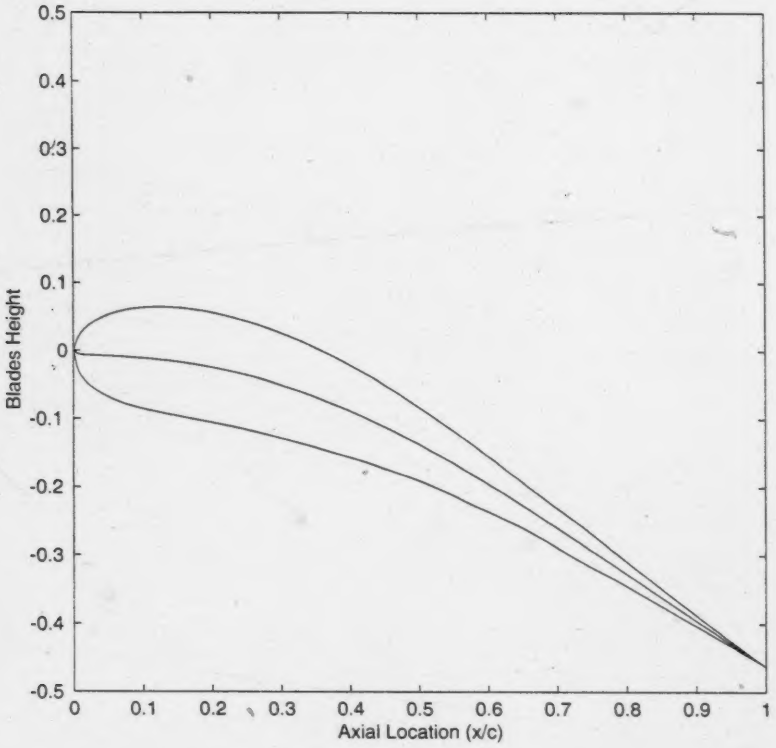

Figure 4.34: Subsonic Case 3: Converged Blade Shape

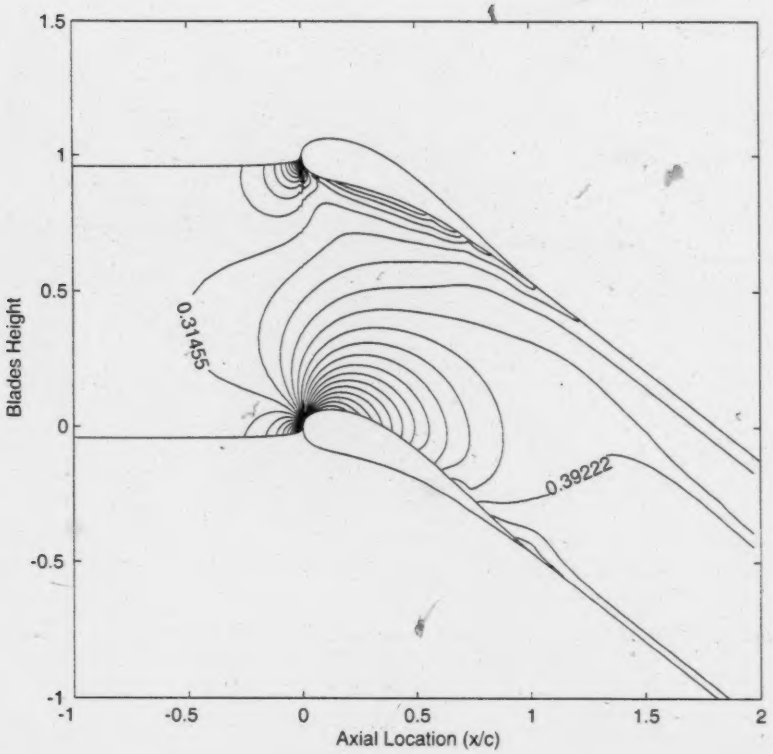

Figure 4.35: Subsonic Case 3: Contours of Mach Number in the Blade Passage

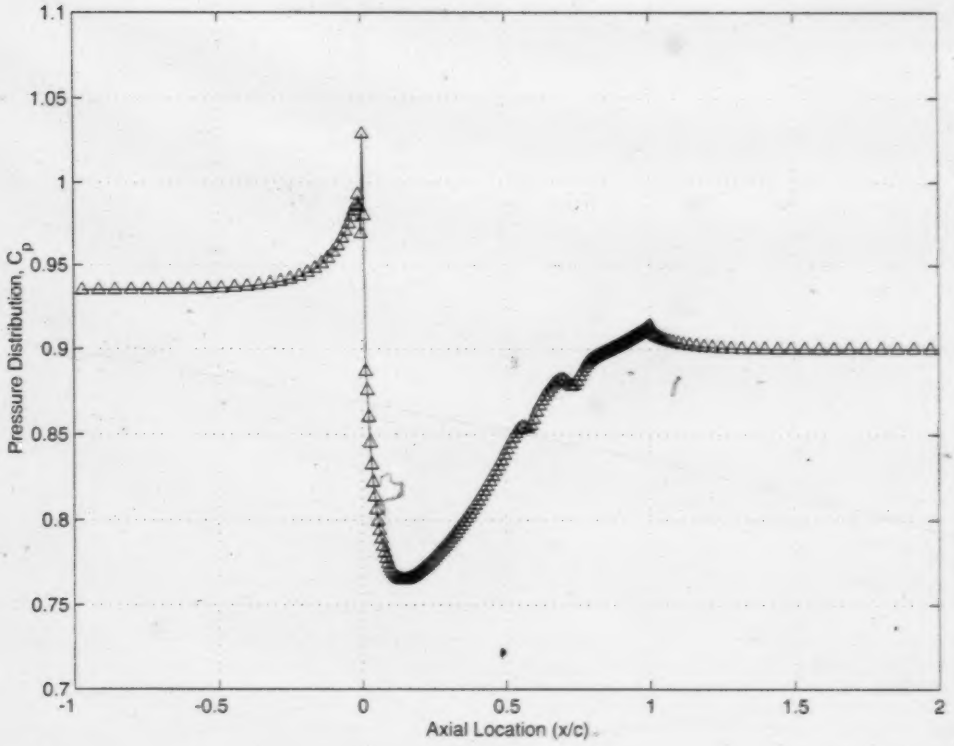

Figure 4.36: Subsonic Case 3: Pressure Distribution on Blade Surface - Suction Side

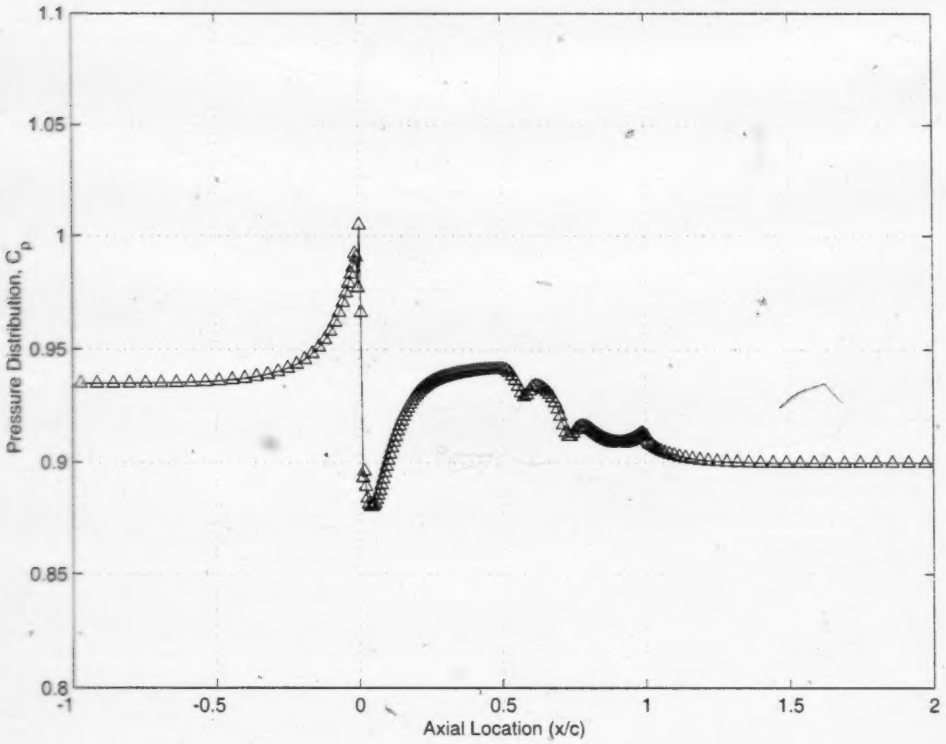

Figure 4.37: Subsonic Case 3: Pressure Distribution on Blade Surface - Pressure Side

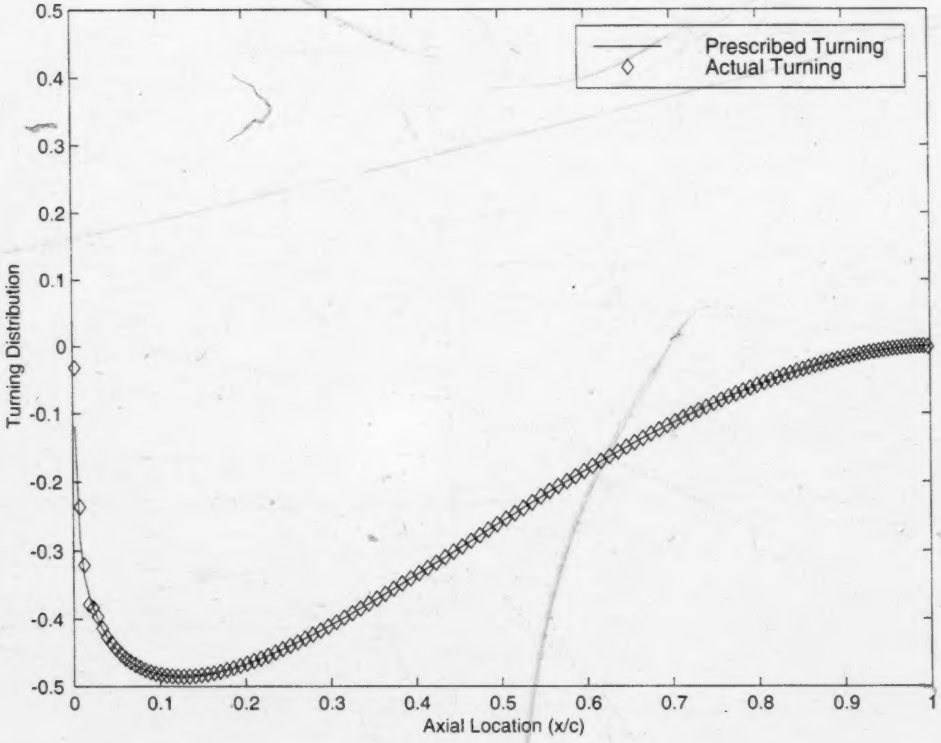

Figure 4.38: Subsonic Case 3: Turning Distributions in Blade Passage

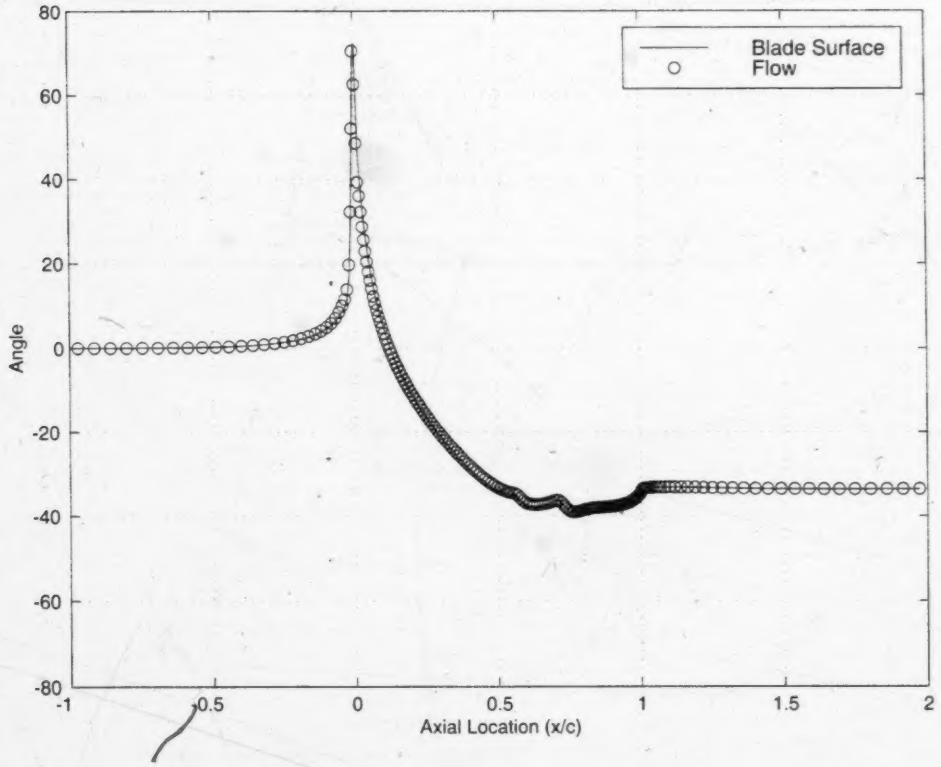

Figure 4.39: Subsonic Case 3: Blade and Velocity Angles - Suction Side

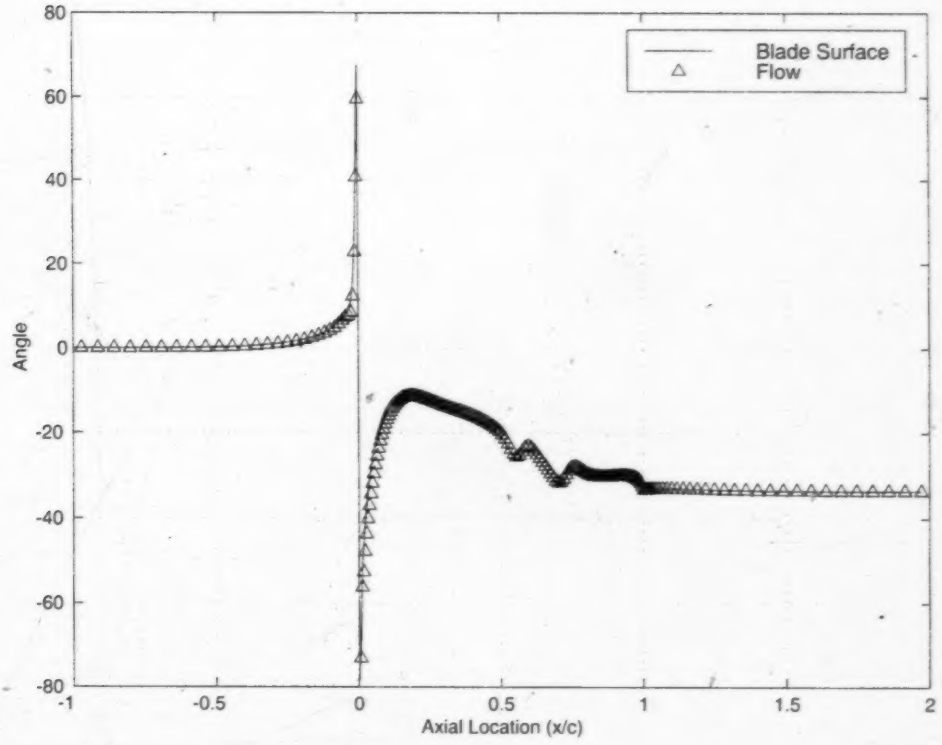

Figure 4.40: Subsonic Case 3: Blade and Velocity Angles - Pressure Side

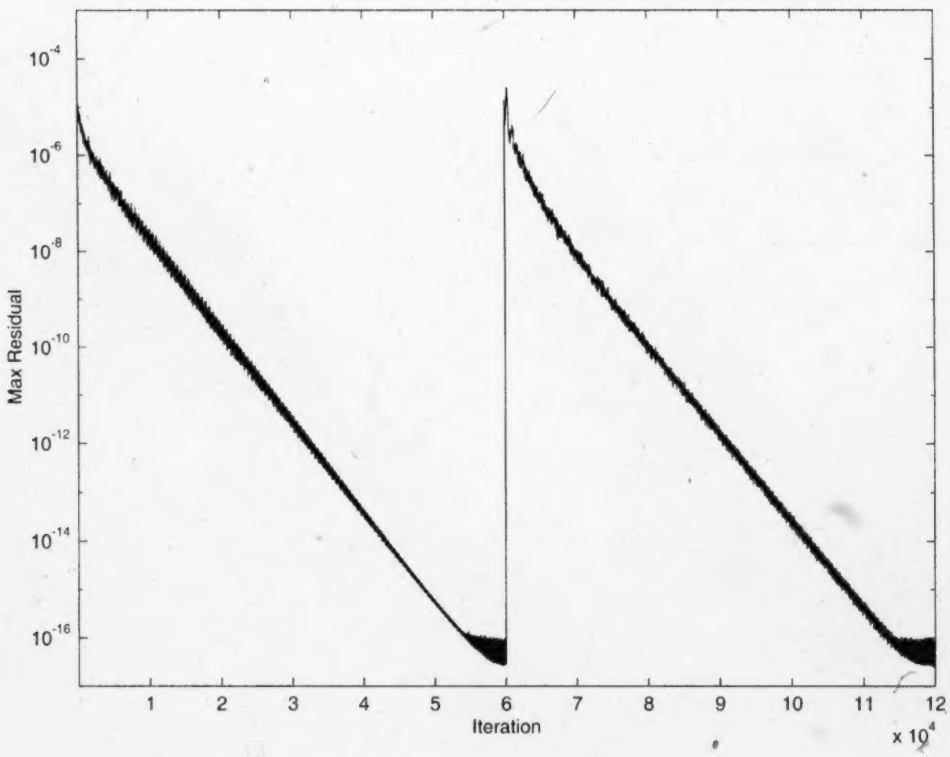

Figure 4.41: Subsonic Case 3: Convergence History

4.2 Transonic Test Cases

Another flow regime in which turbomachinery can operate is the transonic flow regime. An obvious example would be the engines in long range aircraft which fly at velocities close to the speed of sound. Two test cases in the transonic flow regime are included to provide final evidence that the design of the thickness can not be neglected. The first test case is one where the inverse design of a discontinuous blade geometry was caused by the development of a strong shock in the passage. This again illustrates that the inverse design of the camberline alone is not enough to obtain practical blade designs. The second test case employs the new design procedure described in the previous section. The new design procedure is able to deal with the effect of the shock in the passage and generate a continuous blade geometry. This is due to the fact that both thickness and camberline are inversely designed.

The first test case is reiterated from Medd [Medd 1998], therefore the same input parameters will be used. The second transonic test case uses the new design procedure. Both transonic test cases use the same input parameters except for the prescribed thicknesses and camberlines. The cascade is designed by specifying a back pressure of $P = 0.65P_o$, a spacing to chord ratio of $SC = 0.55$ and an inlet flow angle at $\beta = 20°$. The same smooth turning distribution is prescribed in all subsonic cases. It is generated from $\frac{d\bar{v}_y}{dx} = K\cos(\frac{\pi x}{2})$ shown in Fig. (4.42), where the scalar constant K is found form Eqn. (3.69) and the total turning specified as $\Delta\bar{v}_y = -0.783\sqrt{\gamma R\Theta_o}$.

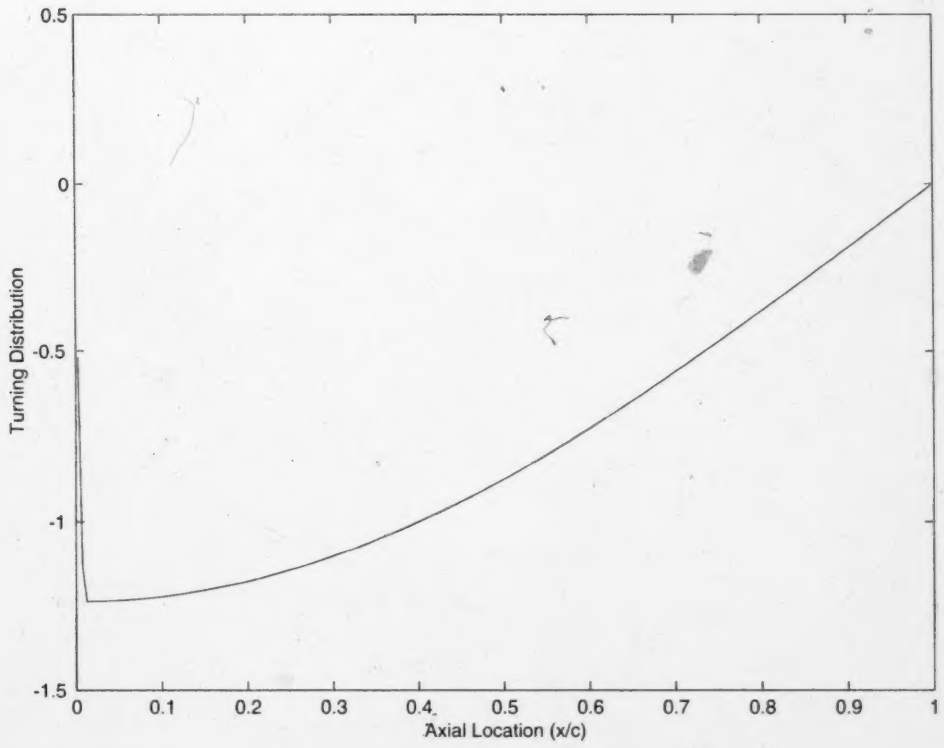

Figure 4.42: Prescribed Turning Distribution for Transonic Cases

4.2.1 Transonic Case 1: Camberline Generation - Discontinuous Geometry

This test case was previously shown by Medd [Medd 1998] and Yokota and Medd [Yokota & Medd 2002] where a transonic blade was generated with a discontinuity in the camberline due to a passage shock. A smooth thickness distribution of the form $T = kx^{\frac{1}{2}}(1-x)$ is prescribed, shown in Fig. (4.43), where the constant k is chosen to ensure a maximum thickness to spacing ratio of $\frac{T_{max}}{S} = 0.3$. Again this thickness distribution was chosen based primarily on aesthetics.

In Fig. (4.44), Mach number contours of the converged flow field, a strong shock has clearly developed at an approximate axial location of 0.75. The shock has developed in a vertical direction from the suction side surface to the pressure side surface at approximately the same axial location on each surface. The arbitrarily chosen thickness was too thick and the blade passage is behaving similar to a supersonic convergent divergent nozzle. The flow has accelerated past sonic speed as the thickness increases beyond the leading edge. As the thickness decreases towards the trailing edge, the passage opens and the supersonic flow must suddenly decelerate causing the shock.

Having specified a smooth turning distribution and a smooth thickness distribution, the camberline adjustment should produce smooth pressure distributions along the blade surfaces but due to the passage shock this is not possible. The shock causes a flow expansion downstream to counter the sudden compression. The camberline compensates to the sudden change in direction of the flow by creating a discontinuity at the location of the shock. This is clearly seen in Fig. (4.45), a plot of the converged blade where the

mid-line is the camberline. Due to the way the camberline and thickness are combined to create the blade, the surfaces also contain this discontinuity.

The discontinuity in the blade surfaces cause large discontinuities in the surface pressure distributions as shown in Figs. (4.46) and (4.47). There is again a conflict of competing influences between the pressure distributions and prescribed turning distribution. The pressure/momentum boundary condition Eqn. (2.3) tries to specify smooth blade pressures but can not due to the large pressure jump created by the shock. The total turning requirement is met but large localized oscillations occur in the actual turning distribution, as shown in Fig. (4.48), at approximately the same location of the shock.

Testing of this blade in a viscous fluid would most assuredly produce separation with conclusive evidence shown by the large discontinuities in the pressure distributions, Figs. (4.46) and (4.47), at the location of the shock. It is again obvious that an arbitrarily chosen thickness can not guarantee the design of a practical blade. There is no way to know prior to a calculation what thickness would avoid a shock. Therefore, in this case the thickness was chosen too thick and a shock developed. The shock not only caused a discontinuous geometry but would also incur a large energy loss across the blade row. For completeness, the convergence history of the residual, shown in Fig. (4.49), shows the residual converged to machine zero.

Text resumes on page 143

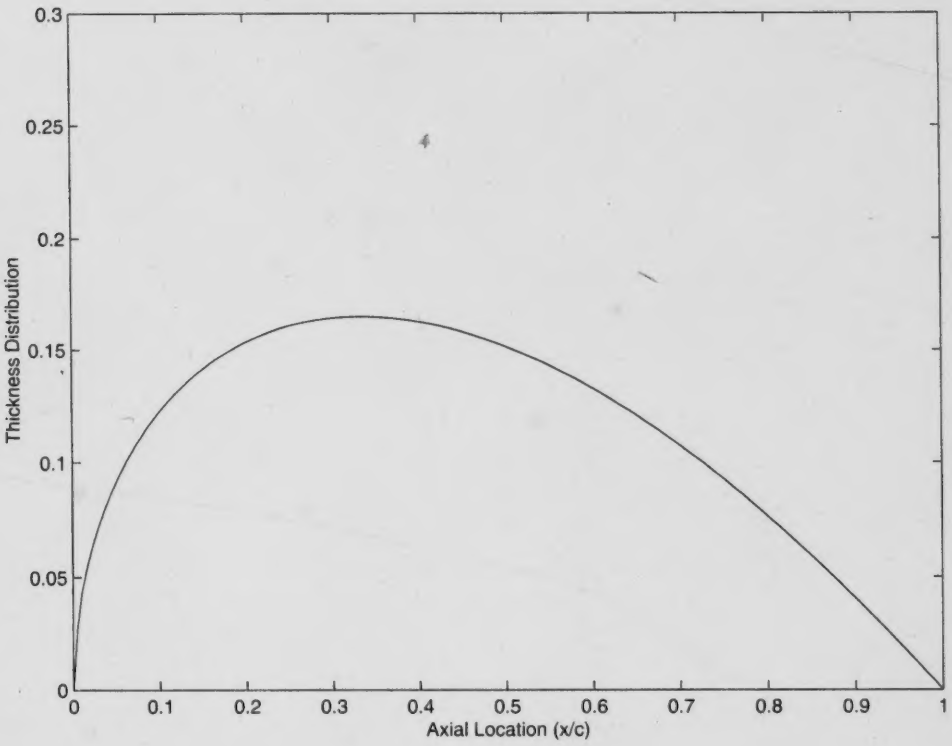

Figure 4.43: Transonic Case 1: Prescribed Thickness Distribution

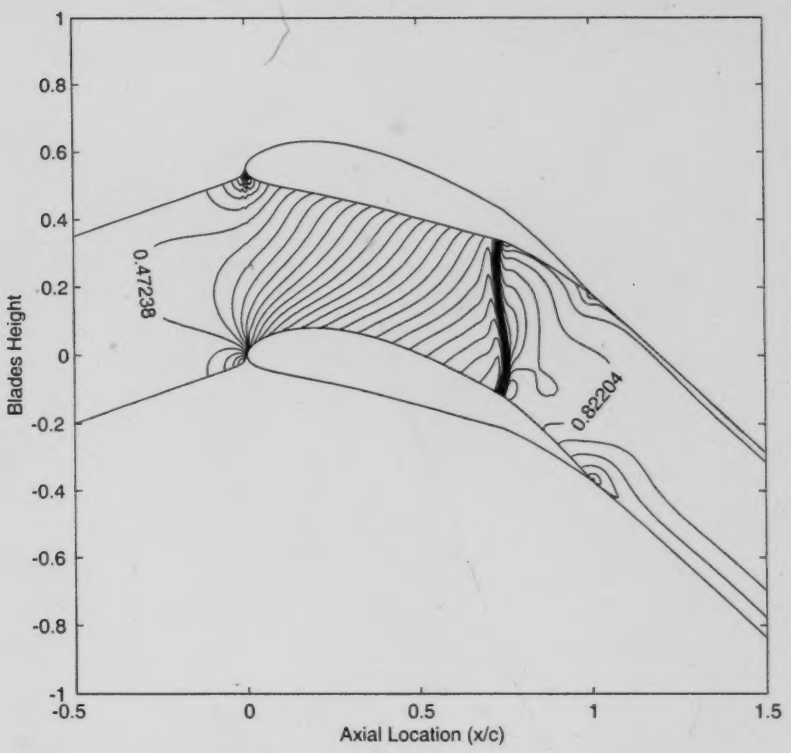

Figure 4.44: Transonic Case 1: Contours of Mach Number in the Blade Passage

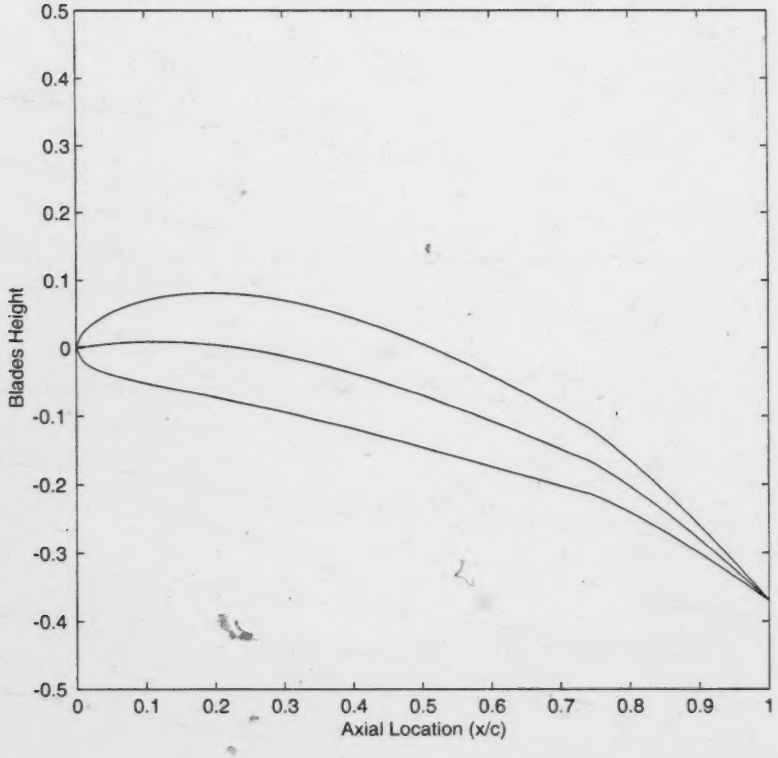

Figure 4.45: Transonic Case 1: Converged Blade Shape

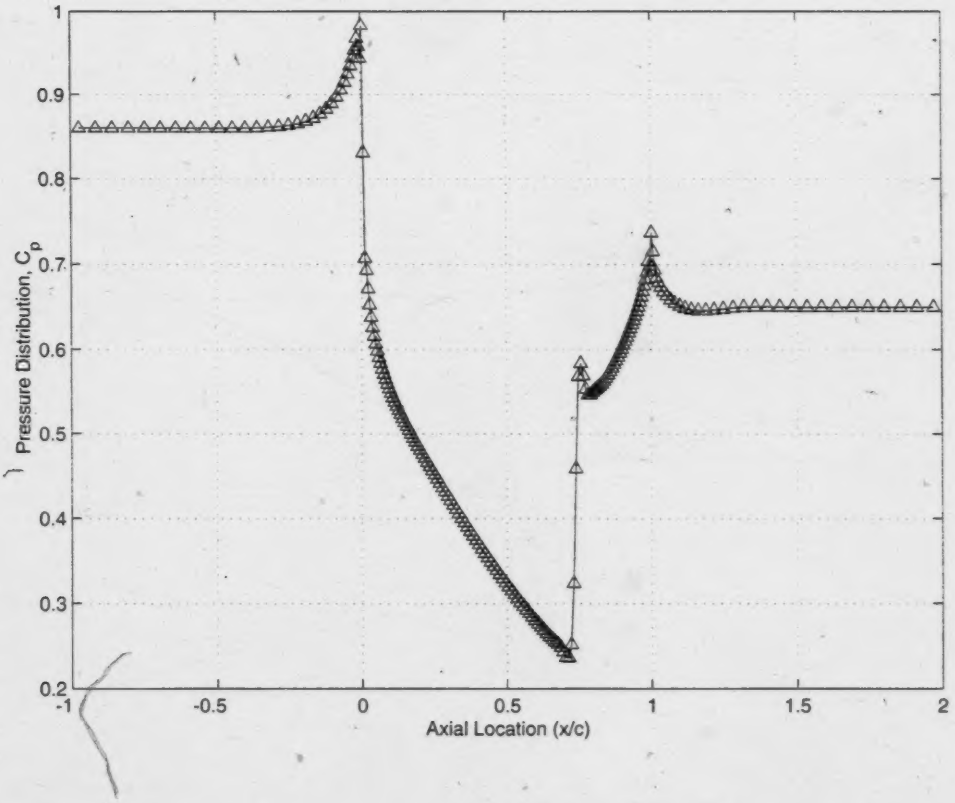

Figure 4.46: Transonic Case 1: Pressure Distribution on Blade Surface - Suction Side

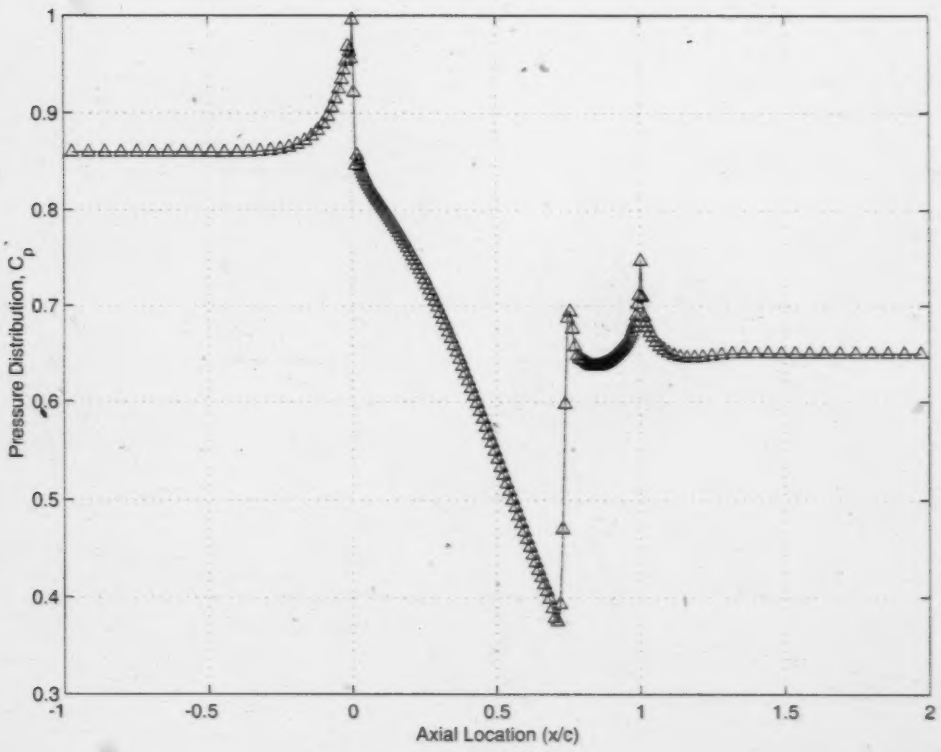

Figure 4.47: Transonic Case 1: Pressure Distribution on Blade Surface - Pressure Side

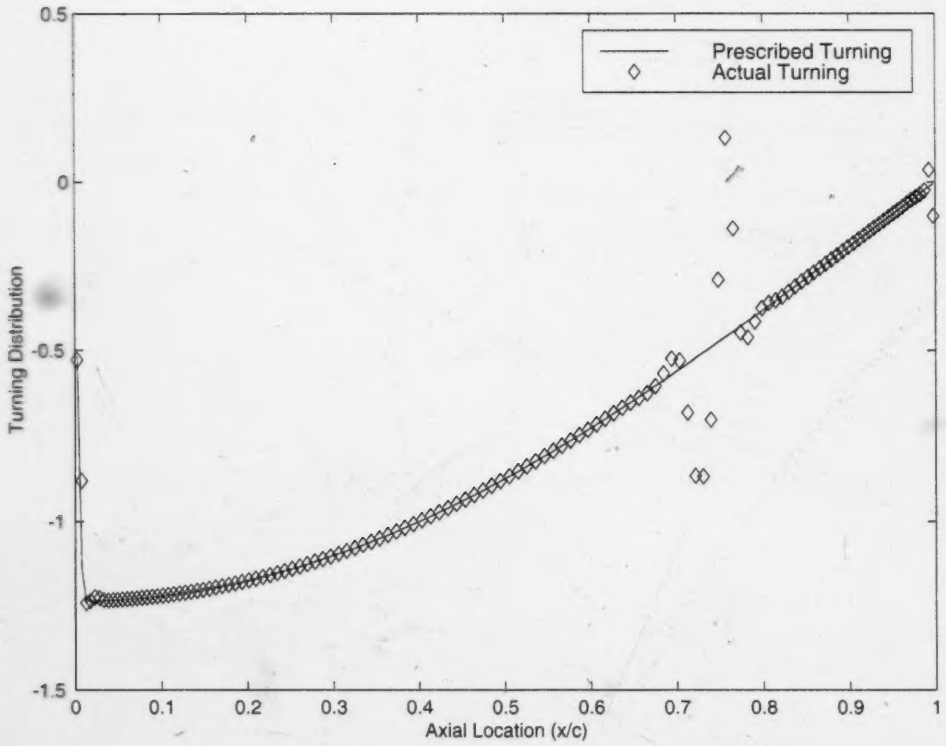

Figure 4.48: Transonic Case 1: Turning Distributions in Blade Passage

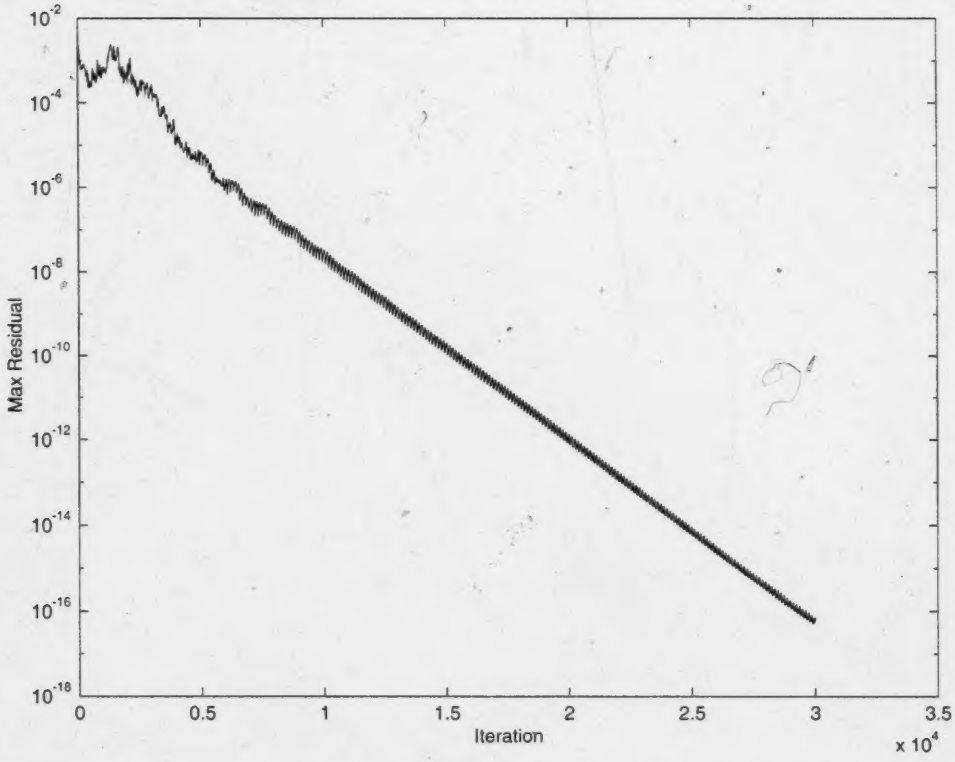

Figure 4.49: Transonic Case 1: Convergence History

4.2.2 Transonic Case 2: New Design - Discontinuous Geometry

Step 1 - Thickness Generation

The previous transonic test case provided further evidence that design of the camberline alone is insufficient to generate a final blade shape which has acceptable aerodynamic characteristics. This test case prescribes the same smooth turning distribution as the previous transonic test case, starting with the discontinuous camberline generated from Sec. (4.2.1). All other input parameters are kept the same. The camberline and thickness from the geometry of the first test are used to allow the new design procedure to redesign the discontinuous geometry.

The thickness is now allowed to change and counters the shock present in the passage by allowing flow through blade downstream of the axial shock location. This is clearly shown in plots of angle of the blade and flow, Figs. (4.50) and (4.51), where flow through the blade is allowed in an attempt to satisfy the turning distribution. The expansion downstream of the shock turned the flow discontinuously and the thickness generator now must deal with this effect. While the thickness generator is allowing flow across the blade surfaces it adjusts the thickness to counter the discontinuous change in flow direction due to the shock. It accomplishes this by reducing the thickness shown in Fig. (4.52), thus eliminating the shock. Fig. (4.53) shows Mach number contours of the converged flow field, where the shock has been eliminated by the new thickness.

Due to the fact the passage shock was eliminated, the surface pressure distributions, Figs. (4.54) and (4.55), are smooth and no longer contain

the large discontinuities that were caused by the shock. Also, because the thickness has allowed flow through the blades surfaces, the actual turning distribution, shown in Fig. (4.56), almost matches the prescribed turning distribution completely. The flow through the blades will be remedied by modifying the camberline (Step 2 of the procedure) and because the new thickness has eliminated the shock, the final camberline and turning should be smooth.

The design of thickness has again illustrated that it's consideration can not be ignored. Without including thickness into the design procedure there is no way for a designer to chose a thickness which will not cause a passage shock.

Text continues on page 152

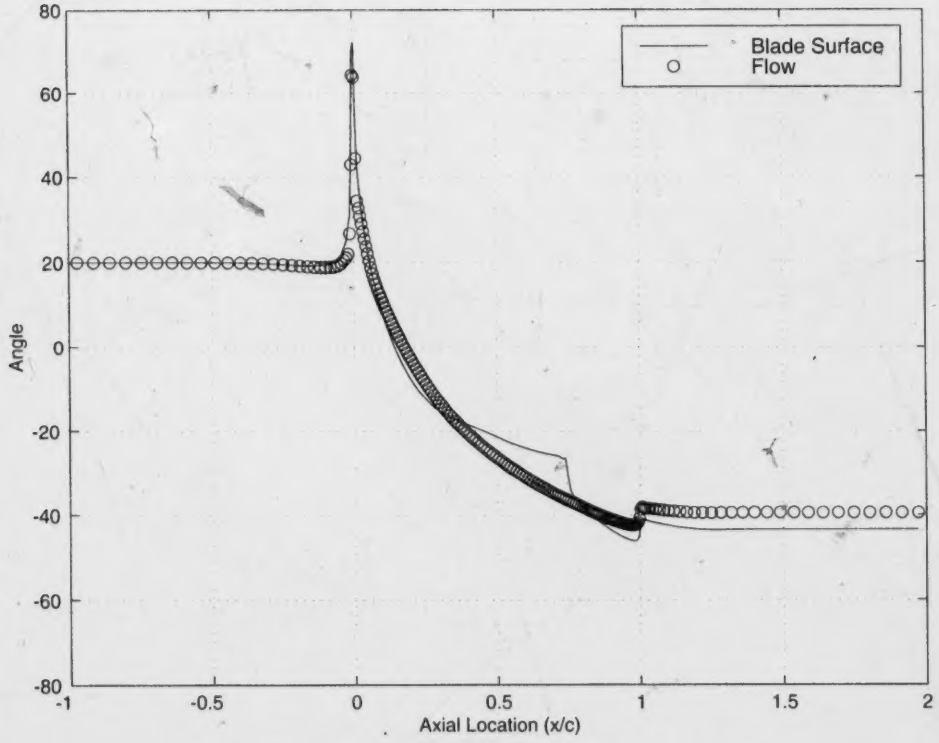

Figure 4.50: Transonic Case 2: Step 1 - Blade and Velocity Angles - Suction Side

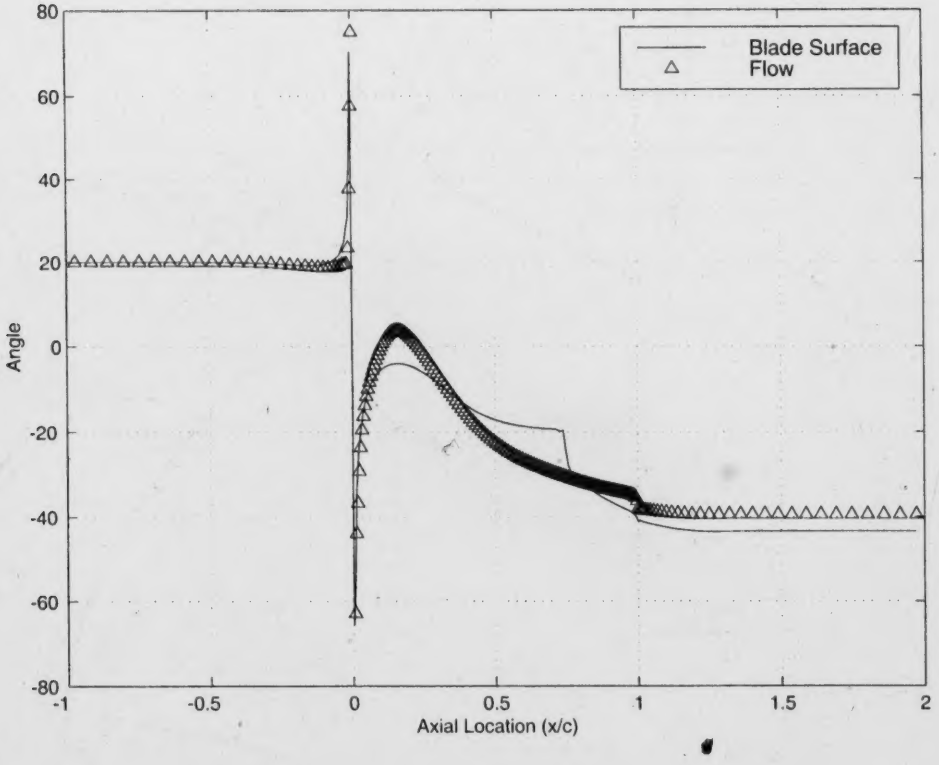

Figure 4.51: Transonic Case 2: Step 1 - Blade and Velocity Angles - Pressure Side

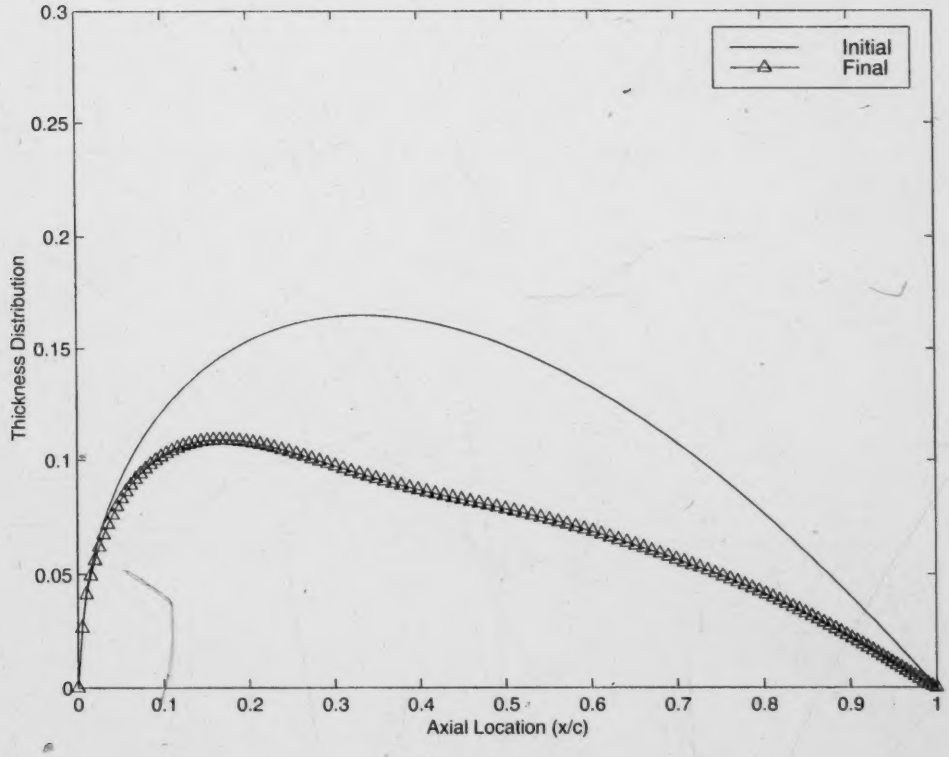

Figure 4.52: Transonic Case 2: Step 1 - Prescribed and Calculated Thickness Distributions

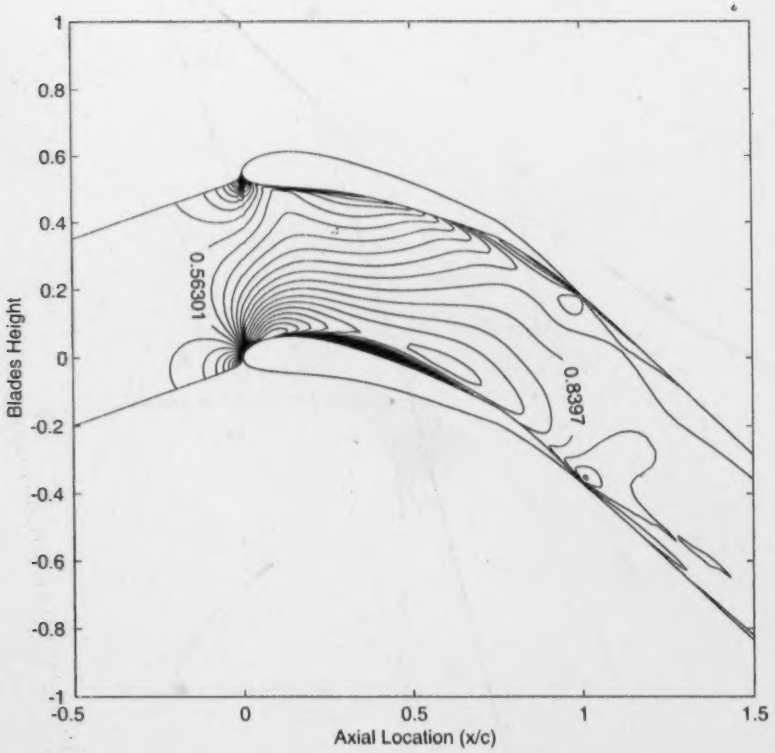

Figure 4.53: Transonic Case 2: Step 1 - Contours of Mach Number in the Blade Passage

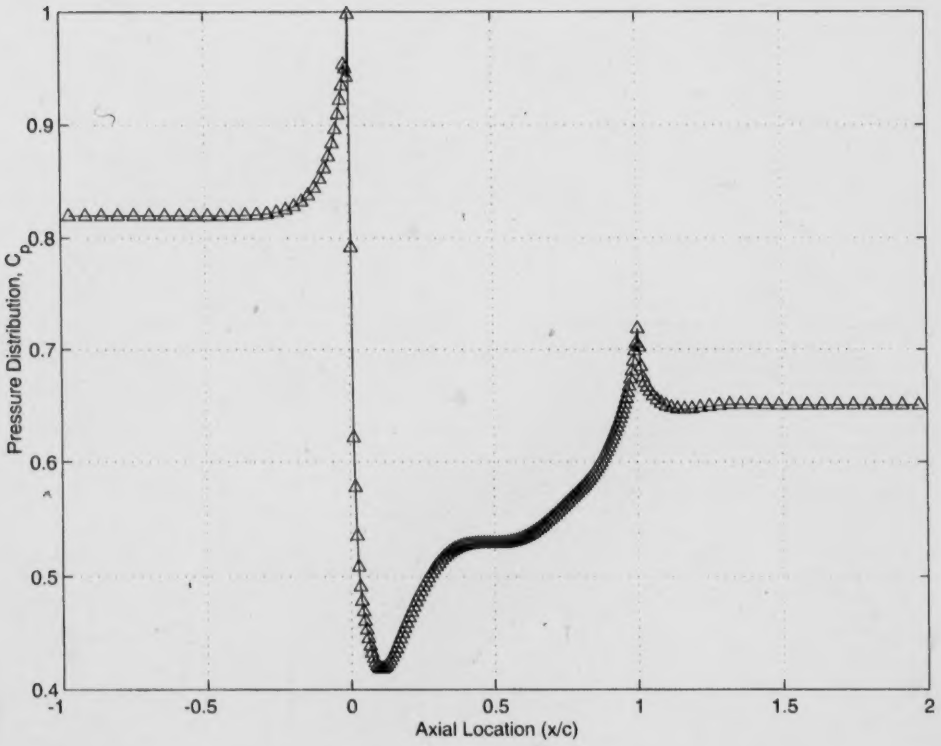

Figure 4.54: Transonic Case 2: Step 1 - Pressure Distribution on Blade Surface - Suction Side

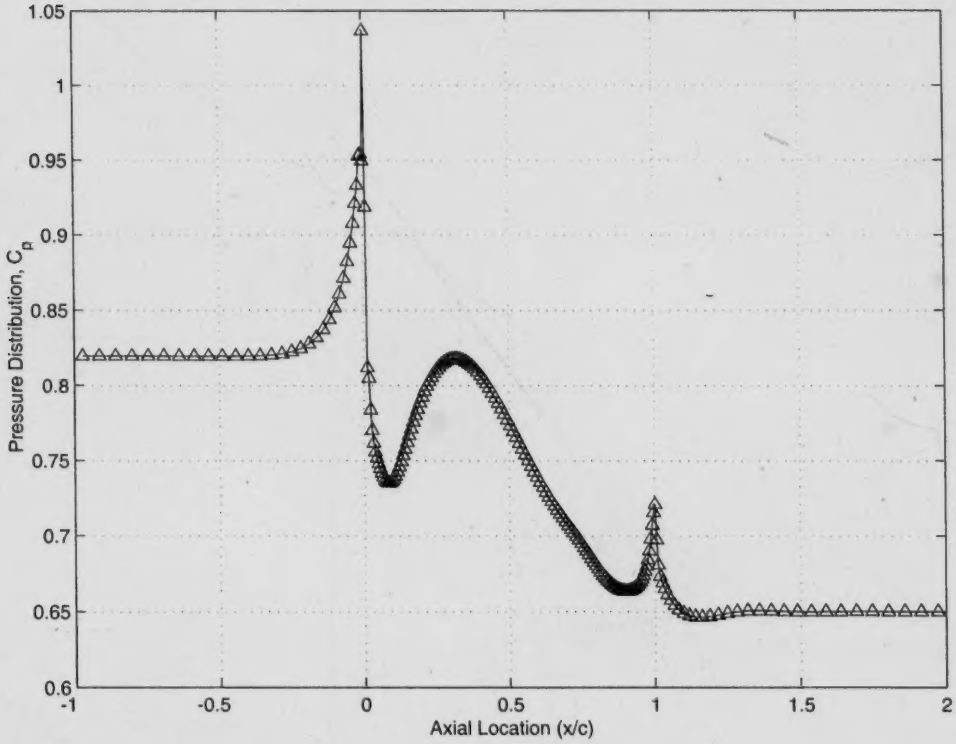

Figure 4.55: Transonic Case 2: Step 1 - Pressure Distribution on Blade Surface - Pressure Side

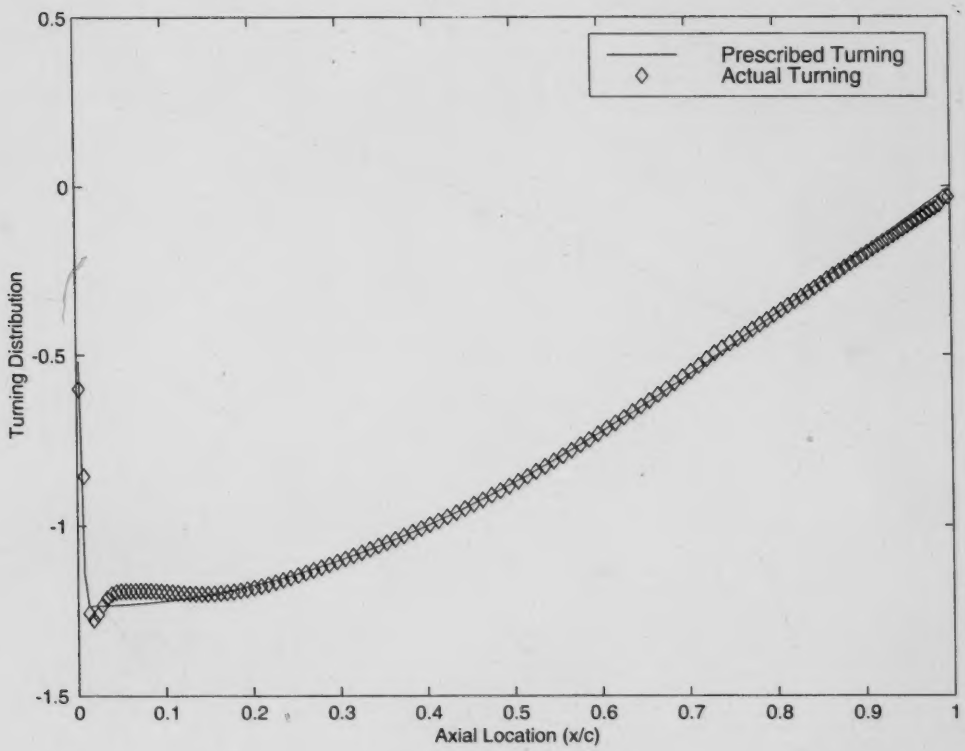

Figure 4.56: Transonic Case 2: Step 1 - Turning Distributions in Blade Passage

Step 2 - Camberline Generation

To alleviate the remaining problems, the thickness distribution is held constant and the camberline is modified. The new thickness has eliminated the shock in the passage. The camberline generator now does not have to deal with the shock and designs a continuous camberline. The continuous camberline is the mid-line of the converged blade, shown in Fig. (4.57). Due to the continuous camberline and smooth thickness the blade surfaces are now continuous as shown in Fig. (4.57). To further show the improvement of the continuous blade geometry, the converged flow field is shown in Fig. (4.58), where it is evident that the passage shock is no longer present.

The continuous blade surfaces now have continuous pressure distributions along them, shown in Figs. (4.59) and (4.60). With the elimination of the jump in surface pressures the chances of separation occurring in a real flow, compared to the previous transonic test case, have drastically been reduced. The actual and prescribed turning, shown in Fig. (4.61), now match perfectly due to the continuous blade surfaces. Another benefit of the fully designed cascade is the mass flow through the passage has increased from $\dot{m} = 0.253\sqrt{\gamma R\Theta_o}$ to $\dot{m} = 0.277\sqrt{\gamma R\Theta_o}$.

Unlike the subsonic case, another pass of the design procedure is not needed. The discontinuity in the blade surfaces have been removed, global and local turning requirements are met and the large discontinuities in pressure distributions have been removed. The final requirement is that the no-flux condition be satisfied on the blade surfaces. This is enforced by the camberline generator and is shown in Figs. (4.62) and (4.63). The maximum residual was again converged to machine zero as shown in Fig. (4.64).

The jump in the residual at 60,000 iterations corresponds to the switch from thickness generation to camberline generations.

The purpose of these transonic test cases was to provide another piece of conclusive evidence that both camberline and thickness must considered when designing a blade geometry. The evidence was shown with the elimination of a passage shock. Not only would a shock create a large energy loss in the passage but more importantly it caused a discontinuity in the geometry, when only camberline was considered. The new design procedure was able to deal with the passage shock by eliminating it and also by correcting the discontinuity in the blade surfaces. Along with the continuous blade surfaces, an added benefit was also shown in the surface pressure distributions. The large pressure jump across a shock would most assuredly cause separation in a real flow but the new technique adjusted for the shock and alleviated this large jump in surface pressures.

Text continues on page 162

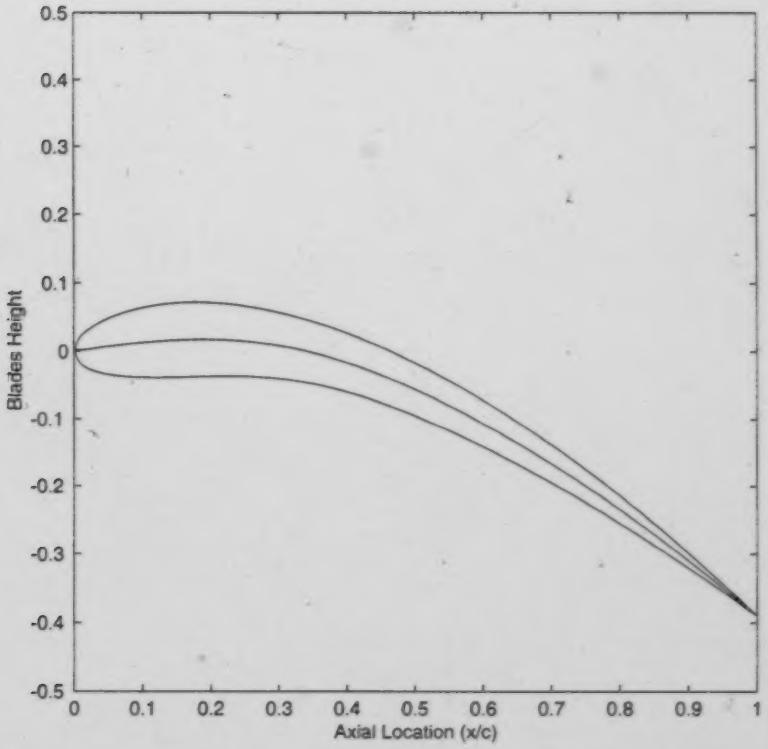

Figure 4.57: Transonic Case 2: Converged Blade Shape

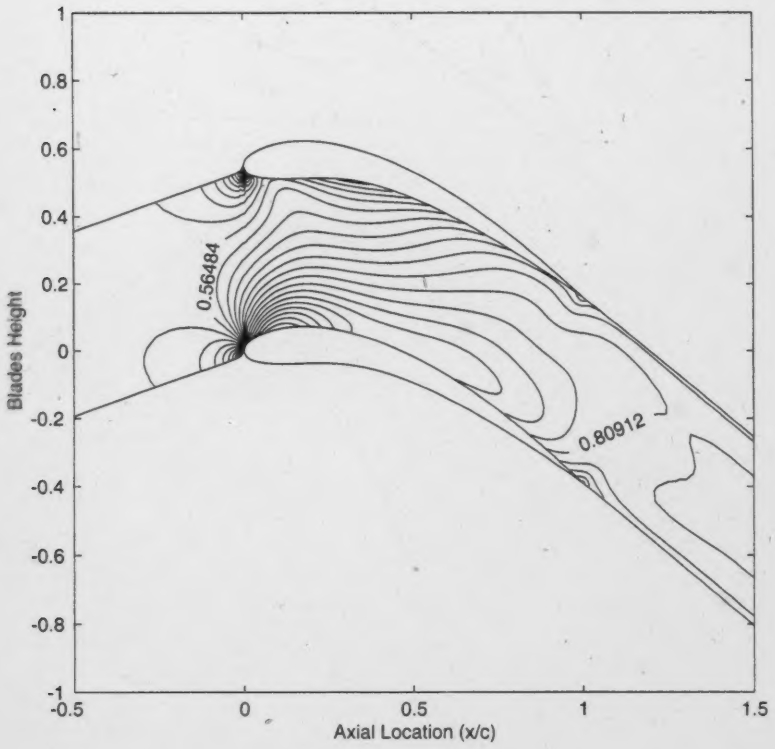

Figure 4.58: Transonic Case 2: Contours of Mach Number in the Blade Passage

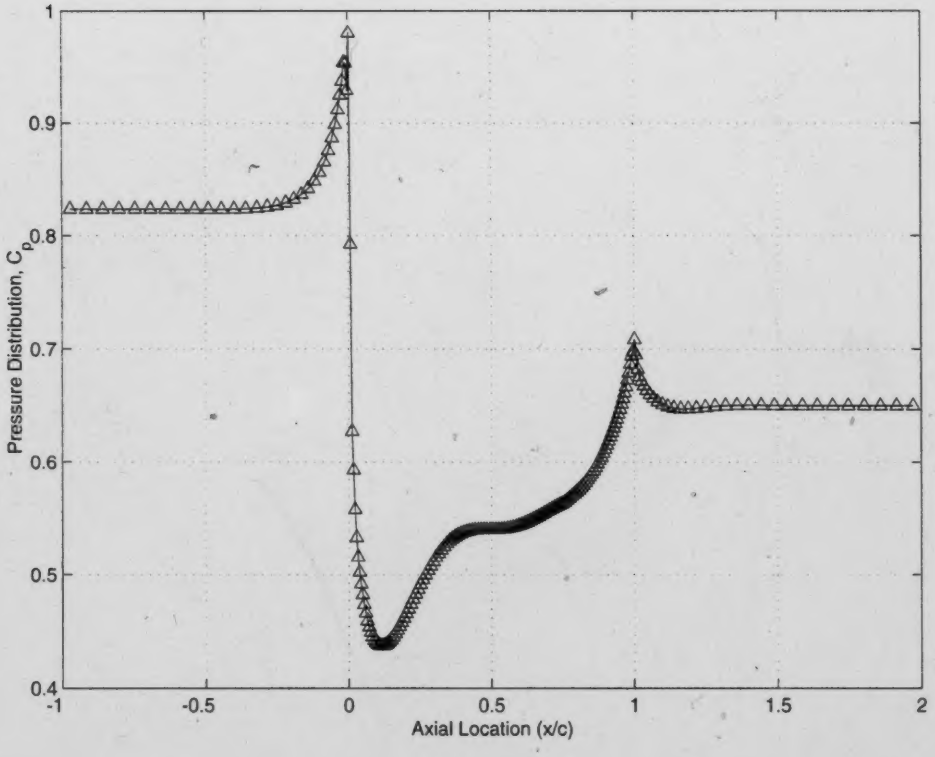

Figure 4.59: Transonic Case 2: Pressure Distribution on Blade Surface - Suction Side

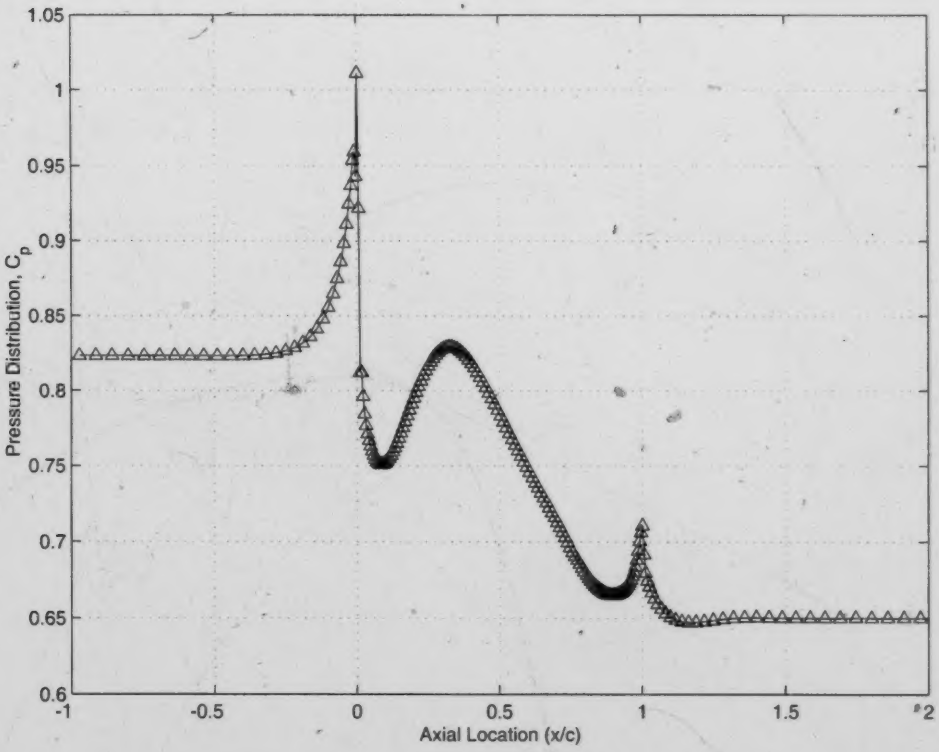

Figure 4.60: Transonic Case 2: Pressure Distribution on Blade Surface - Pressure Side

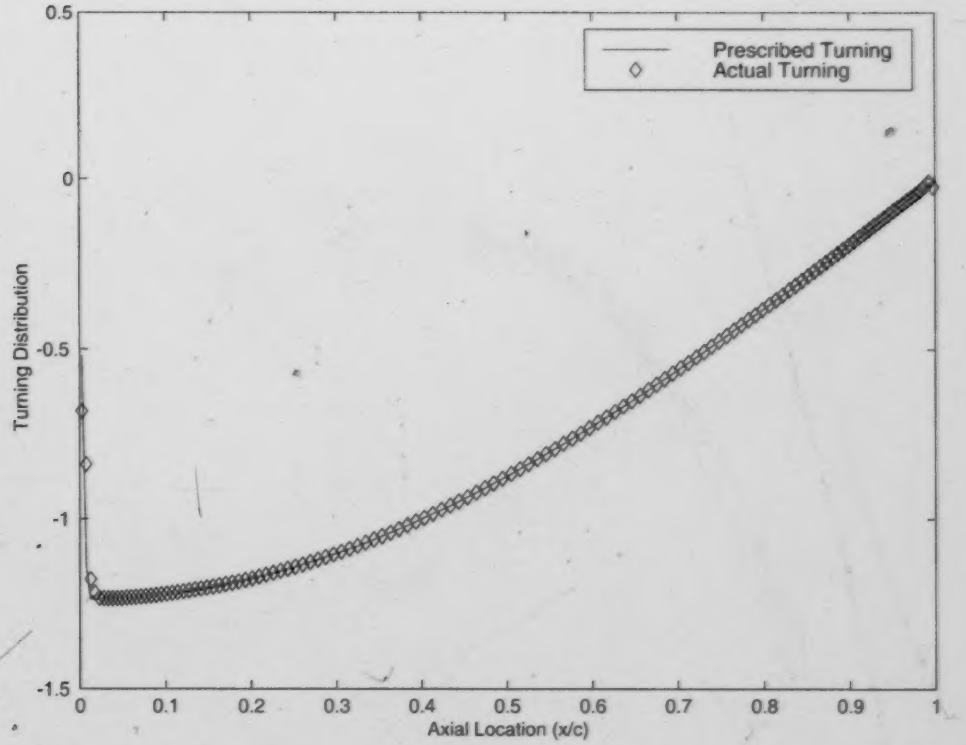

Figure 4.61: Transonic Case 2: Turning Distributions in Blade Passage

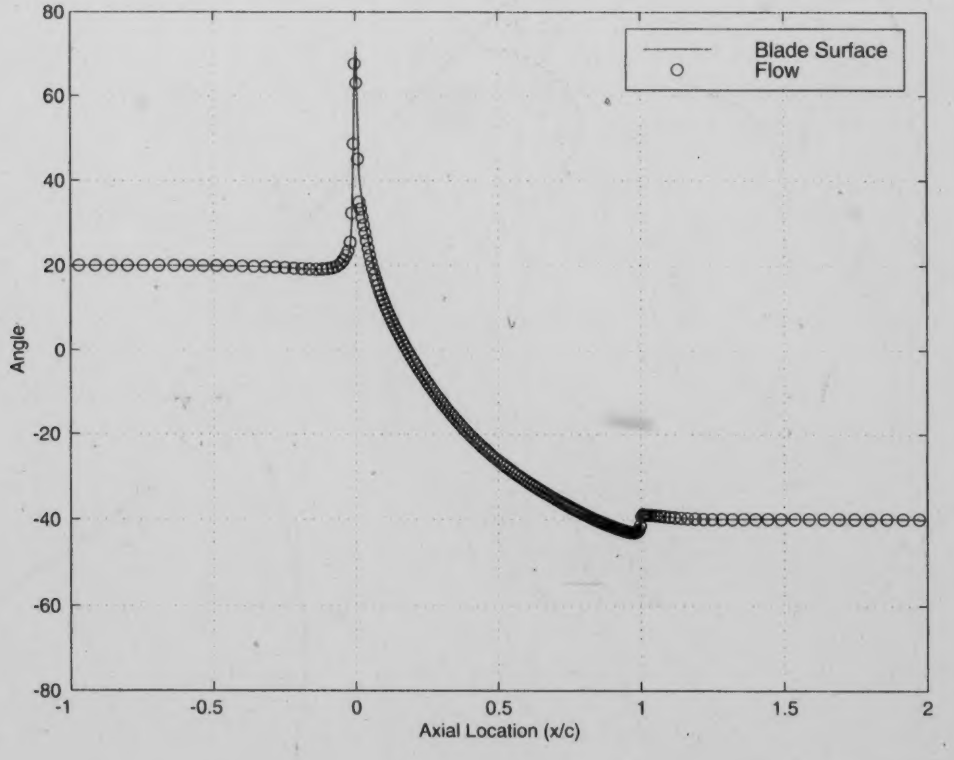

Figure 4.62: Transonic Case 2: Blade and Velocity Angles - Suction Side

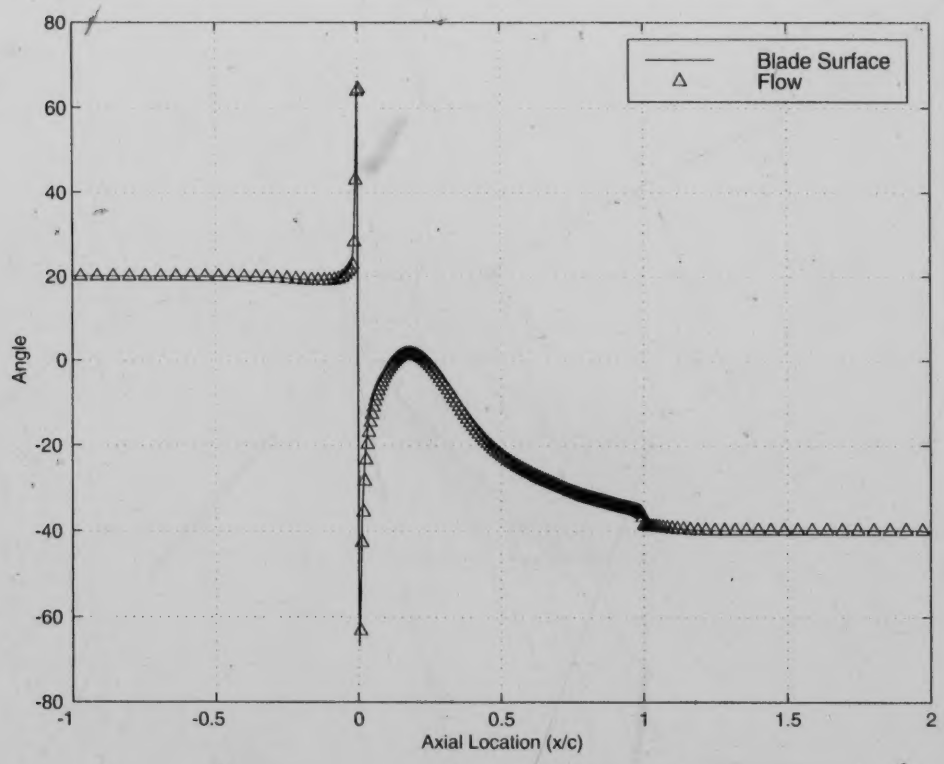

Figure 4.63: Transonic Case 2: Blade and Velocity Angles - Pressure Side

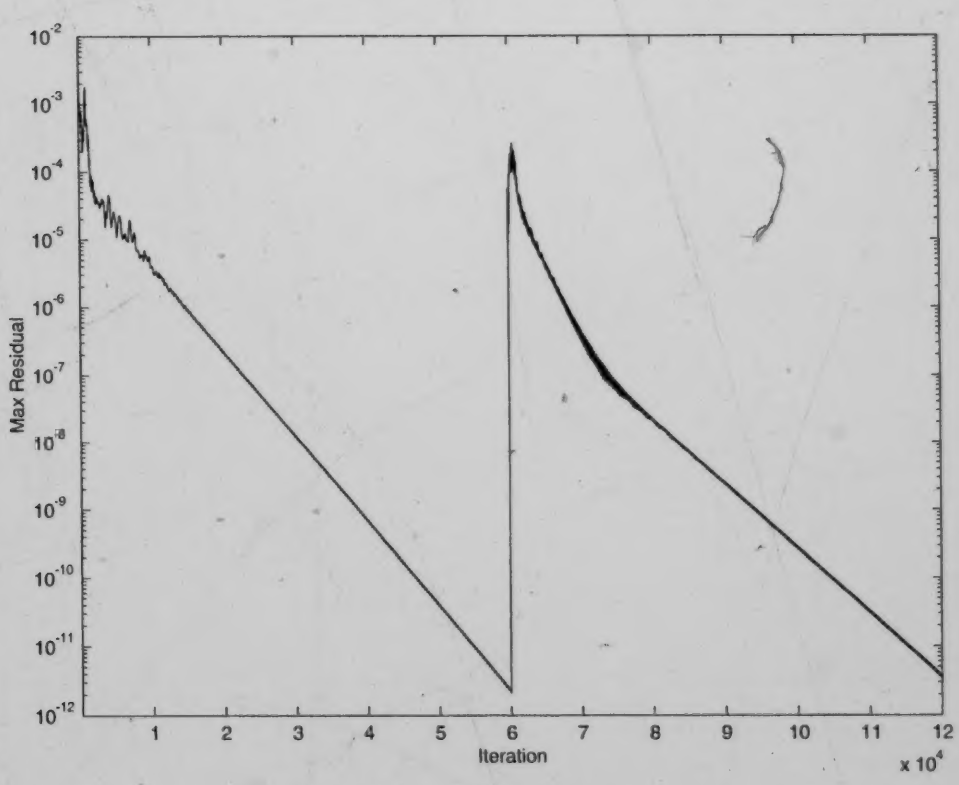

Figure 4.64: Transonic Case 2: Convergence History

Chapter 5

Conclusions

Within this work, a numerical technique for designing the thickness of a turbomachinery blade in an inviscid, compressible flow has been developed. First, an equation to relate the thickness to the surfaces velocities was derived. Then, this equation was transformed into a second order partial differential equation to allow control of the leading and trailing edges. This was needed to avoid creating blade geometries with open trailing edges or "fish tails".

To avoid problems at the leading edge, the thickness distribution was decomposed into fixed and corrected quantities. Along with this decomposition, a function was introduced to limit changes near the leading edge.

After evaluating various numerical constructions of the thickness correction equation, the approximation used was chosen to prevent erroneous mass flow through the blades.

The new design procedure consisted of constructing the entire blade using the newly developed thickness generator with the two dimensional flow field integrator and camberline generator from the work of Medd [Medd 1998] and

Yokota and Medd [Yokota & Medd 2002]. By describing the blade surfaces as a camberline and thickness distribution, the final blade shape was obtained by coupling the camberline and thickness to the material line of the flow which convects from inflow to outflow. The generated blade geometry was modified through a blade surface pressure boundary condition, which was obtained by coupling it with the mass flux averaged tangential velocity distribution.

The first inverse design calculation was the design of the camberline in a subsonic flow using Medd's method [Medd 1998]. This method proved that given a prescribed turning distribution and thickness the camberline could be calculated satisfying both the turning requirements and the no-flux condition on the blade surfaces. This calculation generated an acceptable geometry based on the smooth, prescribed thickness distribution and calculated camberline.

The second inverse design case in the subsonic flow regime used the same input parameters as the first but replaced the smooth, prescribed thickness with a thickness containing oscillations. The point of introducing the thickness oscillations was to prove that without consideration of both camberline and thickness there is no guarantee the final blade shape will provide acceptable aerodynamic characteristics. The oscillations in the thickness caused large oscillations in the pressures along the blade surfaces. Because the turning distribution was smooth, there was competing influences. The camberline generator tried to fix the problem by creating some oscillations in the camberline but because of the way the thickness is added to the camberline it could not eliminate oscillations in the blade surfaces. Even though the designed camberline met the global turning requirement it could not eliminate

local oscillations in the final turning distribution. As a consequence of the oscillations in the blade surfaces there were large oscillations in the pressure distributions, which, if large enough, could lead to separation in a real flow.

The final design case in the subsonic flow regime involved the design of thickness using the new design procedure based on a prescribed turning and camberline. The same smooth turning distribution was used along with the camberline that was calculated from previous test case. The smooth turning distribution again should produce smooth pressure distributions along the blade surface; however, due to the oscillations present in the prescribed camberline this created oscillations in the pressures. Because the thickness generator was constructed to allow flow through the blade surfaces, the thickness generator smoothed out the oscillations in the thickness to counter the pressure oscillations. The converged thickness was now smoother but the camberline still had oscillations. The thickness was then held fixed and the camberline was modified to remove the flow through the blades surfaces, satisfying the no-flux condition. After one pass of this procedure the turning distribution was not perfect, therefore one more pass was needed to generate a blade which matched the turning distribution perfectly and minimized the oscillations on the blade pressure distributions.

To further solidify the inclusion of thickness into the design procedure, it was used to redesign a previously ill-designed transonic blade. The first transonic case reiterated the results from Medd's method [Medd 1998] where a transonic blade design was discontinuous due to a passage shock. A smooth turning distribution and a smooth thickness were prescribed. The smooth turning distribution should produce smooth blade surfaces but due to the

passage shock this was not possible. The shock turned the flow discontinuously and forced the geometry to counter this by becoming discontinuous. This proved the camberline generator was not able to match turning distribution while maintaining the no-flux condition on the blade surfaces. In an inviscid flow the blade generated may satisfy the global turning requirements but due to the passage shock and the large oscillations present in the pressure distributions, the real flow would most assuredly separate.

The final transonic case now included the design of the thickness to deal with the effects of the camberline discontinuity and the passage shock. The same smooth turning distribution was prescribed along with the discontinuous camberline generated from the previous transonic case. To follow the prescribed turning distribution while dealing with the effects of the passage shock the thickness generator allowed flow the through the blade surfaces downstream of the shock. While the thickness generator allowed flow through the blade surfaces, it adjusted the thickness to counter the oscillations in the pressures. It did this by reducing the thickness which eliminated the shock. Once the thickness had converged and the shock was eliminated there was mass flow through the blade surfaces and the camberline was still discontinuous. The thickness was then held constant and the camberline was then designed to remove the flow across the blade surfaces and match the turning distributions. As all the performance criteria were satisfied after the first iteration, another pass was not needed.

The design procedure used in both the subsonic and transonic cases provides conclusive evidence that when design of the camberline alone is considered there is no guarantee that the generated blade will produce acceptable

aerodynamic characteristics, in both a global and local sense. A fully inverse, two dimensional numerical design technique was derived which considered both the camberline and thickness. It was shown that by also considering the design of the thickness, a useful tool was created that enables the designer to control the global performance of the blade, as well as the local effects. This is important when considering the use of the designed blade in a real flow.

BIBLIOGRAPHY

[Abbott 1959] Abbott I.H. & Deonhoff A.E. "Theory of Wing Sections" *New York, USA Dover Publications* 1959

[Dang 1992] Dang T.Q. "Design of Turbomachinery Blading in Transonic Flows by the Circulation Method" *Journal of Turbomachinery* Vol. 114 pp. 141-146 Jan. 1992

[Dang 1995] Dang T.Q. "Inverse Method for Turbomachine Blades Using Shock Capturing Techniques" *AIAA Paper no. 95-2465* 1995

[Dang & Isgro 1995] Dang T.Q. & Isgro V. "Euler-Based Inverse Method for Turbomachine Blades: Two-Dimensional Cascades" *AIAA Journal* Vol. 33 No. 12 pp. 2309-2315 1995

[Eppler 1990] Eppler R. *Airfoil Design and Data* Springer-Verlag, Berlin, Germany 1990

[Eyi and Lee 1995] Eyi S. & Lee D. "High-Lift Design Optimization Using Navier-Stokes Equations" *AIAA Paper* No. 95-0477 1995

[Giles & Drela 1987] Giles M.B. & Drela M. "Two-Dimensional Transonic Aerodynamic Design Method" *AIAA Journal* Vol. 25, pp. 1199-1205 1987

[Hawthorne 1984] Hawthorne W.R., Wang C., Tan C.S. & McCune J.E. "Theory of Blade Design for Large Deflections: Part 1 - Two-Dimensional Cascade" *ASME Journal of Engineering for Gas Turbines and Power* Vol. 106, pp. 346-353 1984

[Hicks 1987] Hicks R.M. "Transonic Wing Design Using Potential Flow Codes - Successes and Failures" *SAE Paper* 810565 1987

[Jameson et.al. 1979] Jameson A., Schmidt W. & Turkel E. "Numerical Solution of the Euler Equations by Finite Volume Methods Using Runge-Kutta Time Stepping Methods" *ASME Journal of Turbomachinery* Vol. 119 pp. 539-543 1979

[Jameson and Caughey 1977] Jameson A. & Caughey D. "A Finite Volume Method For Transonic Potential Flow Calculations" *AIAA Paper* No. 77-635 1977

[Jameson 1983] Jameson A. "Solution of the Euler Equations for Two Dimensional Transonic Flow by a Multigrid Method" *Applied Mathematics and Computation* Vol. 13 pp. 327-355 1983

[Jiang & Dang 1997] Jiang J. & Dang, T "Design Method for Turbomachinery Blades with Finite Thickness by the Circulation Method" *ASME Journal of Turbomachinery* Vol. 119 pp. 539-543 1997

[Laksh. 1996] Lakshminarayana B. *Fluid Dynamics and Heat Transfer of Turbomachinery* New York, USA John Wiley & Sons. 1996

[Leonard & Van den Braembussche 1992] Leonard O. & Van den Braembussche R.A. "Design Method for the Subsonic and Transonic Cascade with Prescribed Mach Number Distribution" *ASME Journal of Turbomachinery* Vol. 114 pp. 553-560 1992

[Meauze 1982] Meauze G. "An Inverse Time Marching Method for the Definition of Cascade Geometry" *Journal of Turbomachinery* Vol. 11 pp. 650-656 1982

[Medd 1998] Medd A.J. "Inverse Design of Turbomachinery Blades" *M.Sc. Thesis* University of Alberta, Edmonton, Alberta, Canada 1998

[Patankar 1986] Patankar S.V. *Numerical Heat Transfer and Fluid Flow* Hemisphere Publishing Corp. 1986

[Portas 2000] Portas L.O. "Inverse Design of Airfoil Thickness Distributions in Incompressible Flow" *M.Sc. Thesis* University of Alberta, Edmonton, Alberta, Canada 2000

[Sanz 1998] Sanz J.M. "Automated Design of Controlled-Diffusion Blades" *ASME Journal of Turbomachinery* Vol. 110 pp. 540-544 1988

[Selig & Maughmer 1992] Selig M.S. & Maughmer M.D. "Multipoint Inverse Airfoil Design Method Based on Conformal Mapping" *AIAA Journal* Vol. 30 No. 5 pp. 1162-1170 May 1992

[Serrin 1959] Serrin S. "Mathematic Principles of Classical Fluid Dynamics" *Encyclopedia of Physics* ed. Flugge S., Vol. 13, Springer, Berlin 1959

[Tan et.al. 1984] Tan C.S., Hawthorne W.R., McCune J.E. & Wang C. "Theory of Blade Design for Large Deflections: Part 2 - Annular Cascades" *ASME Journal of Engineering for Gas Turbines and Power* Vol. 106 No. 5 pp. 354-365 1984

[von Mises 1959] von Mises R. *Theory of Flight* New York, USA Dover Publications 1959

[Whitham 1974] Whitham G.B. *Linear and Nonlinear Waves* New York, New York, USA Wiley and Sons 1974

[Yokota & Medd 2002] Yokota J.W. & Medd A.J. "Shock Fitting a Transonic Cascade Solution into an Inverse Design Technique" *Journal of Propulsion and Power* Vol. 18 No. 1 Jan.-Feb. 2002

Appendix A

Derivation of Euler Equations from First Principles

Following the analysis of Serrin [Serrin 1959], the Transport Theorem for some quantity f can be written as

$$\frac{D}{Dt}\iiint_{\forall} f d\forall = \iiint_{\forall}\left[\frac{Df}{Dt} + f\nabla\cdot\vec{V}\right] d\forall \tag{A.1}$$

where $\forall$ is a volume of fluid moving with the flow and $d\forall$ is its infinitesimal counterpart.

$$\frac{D}{Dt} = \frac{\partial}{\partial t} + \vec{V}\cdot\nabla \tag{A.2}$$

is the derivative following fluid particles in the material frame, written in tensor notation as

$$\frac{D}{Dt} = \frac{\partial}{\partial t} + v_j\frac{\partial_i}{\partial x_j} \tag{A.3}$$

A.1 Conservation of Mass

Assuming no mass sources or sinks

$$\frac{D}{Dt}\iiint_{\forall} \rho \, d\forall = 0 \tag{A.4}$$

The Transport Theorem (A.1) can be used to write Eqn. (A.4) in the form

$$\iiint_{\forall} \left[\frac{D\rho}{Dt} + \rho\nabla\cdot\vec{V}\right] d\forall = 0 \tag{A.5}$$

and expanding the material derivative term

$$\iiint_{\forall} \left[\frac{\partial\rho}{\partial t} + \vec{V}\cdot\nabla\rho + \rho\nabla\cdot\vec{V}\right] d\forall = 0 \tag{A.6}$$

The two dot products can be combined

$$\iiint_{\forall} \left[\frac{\partial\rho}{\partial t} + \nabla\cdot\left(\rho\vec{V}\right)\right] d\forall = 0 \tag{A.7}$$

Since $d\forall$ is an arbitrary infinitesimal volume, conservation of mass can now be written in partial differential conservative form using index notation

$$\frac{\partial\rho}{\partial t} + \nabla\cdot\left(\rho\vec{V}\right) = 0 \tag{A.8}$$

A.2 Conservation of Linear Momentum

$$\frac{D}{Dt}\iiint_{\forall} \vec{V}\rho \, d\forall = \iiint_{\forall} \overline{\overline{f}}\rho \, d\forall + \iint_{S} \vec{t} \, dS \tag{A.9}$$

where $\overline{\overline{f}}$ is the external body forces acting on $\forall$ and t is the surface traction forces acting on S

By virtue of Eqn. (A.8) and the Transport Theorem (A.1), the left hand integrand of Eqn. (A.9) is written as

$$\iiint_{\forall} \rho\frac{D\vec{V}}{Dt} \, d\forall = \iiint_{\forall} \overline{\overline{f}}\rho \, d\forall + \iint_{S} \vec{t} \, dS \tag{A.10}$$

Assuming no external body forces and using the definition of $\vec{t} = -P\vec{n}$ for a perfect fluid

$$\iiint_{\forall} \rho\frac{D\vec{V}}{Dt} \, d\forall = -\iint_{S} P\vec{n} \, dS \tag{A.11}$$

and applying the divergence theorem to the right hand integrand

$$\iiint_{\forall} \rho\frac{\partial\vec{V}}{\partial t} = -\iiint_{\forall} \nabla P \, d\forall \tag{A.12}$$

since $d\forall$ is an arbitrary infinitesimal volume, Eqn. (A.12) can be written in partial differential vector and tensor form

$$\rho\frac{D\vec{V}}{Dt} = -\nabla P \quad ; \quad \rho\frac{Dv_i}{Dt} = -\frac{\partial P}{\partial x_i} \tag{A.13}$$

Eqn. (A.13) can be obtained in conservative form as follows. Writing the vector form of the x component of the left hand side of Eqn. (A.13) in terms of the definition of the material derivative

$$\rho\frac{Du}{Dt} = \rho\frac{\partial u}{\partial t} + \rho\vec{V}\cdot\nabla u \tag{A.14}$$

Also, expanding the following derivative

$$\rho\frac{\partial(\rho u)}{\partial t} = \rho\frac{\partial u}{\partial t} + u\frac{\partial \rho}{\partial t}$$

and rearranging

$$\rho\frac{\partial u}{\partial t} = \rho\frac{\partial(\rho u)}{\partial t} - u\frac{\partial \rho}{\partial t} \tag{A.15}$$

Using the vector identity for the divergence of the product of scalar times a vector

$$\nabla\cdot(\rho u\vec{V}) = u\nabla\cdot(\rho\vec{V}) + (\rho\vec{V})\cdot\nabla u$$

and rearranging

$$(\rho\vec{V})\cdot\nabla u = \nabla\cdot(\rho u\vec{V}) - u\nabla\cdot(\rho\vec{V}) \tag{A.16}$$

Substituting Eqn. (A.15) and (A.16) into Eqn. (A.15) yields

$$\begin{aligned}\rho\frac{Du}{Dt} &= \frac{\partial(\rho u)}{\partial t} - u\frac{\partial \rho}{\partial t} - u\nabla\cdot(\rho\vec{V}) + \nabla\cdot(\rho u\vec{V}) \\ &= \frac{\partial(\rho u)}{\partial t} - u\left[\frac{\partial \rho}{\partial t} - \nabla\cdot(\rho\vec{V})\right] + \nabla\cdot(\rho u\vec{V})\end{aligned} \tag{A.17}$$

The term in the brackets on the left hand side is simply continuity, hence it is zero. Therefore Eqn. (A.17) is reduced to

$$\rho\frac{Du}{Dt} = \frac{\partial(\rho u)}{\partial t} + \nabla\cdot(\rho u\vec{V}) \tag{A.18}$$

Substituting Eqn. (A.18) back into the x component of Eqn. (A.13)

$$\frac{\partial(\rho u)}{\partial t} + \nabla\cdot(\rho u\vec{V}) = -\frac{\partial P}{\partial x} \tag{A.19}$$

and similarly for the y component

$$\frac{\partial(\rho v)}{\partial t} + \nabla\cdot(\rho v\vec{V}) = -\frac{\partial P}{\partial y} \tag{A.20}$$

Writing the equations for conservation of linear momentum in partial differential conservative form using tensor notation

$$\frac{\partial(\rho v_i)}{\partial t} + \frac{\partial(\rho u_i u_j)}{\partial x_j} = -\frac{\partial P}{\partial x_i} \tag{A.21}$$

A.3 Conservation of Energy

$$\frac{D}{Dt}\iiint_{\forall}\rho e_t\, d\forall = -\iint_{S}(\vec{q}\cdot\vec{n})\, dS + \iint_{S}(\vec{t}\cdot\vec{v})\, dS + \iiint_{\forall}\rho(\overline{\overline{f}}\cdot\vec{v})\, d\forall \tag{A.22}$$

where e_t is the total energy defined as $e_t = \Upsilon + \frac{\vec{V}\cdot\vec{V}}{2}$, with Υ as the internal, $\vec{q}$ is the heat flux through the surface S, $\vec{t}$ are the surface traction vectors acting on the surface S and $\overline{\overline{f}}$ are the body forces acting on the volume $\forall$.

By virtue of Eqn. (A.8) and the Transport Theorem (A.1), the right hand integrand of Eqn. (A.22) is written as

$$\iiint_{\forall} \rho \frac{De_t}{Dt}\, d\forall = -\iint_{S} (\vec{q}\cdot\vec{n})\, dS + \iint_{S} (\vec{t}\cdot\vec{v})\, dS + \iiint_{\forall} \rho(\overline{\overline{f}}\cdot\vec{v})\, d\forall \qquad \text{(A.23)}$$

Assuming no external body forces or heat flux and using the definition of $\vec{t} = -P\vec{n}$ for a perfect fluid

$$\iiint_{\forall} \rho \frac{De_t}{Dt}\, d\forall = -\iint_{S} P\vec{V}\cdot\vec{n}\, dS \qquad \text{(A.24)}$$

and converting the surface integral into a volume integral using the divergence theorem

$$\iiint_{\forall} \rho \frac{De_t}{Dt}\, d\forall = -\iiint_{\forall} \nabla(P\vec{V})\, d\forall \qquad \text{(A.25)}$$

since $d\forall$ is an arbitrary infinitesimal volume, Eqn. (A.25) can be written in partial differential vector and tensor form

$$\rho \frac{De_t}{Dt} = -\nabla(P\vec{V}) \quad ; \quad \rho \frac{De_t}{Dt} = -\frac{\partial(Pv_i)}{\partial x_i} \qquad \text{(A.26)}$$

Following a similar procedure to that of the momentum equation, the left hand side of Eqn. (A.24) can be written as

$$\rho \frac{De_t}{Dt} = \frac{\partial(\rho e_t)}{\partial t} + \nabla\cdot(\rho e_t \vec{V}) \qquad \text{(A.27)}$$

Substituting this into Eqn. (A.26) and writing the conservation of energy in conservative from using tensor notation

$$\frac{\partial(\rho e_t)}{\partial t} + \frac{(\partial \rho e_t v_i)}{\partial x_i} = -\frac{\partial(Pv_i)}{\partial x_i} \qquad \text{(A.28)}$$